Brigham Young University
BYU ScholarsArchive

All Theses and Dissertations

2017-03-01

High-Sensitivity Phased Arrays for Radio Astronomy and Satellite Communications

Junming Diao
Brigham Young University

Follow this and additional works at: https://scholarsarchive.byu.edu/etd

Part of the Electrical and Computer Engineering Commons

BYU ScholarsArchive Citation

Diao, Junming, "High-Sensitivity Phased Arrays for Radio Astronomy and Satellite Communications" (2017). *All Theses and Dissertations*. 6546.
https://scholarsarchive.byu.edu/etd/6546

This Dissertation is brought to you for free and open access by BYU ScholarsArchive. It has been accepted for inclusion in All Theses and Dissertations by an authorized administrator of BYU ScholarsArchive. For more information, please contact scholarsarchive@byu.edu, ellen_amatangelo@byu.edu.

High-Sensitivity Phased Arrays for Radio Astronomy and Satellite Communications

Junming Diao

A dissertation submitted to the faculty of
Brigham Young University
in partial fulfillment of the requirements for the degree of

Doctor of Philosophy

Karl F. Warnick, Chair
Brian D. Jeffs
Neal K. Bangerter
Michael D. Rice
David G. Long

Department of Electrical and Computer Engineering

Brigham Young University

Copyright © 2017 Junming Diao

All Rights Reserved

ABSTRACT

High-Sensitivity Phased Arrays for Radio Astronomy and Satellite Communications

Junming Diao
Department of Electrical and Computer Engineering, BYU
Doctor of Philosophy

Radio astronomy is used to study stars, galaxies, black holes and gas clouds radiation at radio frequencies. Detecting extremely weak signals from deep space radio sources requires high sensitive feed system associated with large dish antennas. The key figure of merit is survey speed, or the time required to map a region of the sky to a given source flux density. Survey speed is proportional to the frequency bandwidth, the field of view or observable region of the sky, and the squared sensitivity, where sensitivity is related to reflector aperture efficiency and system noise temperature. Compared to the traditional single feed, phased array feeds with significantly expanded field of view are considered as the next generation feed for radio telescope. This dissertation outlines the design, analysis and measurement of high sensitivity L-band and mm-wave phased array feeds for the 100-meter Green Bank Telescope.

Theoretical works for radio astronomy includes design guideline for high sensitivity phased array feed, fundamental frequency bandwidth limit, array antenna loss influenced by mutual coupling and beamformer coefficients and possibility of superdirectivity for radio telescopes and other antennas. These study are helpful to understand and guide the design of a phased array feed system.

In the absence of dish antennas, sparse phased arrays with aperiodic structure have been developed for satellite communications. A compromise between the peak side lobe level, array element density, directivity and design complexity is studied. We have found that the array peak side lobe level can be reduced by enhancing the array element direction at the main lobe direction, increasing the array element density and enlarging the array size.

A Poynting streamline approach develops to understand the properties of a receiving antenna and the mutual coupling effects between array elements. This method has been successfully used to generate effective area shape for many types of antennas and guide the design of a superdirective antenna. Motivated by this method, a superdirective antenna is experimental demonstrated.

Keywords: Phased array feeds, radio astronomy, satellite communications, superdirective antenna, Poynting streamline and antenna effective area shape

ACKNOWLEDGMENTS

I would like to thank especially Dr. Karl F. Warnick, for his support, help and encouragement. I appreciate him giving me a chance to study in the world class phased array research group, doing projects on the state-of-the-art radio telescopes and letting me have lots of free time to pursue my own interest on open research questions. He gave me lots of advice on research and help me to correct my English writing. I enjoy talking and exchanging my ideas with him, and lots of work and results in this dissertation came from the meeting discussion on every Monday morning. I would like to thank all my committee members Dr. David Long, Dr. Neal Bangerter, Dr. Michael Rice and, particularly, Dr. Brian Jeffs, for the helpful feedback and discussion on my research. I would like to thank all my friends in CB 480, it is wonderful that we work hard together for the research and homework and smile hard together for the COUP game during the lunch time. Lastly but most importantly, thank my wife Ting Chen for encouraging, helping and supporting my study.

TABLE OF CONTENTS

LIST OF TABLES

LIST OF FIGURES

CHAPTER 1. INTRODUCTION

1.1 Phased Array Feeds for Radio Astronomy Observations

Radio astronomy is used to study the stars, galaxies, black holes and gas clouds at radio frequencies of celestial objects such as radio galaxies, quasars, pulsars, and masers. The observation of weak astronomical signals is limited by the antenna and feed performance, so highly sensitive radio telescopes are needed. Radio astronomy is conducted using large reflector radio telescopes including single-dish antennas and the multiple linked-dish antennas that utilize radio interferometry techniques. Many radio telescopes have been built such as the Green Bank Telescope (GBT) with a 100-meter dish, the Arecibo Telescope with a 305-meter dish and the Five-hundred-meter Aperture Spherical Telescope (FAST). Besides the aperture size of the reflector antenna, the performance of feed system is another important thing to the radio telescope.

The key figure of merit for a feed system is the receiver output SNR within the time required to observe an area of the sky for a given minimum signal level, or survey speed. Survey speed is proportional to the product of the feed field of view, the squared receiver sensitivity, and the bandwidth. The receiver sensitivity is proportional to the ratio of aperture efficiency and system noise temperature. Compared to a traditional single-pixel horn feed, the primary motivation for phased array feeds is an increase in field of view by electronically forming multiple simultaneous beams. However, the system noise temperature of existing prototype phased array feeds is higher than single-pixel horn feeds. Hence, the major target of current phased array feeds research is to achieve higher sensitivities comparable to state-of-the-art traditional single horn feeds.

Phased array feeds are considered as the next generation feed system for radio telescope by replacing the traditional single horn feed. However, considerations for array antennas include increasing array element bandwidth in an electrically small area, improving active impedance matched between the array antennas and LNAs and making a tradeoff between high sensitivity and wide field of view and minimizing system noise temperature. These requirements make this feed system difficult to achieve a high performance. Thus an accurate phased array feed model is essential to understand and analyze the feed system performance associated with a reflector antenna and design a high sensitivity feed system.

1.2 Low Side Lobe Level Phased Arrays for Satellite Communications

Communication satellites have been used for television, voice, internet applications due to wide coverage range. To track and communicate with a satellite in a geostationary orbit that is about 36,000 kilometers away from the ground, the receivers and transmitters on the ground require high gain, low system noise temperature, and low side lobe levels. For an electronic steered phased array, however, the cost will be significantly increased by a large number of array elements.

To reduce the cost of phased array antennas, many sparsification techniques have been used. Although arrays with large element spacing benefit from reduced mutual coupling and low number of electronic components across the array aperture, grating lobes become a major issue when the element spacing is larger than one half-wavelength.

Aperiodic elements placement techniques offer one possible solution for mitigation grating lobes and reducting of side lobes. Compared to a periodic structure, aperiodicity makes such arrays difficult to design and fabricate. Recently, arrays with periodically rotated random tiles have been developed. The identical tile units and fewer degrees of freedoms help to reduce the design and fabrication complexity for aperiodic arrays.

We improve the design of rotated aperiodic tiles with optimized discrete rotation angles. Compared to the traditional aperiodic array, the design and fabrication complexity can be largely reduced by the tiled array with periodic array structure. The relationship between peak side lobe level, element number and density and the element radiation pattern is studied.

1.3 Receiving Superdirective Antennas Analyzed by Poynting Streamline Method

Antennas are commonly modeled and understood as transmitters, and the reciprocity theorem is used to obtain the receiving properties of the antennas. The goal of this work is to directly analyze antennas as receivers in terms of the influence of antennas on received fields and consider whether this approach can lead to unique insights or new design methods.

A receiving antenna can be considered as a device that concentrates electromagnetic energy at the load. The interaction between the receiving antenna and incident electric field can be analyzed using streamlines of the Poynting vector field, which we refer to as Poynting streamlines. The field energy absorbed by the antenna load is represented by the Poynting streamlines that terminated on the antenna load. By calculating the Poynting streamline distribution near a receiving antenna, the area of the locus of captured streamlines by the antenna load can be considered as the geometrical shape of the antenna effective area. The effective area shape might be considered as a supplementary to the IEEE standard definition of the effective area based on the mathematical result.

High-gain electrically large aperture antennas such as horn antennas commonly use corrugated internal surfaces, metamaterials and dielectric lenses to make the aperture field distribution close to uniform. Limited by the antenna physical aperture size, the antenna aperture efficiency is always less than unity. Instead, the aperture field distribution could be optimized using the Poynting streamline approach to make the antenna effective area larger than the antenna physical aperture size. We have designed a screen consisting of rows of metal rods in front of the horn antenna in such a way that Poynting streamlines are drawn towards the antenna aperture. The enlongated Poynting streamlines area associated with a dipole is used to compensate for a notch shape in the Poynting streamlines area for the horn antenna and thereby achieve a more convex streamline area shape. The drawbacks for a superdirective array antenna includes narrow bandwidth, large antenna loss and sensitivity to the tolerance of element position and excitation. Motivated by Poynting streamline method, practical superdirective antenna that overcome these issues are studied by considering the drawbacks of superdirectivity.

In this dissertation, an L-band dipole array element for the GBT and the corresponding down-converter system are shown in chapter 3. An accurate noise model associated with a reflector antenna is used to analyzed a mm-wave phased array feed for the GBT in Chapter 4. Reflector aperture efficiency for an ultra wide band phased array feed system and array antenna loss are studied in Chapter 5. The peak side lobe levels for aperiodic and tiled arrays are studied in Chapter 6. Poynting streamlines for receiving antennas and superdirective antennas are illustrated in Chapter 7.

1.4 Contribution

Phased array feeds for radio astronomy observations.

- Characterized performance decrease between phased array feeds (beamforming) and cluster feeds (no beamforming), which are most commonly used multiple feed systems for radio astronomy. Simulations and physical intuition were used to explain this effect and clarify its causes and possible remedies. A fundamental bandwidth limit was found for phased array feeds.

- Proposed effective resistance for array antennas similar to the resistance of a single antenna to analyze array antenna loss. It is less well understood that array antenna loss not only depends on the antenna materials, but also relates to the mutual coupling and beamformer weights. Large effective loss resistance occurs when the beam is steered to a large angle under strong mutual coupling.

Poynting streamlines, effective area shapes and superdirectivity.

- Used Poynting streamlines of total fields and antenna effective area shapes to uniquely understand the receiving properties of antennas and mutual couplings and guide the design of a superdirective antenna.

- Showed numerically results that the area of the locus of streamlines terminated by the antenna load is close to the effective area of the antenna, and so we suggest this locus is similar to the effective area shape. The effective area shape might be considered as a supplementary to the IEEE standard definition of the effective area based on the strict mathematical demonstration.

- Suggested electrically small and middle size antennas and electrically large antennas with a large aspect ratio for practical superdirectivity. Predicted physical limit for the directivity of superdirective antennas with arbitrary shape and size.

- Verified a superdirective horn antenna experimentally. To our knowledge, this is the first time to experimentally demonstrate a superdirective antenna with such electrically large aperture.

CHAPTER 2. BACKGROUND

For a receiving antenna system, the primary figure of merit is the sensitivity S, which is related to the system output signal to noise ratio (SNR) by

$$S = \frac{A_\mathrm{e}}{T_\mathrm{sys}} = \frac{k_\mathrm{b} B}{S^\mathrm{sig}} \mathrm{SNR}, \tag{2.1}$$

where A_e is the effective area of the reflector antenna, T_sys is the system noise temperature, k_b is the Boltzman's constant, B is the system bandwidth and S^sig represents the signal power density for a certain polarization.

The output SNR for a passive receiving antenna can be easily defined by the ratio of antenna output signal power to the noise power using aperture efficiency of reflector antenna, equivalent system noise temperature and other figures of merits. For an active receiving array feed system, the definition of SNR and other figures of merits become complicated for mutual coupling effects between each array element, gain for the back end of system, beamformer weights for each element channel, noise match between the antennas and LNAs and so on.

The goal of this section is to define the figures of merits for an active receiving array feed system, including the aperture efficiency, spillover efficiency, radiation efficiency, equivalent system noise temperature, and sensitivity.

2.1 Array Signal Model

Using the reciprocity theorem, when a plane wave with polarization $\hat{p}$ and electric field intensity E_0 incidents on an array antenna from the direction with a spherical angle of Ω, the open circuit voltage for the mth element is

$$v_\mathrm{oc,m}(\hat{p}, E_0, \Omega) = \frac{4\pi j r e^{jkr}}{\omega \mu I_0} E_0 \hat{p} \cdot \overline{E}_m(\bar{r}). \tag{2.2}$$

The position vector $\bar{r}$ has a polar coordinates (r, Ω). $\overline{E}_m(\bar{r})$ is the embedded open circuit loaded radiated field pattern, which represents the radiated far field when the mth element is excited by an input current I_0 with other element open circuited. For an array feed, $\overline{E}_m(\bar{r})$ usually refers to the secondary radiated fields in the presence of a reflector antenna. k represents the space factor of the EM wave. ω is angular velocity. μ represents permeability.

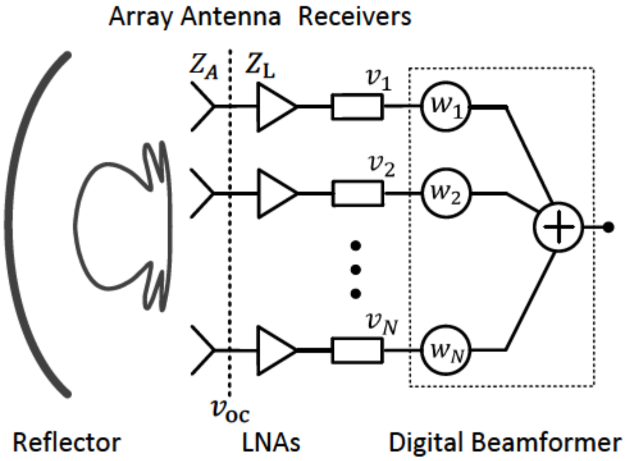

Figure 2.1: Array feed and beamformer system block diagram.

In a PAF system, the signal of interest is received by the array antenna and excites voltages at each antenna port. As shown in Figure 2.1, the received signals at the antenna port are amplified by LNAs and passed into receivers. The signals at the receiver output before the applied beamformer coefficients can be represented by a column vector

$$\mathbf{v} = [v_1, v_2, \ldots, v_N]^{\mathrm{T}}, \tag{2.3}$$

where v_n is the sampled signal from the nth element and N is array element number. $\mathbf{v}_{\mathrm{oc}}$ can be transferred to $\mathbf{v}$ by a transform matrix Q

$$\mathbf{v} = \mathbf{Q}\mathbf{v}_{\mathrm{oc}}, \tag{2.4}$$

where $\mathbf{Q}$ is

$$\mathbf{Q} = g\mathbf{Z_L}(\mathbf{Z_L} + \mathbf{Z_A})^{-1}, \tag{2.5}$$

$\mathbf{Z_A}$ is the array antenna impedance, $\mathbf{Z_L}$ is the load impedance matrix of the receiver chain, and g is the voltage gain of LNA and receiver chain.

In the digital processing, the receiver output signals $\mathbf{v}$ are combined by a vector $\mathbf{w}$ of complex weights to produce a scalar output signal by

$$v = \mathbf{w}^H \mathbf{v}. \tag{2.6}$$

Array excitation current vector is equal to the complex conjugate of vector w. The output signals $\mathbf{v}$ vector is a combination of the signal of interest $\mathbf{v}_{\mathrm{sig}}$ and noise $\mathbf{v}_{\mathrm{n}}$ by

$$\mathbf{v} = \mathbf{v}_{\mathrm{sig}} + \mathbf{v}_{\mathrm{n}}, \tag{2.7}$$

where $\mathbf{v}_{\mathrm{n}}$ can be written as

$$\mathbf{v}_{\mathrm{n}} = \mathbf{v}_{\mathrm{sky}} + \mathbf{v}_{\mathrm{sp}} + \mathbf{v}_{\mathrm{rec}} + \mathbf{v}_{\mathrm{loss}}. \tag{2.8}$$

$\mathbf{v}_{\mathrm{sky}}$ is the sky noise, which represents atmospheric and cosmic background noise received by the feed and reflector system, $\mathbf{v}_{\mathrm{sp}}$ is the spillover noise due to thermal noise from the warm ground received by the antenna feed, $\mathbf{v}_{\mathrm{rec}}$ is the receiver electronics noise and $\mathbf{v}_{\mathrm{loss}}$ is the noise from the antenna ohmic and dielectric losses.

It is convenient to represent these items in terms of correlation matrices. If we assume the background noise environment is statistically stable, the array output voltage correlation matrix is

$$\mathbf{R}_v = \mathrm{E}[\mathbf{v}\mathbf{v}^H] = \lim_{N\to\infty} \frac{1}{N} \sum_{n=1}^{N} \mathbf{v}[n]\mathbf{v}^H[n], \tag{2.9}$$

where $\mathrm{E}[\cdot]$ denotes the time expectation and n represents a sample index.

In most cases, the signal and noise are independent, which means the noise term are uncorrelated, so that

$$\mathrm{E}[\mathbf{v}_{\mathrm{sig}}\mathbf{v}_{\mathrm{n}}^{H}] = \mathbf{0}. \tag{2.10}$$

The correlation matrix $\mathbf{R}$ can then be rewritten as

$$\begin{aligned}\mathbf{R} &= \mathbf{R}_{\mathrm{sig}} + \mathbf{R}_{\mathrm{n}} \\ &= \mathbf{R}_{\mathrm{sig}} + \mathbf{R}_{\mathrm{sky}} + \mathbf{R}_{\mathrm{sp}} + \mathbf{R}_{\mathrm{loss}},\end{aligned} \tag{2.11}$$

where $\mathbf{R}_{\mathrm{n}}$ represents the noise correlation matrix.

For an array output signal $\mathbf{v}$, the corresponding output power with a specified beamforming weight vector $\mathbf{w}$ is proportional to $\mathbf{w}^{H}\mathbf{R}\mathbf{w}$. Thus the SNR becomes

$$\begin{aligned}\mathrm{SNR} &= \frac{P_{\mathrm{sig}}}{P_{\mathrm{n}}} \\ &= \frac{\mathbf{w}^{H}\mathbf{R}_{\mathrm{sig}}\mathbf{w}}{\mathbf{w}^{H}\mathbf{R}_{n}\mathbf{w}} \\ &= \frac{\mathbf{w}^{H}\mathbf{R}_{\mathrm{sig}}\mathbf{w}}{\mathbf{w}^{H}(\mathbf{R}_{\mathrm{sky}} + \mathbf{R}_{\mathrm{sp}} + \mathbf{R}_{\mathrm{loss}})\mathbf{w}}.\end{aligned} \tag{2.12}$$

2.2 Array Noise Model

For a transmitting array antenna with excitation current vector $\mathbf{i}_{\mathrm{A}}$, the total input power is

$$P_{\mathrm{in}} = \frac{1}{2}\mathbf{i}_{\mathrm{A}}^{H}\mathbf{Re}[\mathbf{Z}_{\mathrm{A}}]\mathbf{i}_{\mathrm{A}}. \tag{2.13}$$

From the conservation of energy, the array input power is either dissipated in the array in terms of ohmic, dielectric loss or radiated by the antennas in terms of far fields. This implies that

$$P_{\mathrm{in}} = P_{\mathrm{rad}} + P_{\mathrm{loss}}. \tag{2.14}$$

The total radiated power P_{rad} is

$$P_{\text{rad}} = \frac{1}{|I_0|^2}\mathbf{i}_{\text{A}}^H \mathbf{A}\mathbf{i}_{\text{A}}, \tag{2.15}$$

where $\mathbf{A}$ is the matrix of pattern overlap integral with elements given by

$$A_{mn} = \frac{1}{2\eta_0}\int \overline{E}_m(\bar{r})\cdot\overline{E}_n^*(\bar{r})r^2 d\Omega. \tag{2.16}$$

The antenna ohmic loss is

$$P_{\text{loss}} = \frac{1}{2}\mathbf{i}_{\text{A}}^H \mathbf{R}_{\text{loss}}\mathbf{i}_{\text{A}}. \tag{2.17}$$

From (2.13-2.17), for a lossless antenna the relationship between the array mutual scattering matrix $\mathbf{Z}_{\text{A}}$ and the array overlap matrix $\mathbf{A}$ is

$$\mathbf{A} = \frac{1}{2}|I_0|^2\text{Re}[\mathbf{Z}_{\text{A}}]. \tag{2.18}$$

This means the array radiation field pattern overlap matrix is proportional to the real part of the mutual impedance matrix or mutual resistance matrix.

Considering an array antenna in thermal equilibrium with an isotropic noise environment at temperature T_{iso}, the total thermal noise correlation matrix becomes

$$\mathbf{R}_{\text{t}} = 8k_{\text{b}}T_{\text{iso}}B\mathbf{Q}\text{Re}[\mathbf{Z}_{\text{A}}]\mathbf{Q}^{\text{H}}. \tag{2.19}$$

Without considering the antenna loss, the contribution from the external isotropic noise alone becomes

$$\mathbf{R}_{\text{ext,iso}} = \frac{1}{|I_0|^2}16k_{\text{b}}T_{\text{iso}}B\mathbf{Q}\mathbf{A}\mathbf{Q}^H. \tag{2.20}$$

The difference between $\mathbf{R}_{\text{t}}$ and $\mathbf{R}_{\text{iso}}$ is due to the antenna loss, which can be written as

$$\mathbf{R}_{\text{loss}} = 8k_{\text{b}}T_{\text{a}}B\mathbf{Q}\mathbf{R}_{\text{loss}}\mathbf{Q}^H, \tag{2.21}$$

where T_a is the physical temperature of the array elements.

Similar to the pattern overlap integral matrix in Equation 2.16, the spillover overlap integral matrix with elements can be written as

$$A_{\mathrm{sp},mn} = \frac{1}{2\eta_0} \int_{\Omega_{\mathrm{sp}}} \overline{E}_m(\bar{r}) \cdot \overline{E}_n^*(\bar{r}) r^2 d\Omega, \tag{2.22}$$

where Ω_{sp} is a spillover solid angle from the feed to the reflector antenna. The spillover correlation matrix is

$$\mathbf{R}_{\mathrm{sp}} = \frac{1}{|I_0|^2} 16 k_\mathrm{b} T_{\mathrm{iso}} B \mathbf{Q} \mathbf{A}_{\mathrm{sp}} \mathbf{Q}^H. \tag{2.23}$$

If the physical noise temperature T_{sp} changes over Ω_{sp}, or nonuniform sky noise temperature distribution, the spillover noise correlation matrix is

$$R^{\mathrm{oc}}_{\mathrm{sp,mn}} = \frac{8 k_\mathrm{b} B}{\eta_0 |I_0|^2} \int T(\Omega) \overline{E}_m(\bar{r}) \cdot \overline{E}_n^*(\bar{r}) r^2 d\Omega. \tag{2.24}$$

2.3 Figures of Merit

From the above analysis of the radiation performance for a phased array feed, we define the radiation efficiency, aperture efficiency, spillover efficiency, system noise temperature and sensitivity in this section.

2.3.1 Aperture Efficiency

The overlap matrix with elements is given by

$$A_{mn} = \frac{1}{2\eta} \int\limits_{\Omega} \overline{E}_m(\bar{r}) \cdot \overline{E}_n^*(\bar{r}) d\Omega, \tag{2.25}$$

where $\overline{E}_n(\bar{r})$ represents the open circuit loaded embedded element radiation field pattern of an array antenna. Because the main beam of the reflector antenna is much narrower than that of the array antenna, to increase the integral accuracy, the radiated field of the array antenna instead of the reflector antenna is used in the overlap integral.

The total radiated power is

$$P_{\text{rad}} = \frac{1}{|I_0|^2}\mathbf{w}^H\mathbf{A}\mathbf{w}, \tag{2.26}$$

where **w** is the array beamformer weights and I_0 is the input current to generate $\overline{E}_n(\bar{r})$.

The radiated power density in a given direction can be written as

$$S(\bar{r}) = \frac{1}{|I_0|^2}\mathbf{w}^H\mathbf{B}(\bar{r})\mathbf{w}, \tag{2.27}$$

where **B** is a matrix with elements given by

$$B_{mn}(\bar{r}) = \frac{1}{2\eta}\overline{E}_m(\bar{r})\cdot\overline{E}_n^*(\bar{r}), \tag{2.28}$$

$\overline{E}_n(\bar{r})$ represents the element radiated field when the array antenna is combined with the reflector antenna.

By combining the total radiated power from the array antenna and the power density from the reflector antenna, the directivity of the reflector antenna can be expressed as

$$D_r(\Omega) = \frac{4\pi r^2\mathbf{w}^H\mathbf{B}(\bar{r})\mathbf{w}}{\mathbf{w}^H\mathbf{A}\mathbf{w}}. \tag{2.29}$$

The standard directivity of a reflector antenna is defined as the aperture of a reflector antenna uniformly illuminated by an incident field, which can be written as

$$D_s(\Omega) = 4\pi\frac{\mathrm{A}}{\lambda^2}, \tag{2.30}$$

where A is the aperture area of the reflector antenna, and λ is the wavelength of the electric field.

By combining the directivity of the PAF and the standard directivity of the reflector antenna, the aperture efficiency can be written as

$$\eta_{\text{ap}} = \frac{D_r}{D_s}. \tag{2.31}$$

To achieve the maximum aperture efficiency, the optimal beamformer weights are

$$\mathbf{w} = \mathbf{A}^{-1}\mathbf{E}(\bar{r}), \tag{2.32}$$

where **E** represents the open circuit loaded embedded element radiated field of an array element combined with a reflector antenna.

2.3.2 Antenna Efficiency

Single Antennas

In a given direction, the antenna effective area A_{e} is defined as the ratio of the available power $P_{\mathrm{sig}}^{\mathrm{av}}$ at the terminals of a receiving antenna to the power flux density S^{sig} of a plane wave incident on the antenna from that direction and aligned with polarization by

$$A_{\mathrm{e}} = \frac{P_{\mathrm{sig}}^{\mathrm{av}}}{S^{\mathrm{sig}}}. \tag{2.33}$$

The effective area is related to the antenna gain G and the operating wavelength λ by

$$A_{\mathrm{e}} = \frac{\lambda^2}{4\pi}G. \tag{2.34}$$

Antenna efficiency measures the efficiency of an antenna receiving an incident electromagnetic wave. Antenna efficiency is related to radiation efficiency η_{rad} and aperture efficiency η_{ap}. The antenna efficiency is written as the ratio of the effective area and the antenna physical aperture area A_{phy} by

$$\eta_{\mathrm{ant}} = \frac{A_{\mathrm{e}}}{A_{\mathrm{phy}}}.$$

Antenna efficiency can also be considered as the ratio of the available power at the antenna output port to the incident power P^{inc} on the antenna physical aperture by

$$\begin{aligned}\eta_{\text{ant}} &= \frac{P_{\text{sig}}^{\text{av}}}{S^{\text{sig}}A_{\text{phy}}} \\ &= \frac{P_{\text{sig}}^{\text{av}}}{P^{\text{inc}}}.\end{aligned} \tag{2.35}$$

The antenna radiation efficiency η_{rad} can be written as the ratio of the antenna radiated power to the antenna input power by

$$\eta_{\text{rad}} = \frac{P_{\text{rad}}}{P_{\text{in}}}. \tag{2.36}$$

Antenna aperture efficiency is independent of the antenna radiation efficiency η_{rad} and impedance match between the antenna and the antenna load. It can be written as

$$\eta_{\text{ap}} = \frac{D}{D_{\text{std}}}, \tag{2.37}$$

where D is the antenna directivity at a given direction and D_{std} is the standard directivity which is defined as the maximum directivity from a planar aperture of area A, or from a line source of length L, when excited with a uniform-amplitude, equiphase distribution. Antenna efficiency is relative to aperture efficiency and radiation efficiency by

$$\eta_{\text{ant}} = \eta_{\text{rad}}\eta_{\text{ap}}. \tag{2.38}$$

Phased Array Feeds

In this section, we will extend the definitions of the figure of merits of from a single antenna to an active array feed. As shown in Figure 2.2a, in an isotropic thermal noise environment with brightness temperature T_{iso} and thermal equilibrium, the available input noise power at the antenna port is

$$P_{\text{n}}^{\text{in}} = k_{\text{b}}T_{\text{iso}}B. \tag{2.39}$$

For the noise response, the array output power becomes

$$P_{\mathrm{n}}^{\mathrm{out}} = \mathbf{w}^{H}\mathbf{R}_{\mathrm{t}}\mathbf{w}. \tag{2.40}$$

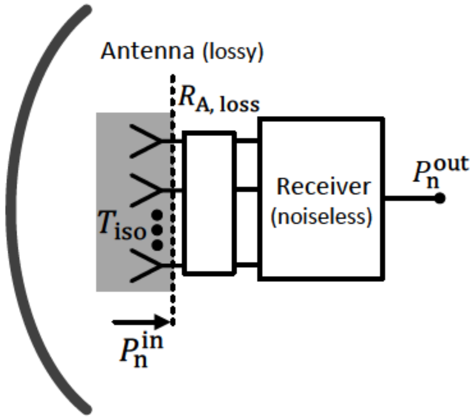

(a) External noise response.

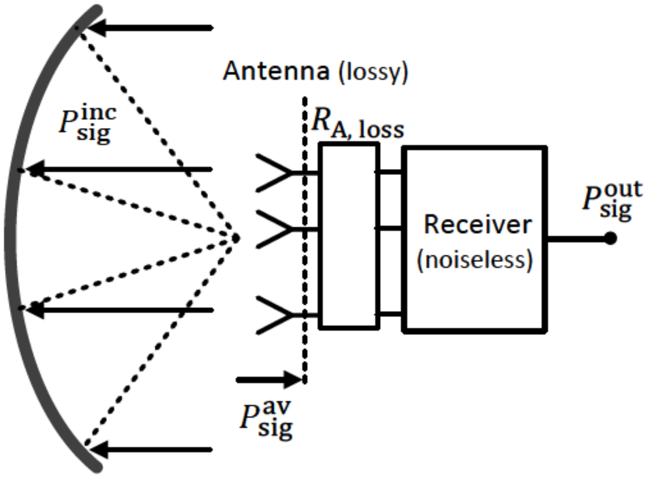

(b) Available signal response.

Figure 2.2: Beamforming array receiver system response block diagram.

As shown in Figure 2.2b, the total incident power on the reflector antenna is

$$P_{\mathrm{sig}}^{\mathrm{inc}} = S^{\mathrm{sig}}A_{\mathrm{phy}}. \tag{2.41}$$

The available power at the antenna port is $P_{\text{sig}}^{\text{av}}$. Similar to the noise power response, the signal power response at the array output becomes

$$P_{\text{sig}}^{\text{out}} = \mathbf{w}^H \mathbf{R}_{\text{sig}} \mathbf{w}. \tag{2.42}$$

Since the antennas and receivers are a linear system, there is a constant scaling factor between the input power on the antenna ports and the array output power by

$$\frac{P_{\text{n}}^{\text{in}}}{P_{\text{n}}^{\text{out}}} = \frac{P_{\text{sig}}^{\text{av}}}{P_{\text{sig}}^{\text{out}}}. \tag{2.43}$$

Solving for the available power leads to

$$P_{\text{sig}}^{\text{av}} = k_{\text{b}} T_{\text{iso}} B \frac{\mathbf{w}^H \mathbf{R}_{\text{sig}} \mathbf{w}}{\mathbf{w}^H \mathbf{R}_{\text{t}} \mathbf{w}}. \tag{2.44}$$

Combined with (2.35) and (2.44), antenna efficiency for an array feed can be written as

$$\eta_{\text{ant}} = \left(\frac{k_{\text{b}} T_{\text{iso}} B}{S_{\text{sig}} A_{\text{phy}}} \right) \left(\frac{\mathbf{w}^H \mathbf{R}_{\text{sig}} \mathbf{w}}{\mathbf{w}^H \mathbf{R}_{\text{t}} \mathbf{w}} \right). \tag{2.45}$$

Aperture efficiency becomes

$$\eta_{\text{ap}} = \left(\frac{k_{\text{b}} T_{\text{iso}} B}{S_{\text{sig}} A_{\text{phy}}} \right) \left(\frac{\mathbf{w}^H \mathbf{R}_{\text{sig}} \mathbf{w}}{\mathbf{w}^H \mathbf{R}_{\text{iso}} \mathbf{w}} \right), \tag{2.46}$$

and radiation efficiency is

$$\begin{aligned} \eta_{\text{rad}} &= \frac{\mathbf{w}^H \mathbf{R}_{\text{iso}} \mathbf{w}}{\mathbf{w}^H \mathbf{R}_{\text{t}} \mathbf{w}} \\ &= \frac{\mathbf{w}^H \mathbf{R}_{\text{iso}} \mathbf{w}}{\mathbf{w}^H (\mathbf{R}_{\text{iso}} + \mathbf{R}_{\text{loss}}) \mathbf{w}}. \end{aligned} \tag{2.47}$$

2.3.3 Spillover Efficiency and Spillover Noise Temperature

For a transmitting antenna, spillover efficiency describes how much radiated power of the array feed is received by the reflector antenna. For a transmitting phased array feed, the spillover efficiency is

$$\eta_{\mathrm{sp}} = 1 - \frac{P_{\mathrm{spill}}}{\mathrm{P}_{\mathrm{rad}}}. \tag{2.48}$$

Solving the available power, the spillover efficiency becomes

$$\eta_{\mathrm{sp}} = 1 - \frac{\mathbf{w}^H\mathbf{Q}\mathbf{A}_{\mathrm{sp}}\mathbf{Q}^H\mathbf{w}}{\mathbf{w}^H\mathbf{Q}\mathbf{A}\mathbf{Q}^H\mathbf{w}}.$$

If the sky noise temperature is constant over the solid angle Ω_{sp}, the spillover efficiency can be written as

$$\eta_{\mathrm{sp}} = 1 - \frac{\mathbf{w}^H\mathbf{R}_{\mathrm{sp}}\mathbf{w}}{\mathbf{w}^H\mathbf{R}_{\mathrm{iso}}\mathbf{w}} \tag{2.49}$$

and spillover noise temperature becomes

$$\begin{aligned} T_{\mathrm{sp}} &= T_{\mathrm{iso}}\frac{\mathbf{w}^H\mathbf{Q}\mathbf{A}_{\mathrm{sp}}\mathbf{Q}^H\mathbf{w}}{\mathbf{w}^H\mathbf{Q}\mathbf{A}\mathbf{Q}^H\mathbf{w}} \\ &= T_{\mathrm{iso}}\frac{\mathbf{w}^H\mathbf{R}_{\mathrm{sp}}\mathbf{w}}{\mathbf{w}^H\mathbf{R}_{\mathrm{iso}}\mathbf{w}}. \\ &= T_{\mathrm{iso}}(1-\eta_{\mathrm{sp}}) \end{aligned} \tag{2.50}$$

2.3.4 Receiver Noise Temperature

A PAF receiver system is a cascaded system consisting of low noise amplifiers (LNAs), downconverters, filters and power amplifiers with various gain and equivalent noise temperature. From the network theory, the total equivalent noise temperature for the receiver system is

$$T_{\mathrm{rec}} = T_1 + \frac{T_2}{G_1} + \frac{T_3}{G_2} + \cdots, \tag{2.51}$$

where T_1, T_2 and T_3 are equivalent noise temperatures of the first, second and third component of the system, and G_1 and G_2 are the gains of the first and second components, respectively.

From this formula we can find that the system equivalent noise temperature depends strongly on the equivalent noise temperature and gain of the first stage. To minimize the equivalent noise temperature of the PAF system, LNAs are used as the first stage for the receiver system. The equivalent noise temperature of a state-of-the-art LNA at L-band can be less than 10 K and the gain is 40 dB. This allows us to approximate T_{rec} as equal to T_{LNA}.

At this point, we will ignore the noise contributed by the other parts of the PAF chain system and assure that the equivalent receiver noise temperature is dominated by the LNAs. Similar to the definition of spillover noise temperature in equation 2.50, T_{LNA} can be written as

$$T_{\text{LNA}} = T_{\text{iso}}\left(\frac{\mathbf{w}^H\mathbf{R}_{\text{LNA}}\mathbf{w}}{\mathbf{w}^H\mathbf{R}_{\text{t}}\mathbf{w}}\right), \tag{2.52}$$

where $\mathbf{w}^H\mathbf{R}_{\text{t}}\mathbf{w}$ is the output power for a PAF system with isotropic noise temperature T_{iso} in Figure 2.2a and $\mathbf{w}^H\mathbf{R}_{\text{LNA}}\mathbf{w}$ is the PAF output noise power contributed by the LNAs.

The LNA noise correlation matrix $\mathbf{R}_{\text{LNA}}$ depends on the minimum amplifier noise temperature T_{min}, the impedance match between the antenna active impedance $Z_{\text{act,m}}$ and the amplifier optimal source impedance Z_{opt} [2].

2.3.5 Sensitivity

Sensitivity is a key figure of merit for a PAF system. It determines the weakest signal that can be detected by a radio astronomy receiver. High sensitivity requires maximizing the reflector aperture efficiency and minimizing the receiver system noise temperature. The sensitivity for a PAF system is proportional to the SNR at the receiver output with a conjugate matched load on the antenna terminals by

$$\text{SNR} = \frac{\eta_{\text{rad}}\eta_{\text{ap}}A_{\text{p}}S_{\text{sig}}}{k_{\text{B}}[\eta_{\text{rad}}(1-\eta_{\text{spill}})T_{\text{ground}} + \eta_{\text{spill}}\eta_{\text{rad}}T_{\text{sky}} + (1-\eta_{\text{rad}})T_{\text{p}} + T_{\text{rec}}]\text{B}}, \tag{2.53}$$

where A_{p} is the reflector aperture area, S_{sig} is the incident power density in one polarization, k_{B} is Boltzmann's constant, and B is the signal processing bandwidth of the receiver system.

From the above formula, we can find that the receiver output SNR can be optimized by considering the following factors:

1) *Radiation efficiency*: the received signal power and antenna noise temperature is influenced by the antenna radiation efficiency. For an array feed, the radiation efficiency can be maximized by using a high conductivity material for the antennas and reducing mutual couplings between each array elements.

2) *Reflector antenna size*: increasing the physical collecting area of the reflector antenna is helpful to receive more incident signal power, which is the main motivation for building very large dish antennas for radio astronomy observations. The diameter of a dish antenna can be up to 500 meters.

3) *Aperture efficiency*: aperture efficiency represents the utilization efficiency of the reflector antenna. The typical aperture efficiency for a single feed antenna is about 60%, but can be increased to 80% by careful design. For a phased array feed, aperture efficiency can be improved by increasing the element number for better sampling the Airy pattern, which describes the electric field distribution on the reflector focal plane. Ideally, ignoring the blockage effect of the feed system, a phased array feed with infinite array element could fully sample the Airy pattern, the aperture efficiency of which could be close to unity.

4) *System noise temperature*: spillover can be minimized by optimizing the feed radiation pattern to increase the aperture and spillover efficiency. Antenna loss can be reduced by increasing the antenna radiation efficiency and reducing the antenna environment brightness temperature by cryogenic cooling. Receiver noise temperature can be minimized by using an LNA with high gain and low noise temperature. The optimal noise temperature of LNAs can only be achieved when the antenna active impedance match to the LNAs optimal impedance Z_{opt}.

For a PAF with a given beam, the sensitivity can be defined as

$$S = \frac{A_e}{T_{sys}} \tag{2.54}$$

$$= \frac{k_{\mathrm{B}}B}{S_{\mathrm{sig}}}\left(\frac{\mathbf{w}^H\mathbf{R}_{\mathrm{sig}}\mathbf{w}}{\mathbf{w}^H\mathbf{R}_{\mathrm{n}}\mathbf{w}}\right). \tag{2.55}$$

The sensitivity of the phased array feeds is related to the beamformer weights. For the maximum SNR at the receiver output, the beamformer is given by

$$\mathbf{w}_{\mathrm{maxSNR}} = \mathbf{R}_{\mathrm{n}}^{-1}\mathbf{v}_{\mathrm{sig}}(\Omega_{\mathrm{s}}). \tag{2.56}$$

2.4 Summary

In this section, the figures of merits for an active receiving array feed system has been defined by correlation matrix, including aperture efficiency, spillover efficiency, radiation efficiency, equivalent system noise temperature and sensitivity.

CHAPTER 3. DESIGN AND ANALYSIS OF AN L-BAND PHASED ARRAY FEED SYSTEM

3.1 Introduction

An L-band 19-element dual-polarized phased array feed has been developed by the BYU/NRAO Radio Astronomy System Research group for the 100-meter Green Bank Telescope (GBT). GBT is the largest fully steerable telescope in the world. The dipole element structure and array element spacing were optimized to achieve the maximum sensitivity and field of view. In this chapter, single dipole element performance is studied including antenna impedance bandwidth, antenna loss improvement by electroplating, antenna weight reduction design, manufacture error and antenna S-parameter measurement. The aperture efficiency, system noise temperature and sensitivity performance for the PAF were analyzed using a noise model including the GBT reflector antenna. A downconverter system with 20-MHz bandwidth has been design and test.

3.2 GBT2 Antenna Element Analysis

3.2.1 Antenna Impedance Bandwidth

The PAF antenna element (GBT2 dipole) is an important part of a PAF system. It relates to system bandwidth, radiation pattern for beamforming and impedance matching to LNAs. A wideband dipole antenna was designed by David Carter and Taylor Webb by optimizing of the antenna dimension parameters [3, 4]. The goal of this design is to implement a dual-polarized wideband high efficiency dipole phased array feed for the Green Bank Telescope.

The GBT2 dipole antenna element comes from the optimization results designed by previous graduates students, the structure of which is less understood. In my work, to investigate the physical meaning of the antenna structure associated with well optimized performance, I compare the GBT2 dipole antena to other wideband antennas.

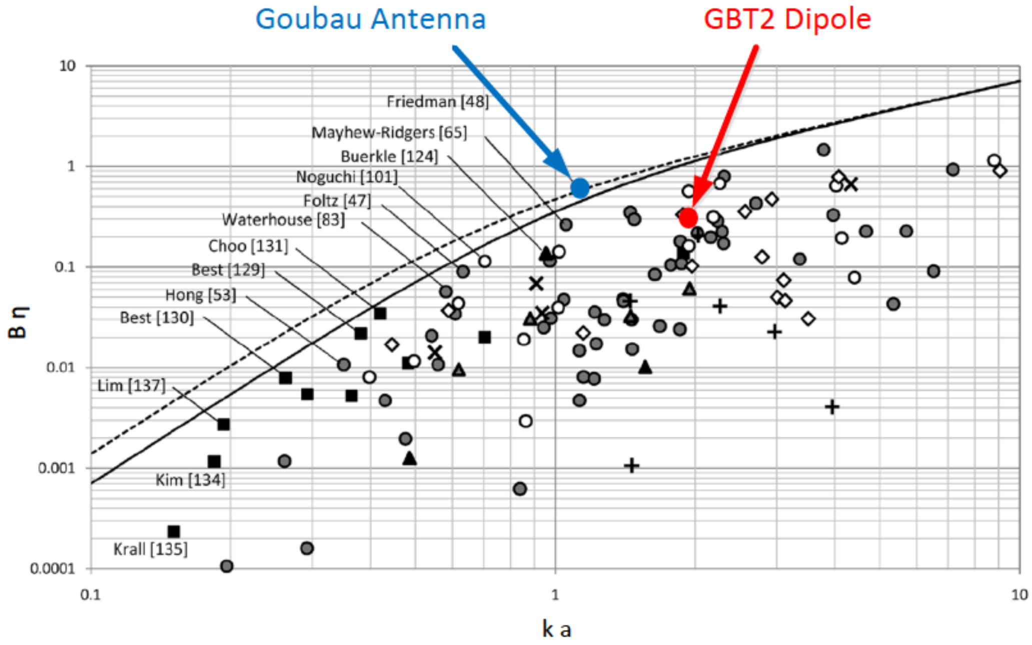

Figure 3.1: 112 selected small broadband antennas compared with the Wheeler-Chu limit [1].

The Wheeler-Chu limit gives a physical limit to the Q factor for a small antenna with an electrical size by [5]

$$Q = \frac{1}{ka} + \frac{1}{(ka)^3} \tag{3.1}$$

where a is the radius of a sphere used to cover the antenna and k is $2\pi/\lambda$.

Because the antenna bandwidth B and the antenna radiation efficiency η are related to Q factor, this equation becomes

$$B\eta = \frac{1}{\sqrt{2}}\left(\frac{1}{ka} + \frac{1}{n(ka)^3}\right)^{-1} \tag{3.2}$$

where n = 1 for linearly polarized or single-mode antennas, and n = 2 for circularly polarized or dual-mode antennas.

Based on the relationship between the antenna electrical size and the multiplication of bandwidth and radiation efficiency from the above formula, D. Sievenpiper et al. [1] compare 112 selected small broadband antennas published in the IEEE Transaction on Antennas and Propagation by the end of the year 2010. These results are shown in Figure 3.1, where it can be seen that all the antennas are below the physical limit.

Since the GBT2 dipole antenna is plated with copper, the radiation efficiency is closed to unity. The relationship between the electrical size and the bandwidth of GBT2 dipole antenna is shown in Figure 3.1. In this plot, the GBT2 dipole antenna has a larger bandwidth than the most antennas under the same electrical size.

In Figure 3.1, the Goubau antenna shows best performance. Figure 3.2 shows that the GBT2 dipole antenna has a similar structure to the Goubau antenna. Even though the Goubau antenna is closer to the physical limit, it is single polarized, so it is expected to have better performance than the dual-polarized GBT2 dipole antenna.

In terms of the wide bandwidth design, the structure of GBT2 dipole antenna shows the advantage of a low aspect ratio to fully utilize the spherical space of the antenna by a large flare angle and thick arms bending downward to the ground plane. The surface current is evenly distributed on the dipole arms, which increases of the antenna bandwidth.

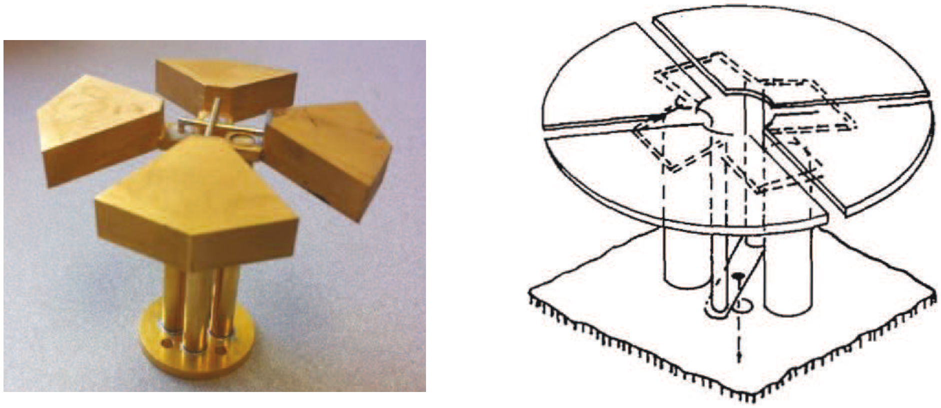

(a) GBT2 dipole antenna.

(b) Goubau antenna.

Figure 3.2: Structures of the GBT2 antenna element and the Goubau antenna.

3.2.2 Antenna Loss

Antenna loss noise temperature is an important contribution to the system noise budget. The antenna equivalent noise temperature is

$$T_{\mathrm{loss}} = (1 - \eta_{\mathrm{rad}})T_{\mathrm{p}} \tag{3.3}$$

where η_{rad} is the antenna radiation efficiency, and T_{p} is the antenna physical temperature. The radiation efficiency can be expressed as

$$\eta_{\mathrm{rad}} = \frac{R_{\mathrm{rad}}}{R_{\mathrm{rad}} + R_{\mathrm{ohmic}}} \tag{3.4}$$

where R_{rad} is the antenna radiation impedance and R_{ohmic} is the antenna ohmic loss.

Table 3.1: Material relative conductivity

Material	Conductivity
Silver	105%
Copper	100%
Gold	70%
Aluminum	61%
Brass	28%
Zinc	27%
Nickel	22%
Iron	17%
Tin	15%
Phosphor Bronze	15%
Lead	7%
Nickel Alum. Bronze	7%
Steel	3 to 15%

Antenna noise temperature can be reduced by decreasing the antenna ohmic loss. The relative conductivity for brass, copper and other materials are shown in Table 3.1. In order to reduce the fabrication cost of the antennas, brass is used to build the GBT2 dipole antennas and then electroplated with copper. Including the inner surface of the coaxial feed lines, 19 dipole antennas were electroplated by Gerry Petencin at NRAO, Green Bank, WV. A 6.35µm copper layer (about 3 skin depths at 1 GHz in copper) followed by about 1µm of gold layer was plated on the surface of the antennas. The thickness of the plating layer is less than the mechanical fabrication tolerance of the antennas, so the influence of the plating on the antenna electrical performance is small.

Another contribution to antenna loss is the dielectric loss of Teflon beads, which is used to fill the coax. This loss can be minimized by using air filled coax with two Teflon beads, one at either end of the line, to support the inner conductor in the coax.

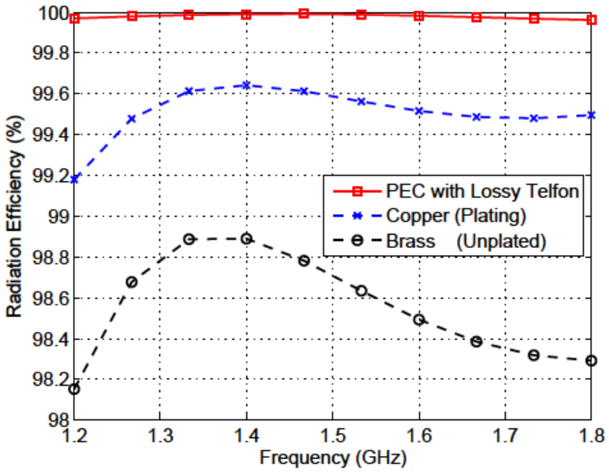

Figure 3.3: Simulated radiation efficiency of an antenna with various materials.

It is difficult to get an accurate radiation efficiency from a full-wave model, since there is only a small difference between the antenna input power and radiated power, and the difference is sensitive to numerical errors. To accurately model the radiation efficiency, it is necessary to improve the FEM model setup. The volume finite-conductivity material of an antenna is replaced by a surface finite-conductivity material to reduce the number of unknowns. The radiation boundary condition is expanded to increase the calculation accuracy of the radiation energy and the convergence speed. The number of mesh grid is increased to enhance the simulation accuracy.

Second-order basis functions are used for the analysis. With these settings, the accuracy of the numerical solution can be significantly improved.

The radiation efficiency of an isolated GBT2 dipole antennas with various materials over frequency are shown in Figure 3.3. The radiation efficiency is increased by about 1% when the antenna is plated with copper instead of brass. The system noise temperature can be reduced by about 3 K assuming the antennas are at the room temperature. This means a significant improvement to the system noise temperature can be achieved by electroplating, since the goal of the total system noise temperature is about 15 K.

3.2.3 Antenna Weight Reduction Design

In the initial design, the mechanical structure of the antenna was not strong enough to support the heavy arms of the dipole antennas, leading to a poor antenna mechanical strength. It is necessary to find a way to reduce the weights of dipole arms without influencing the PAF performance. The impedance and radiation pattern of the antennas depend on the surface current distribution on the top of dipole arms. The antenna arm weight can be reduced by drilling holes on the bottom of dipole arms. Figure 3.4 shows various methods of drilling circular holes and along-edge holes on the bottom of dipole arms, which can reduce the weight of arms by 50% and 75% respectively. The calculated aperture efficiency and sensitivity are shown in Figure 3.5. The drilled holes has no influence on the these figures of merit. Since drilling in the along-edge holes is much harder than that of the circular holes, circular holes on the bottom of dipole arms were used to reduce the antenna weight.

3.2.4 Antenna Measurement

GBT2 dipole antennas were fabricated by the Precision Machining Lab (PML) at BYU and also at the National Radio Astronomy Observatory (NRAO). Because the input impedance of the antennas is sensitive to the machining accuracy, it was necessary to measure the size of the manufactured antennas to verify fabrication tolerances. A photogrammetry method was used to compare the designed size to the manufactured size. As shown in Figure 3.6, a long zoom camera is used to take a picture of an antenna from the boresight direction. In order to make sure the

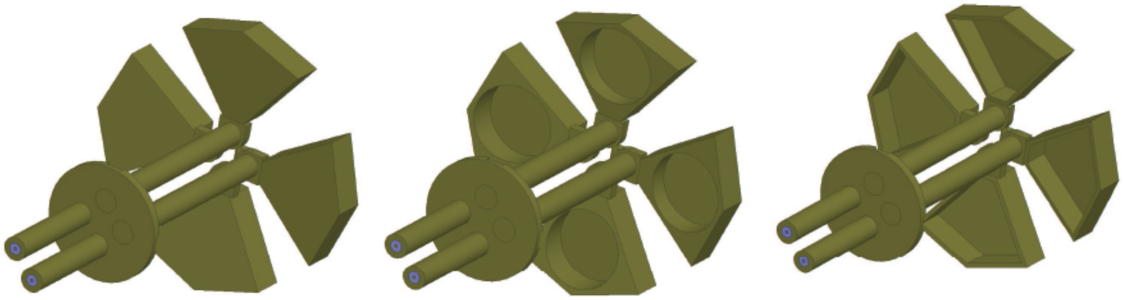

(a) Original design. (b) Drilled circular holes. (c) Drilled along-edge holes.

Figure 3.4: Antenna weight reduction schemes.

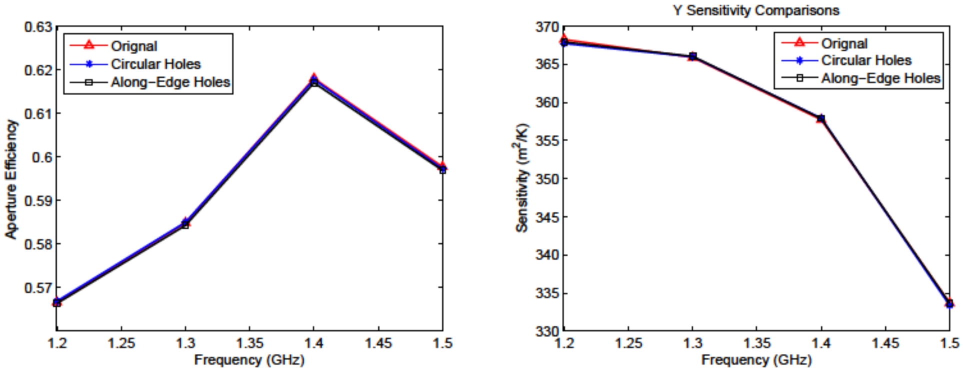

(a) Sensitivity. (b) Aperture efficiency.

Figure 3.5: Comparisons of figures of merit between the original design and the modified design with circular holes and along-edge holes.

camera is directly overhead of the antenna, a reference line below the antenna is used to make it overlap with an edge of the dipole arm in the picture. Figure 3.7 shows a top view comparison between the designed structure and the manufactured structure by photogrammetry, where there are slight manufacturing errors.

Figure 3.8 shows the impedance test setup for the GBT2 dipole antennas. With a large copper ground plane, an antenna is put into a wood box with absorber material around it. A comparison of S_{11} and S_{22} between the test results of 19 dipole antennas and the corresponding HFSS simulation result are shown in Figure 3.8. The simulated center frequency is always lower than the test frequency, which might be attributed to the inaccuracy of HFSS simulation results or manufacturing errors. Possible manufacturing errors include dimension and rotational angle error

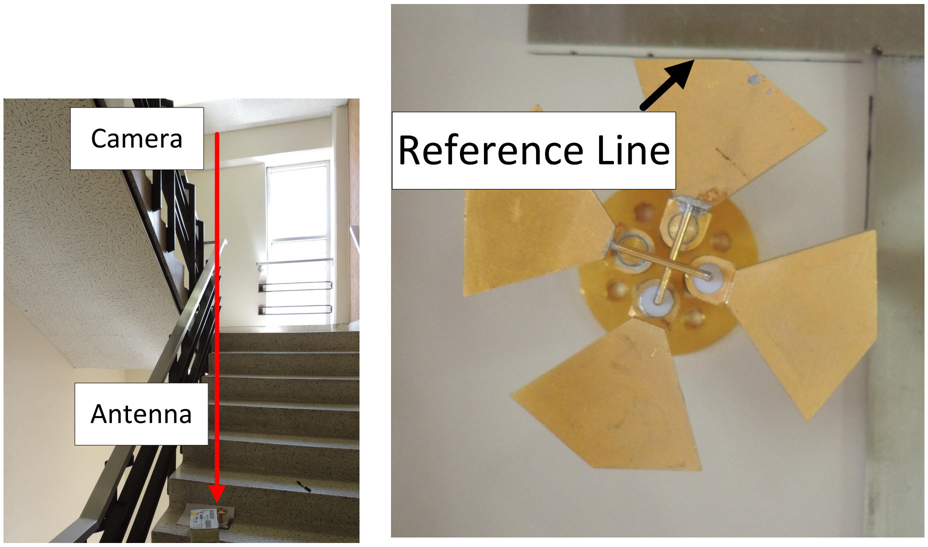

(a) Measurement Setup. (b) Top view of an antenna.

Figure 3.6: Photogrammetry for measuring the GBT2 dipole antenna dimension.

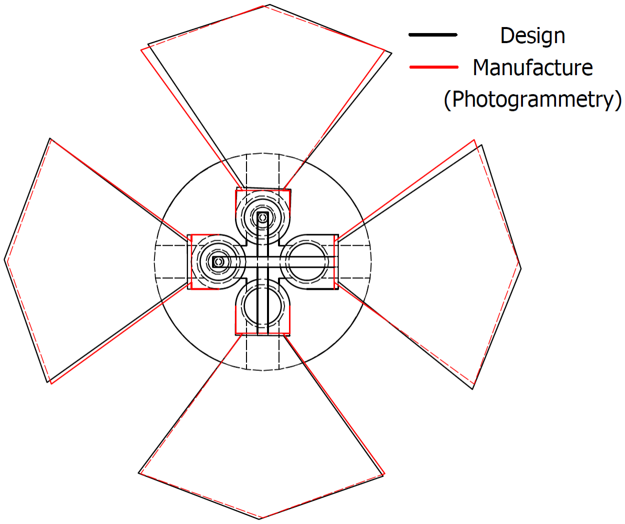

Figure 3.7: Comparison of designed structure to manufactured structure using photogrammetry.

of the dipole arms, position error of the inner conductor in the coax that is not perfectly centered and dielectric constant error of Teflon beads in the coax.

Figure 3.8: Photographs of S-parameter test in an anechoic chamber.

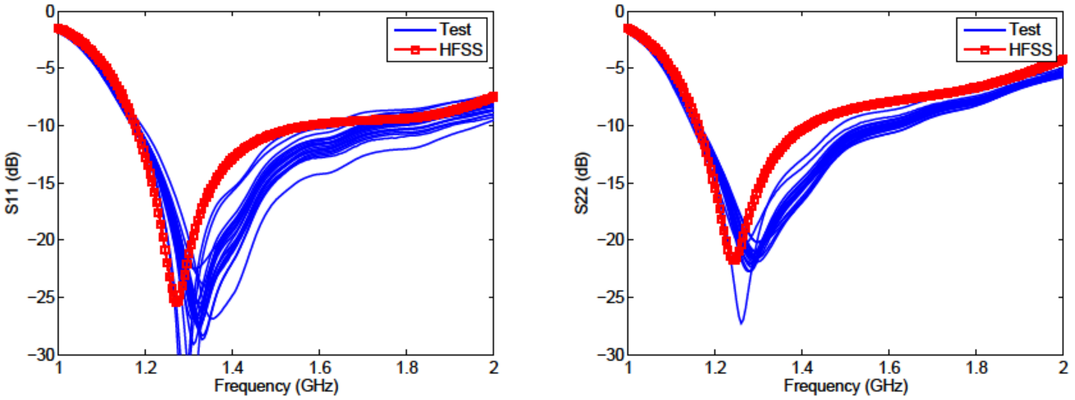

(a) S11

(b) S22

Figure 3.9: Comparison of simulated and measured S-parameters. Port 1 and 2 are the two orthogonal polarization ports.

3.3 GBT2 Phased Array Feed Analysis

A 19-element GBT2 dual-pol dipole array with $0.7\lambda_0$ (the center frequency is at 1.4 GHz) element spacing is analyzed with a noise model in the presence of a reflector antenna. The calculated LNAs noise temperature for each element are shown in Figure 3.10. This plot shows a low noise temperature level in the range of the frequencies of interest (from 1.2 GHz to 1.8 GHz). The increased noise level at the bound of the frequency bandwidth is due to the impedance mismatch between the optimal impedance of LNAs and the embedded element active impedance. At the low frequency range, stronger mutual coupling effects make the impedance mismatch issue worse, leading to a higher LNA noise temperature.

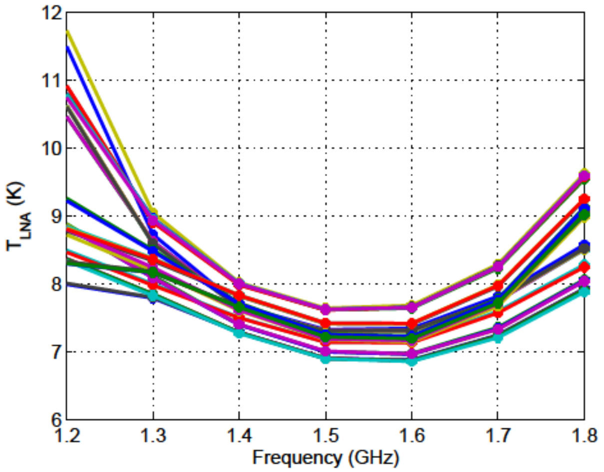

Figure 3.10: LNAs noise temperature of each antenna element.

Figure 3.11 shows the calculated figures of merits for the boresight formed beam using the maximum sensitivity beamformer and the center element beam at the boresight direction, respectively. Since the beamformer coefficient weight vector is used to optimize the array radiation pattern and impedance, the figures of merit for the formed beam are better than that of the center element beam. The only exception is in Figure 3.11a, where the aperture efficiency of the center element is slightly higher than that of the formed beams at the high frequency range. The reason is that high spillover efficiency compensates for the decrease of aperture efficiency and leads to a high $T_{\text{sys}}/\eta_{\text{ap}}$ in Figure 3.11c.

Using the same noise model, $T_{\text{sys}}/\eta_{\text{ap}}$ for a GBT2 array feed with $0.52\lambda_0$ element spacing is shown in Figure 3.12. The reason for the higher $T_{\text{sys}}/\eta_{\text{ap}}$ for the $0.52\lambda_0$ element spacing at low frequency is due to the stronger mutual-coupling effects increasing the noise temperature of the LNAs. Meanwhile, $T_{\text{sys}}/\eta_{\text{ap}}$ at the X and Y polarizations for the GBT2 array feed with $0.7\lambda_0$ element spacing is compared to a Kite array feed in Figure 3.13.

3.4 Downconverter System Design and Analysis

A downconverter with 64 independent channels has been developed to mix down, filter, and amplify the signals of interest. The inputs for the downconverter system are L-band radio frequency (RF) signals which is received by antennas and then amplified by the LNAs. The output

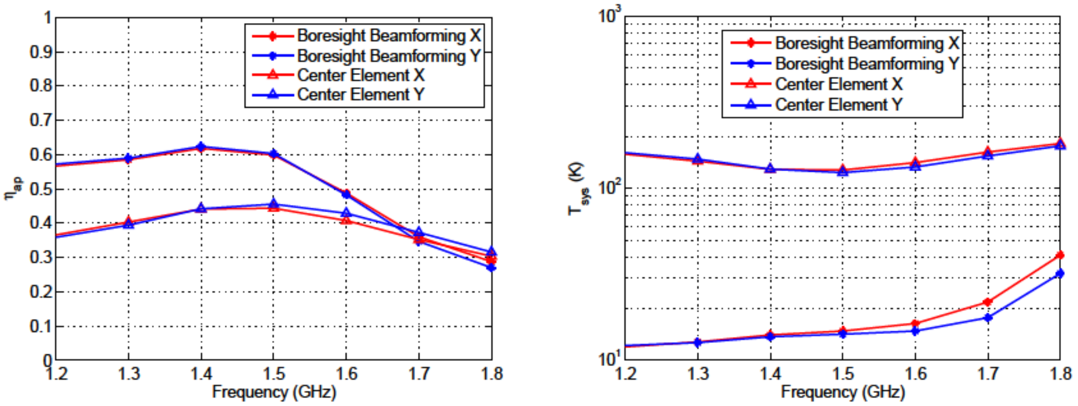

(a) Aperture efficiency

(b) System noise temperature

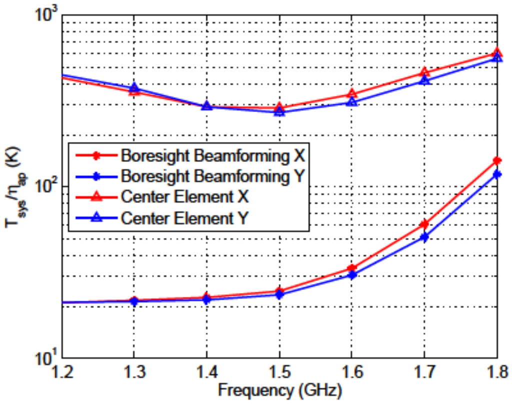

(c) T_{sys}/η_{ap}

Figure 3.11: Comparisons of figures of merit at the boresight direction for the x and y polarization between a boresight formed beam and a center element beam. The element spacing for the 19 element dual-pol GBT2 array feed is $0.7\lambda_0$, the center frequency of which is at 1.4 GHz

.

signal is intermediate frequency (IF) signals, which are transmitted to the digital processing system. Figure 3.14a shows the pictures of the downconverter system in a rack, which includes power supply, local oscillator (LO) distribution network, analog receiver cards, and signal generators.

The block diagram for the down converter system is shown in Figure 3.14b. The signal generators produce two pure tone signals for LO distribution. The frequency of LO1 depends on the frequency of the input signal. The frequency for LO2 is fixed at 442.5 MHz. After being amplified and split the signals are distributed to the LO inputs at each receiver card. The analog receiver cards are used to convert the signals from RF frequency to IF frequency. A power supply

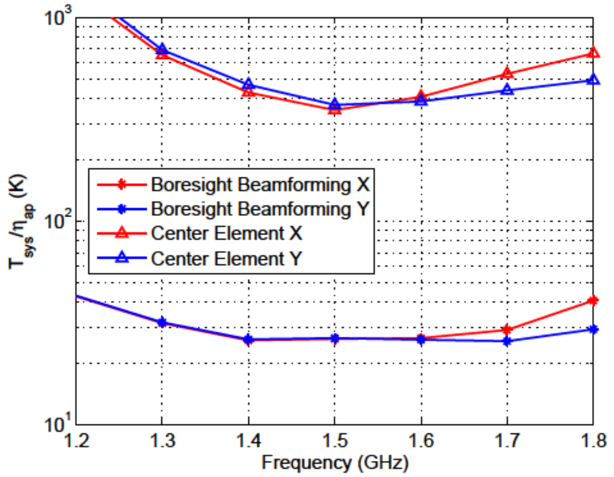

Figure 3.12: Comparison of $T_{\mathrm{sys}}/\eta_{\mathrm{ap}}$ for GBT2 array feed with $0.52\lambda_0$ element spacing.

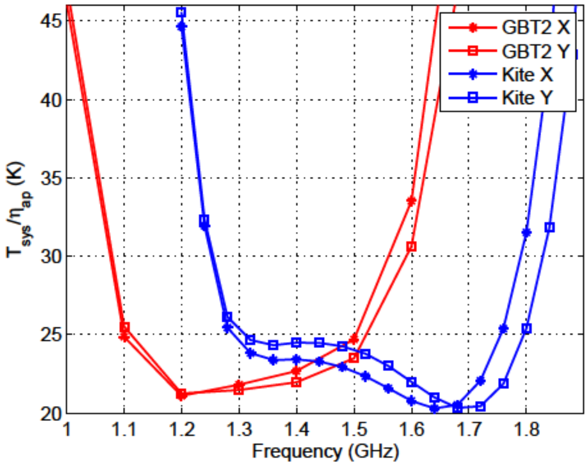

Figure 3.13: Comparison of $T_{\mathrm{sys}}/\eta_{\mathrm{ap}}$ for GBT2 PAF with $0.7\lambda_0$ element spacing to Kite PAF.

is used to produce a stable voltage for each receiver card and amplifier in the LO distribution network.

3.4.1 Power Supply

Power supply used in the downconverter system is shown in Figure 3.15. A 5 V output voltage supplies for the amplifiers of LO distribution and a 12 V output voltage supplies for the receiver cards. The output currents for the power supplies are below the measured maximum

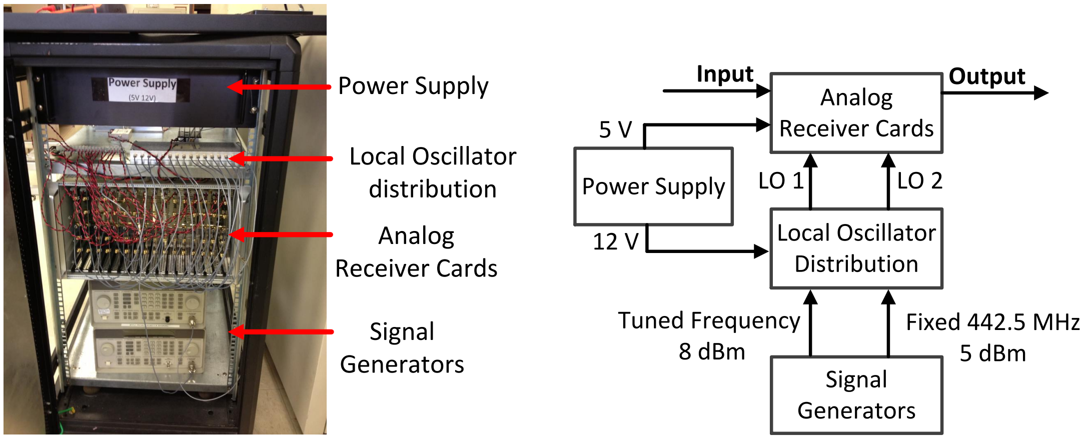

(a) Picture.

(b) Block diagram.

Figure 3.14: Configuration of downconverter system.

current of the LNAs and receiver cards. Because heat is produced by the power supply, heat dissipation is a key problem. This problem was solved by drilling holes on the top wall of the chassis and adding a fan above the chassis to cool the power supply. Additionally, two LED indicators are used to show the working status of the power supply.

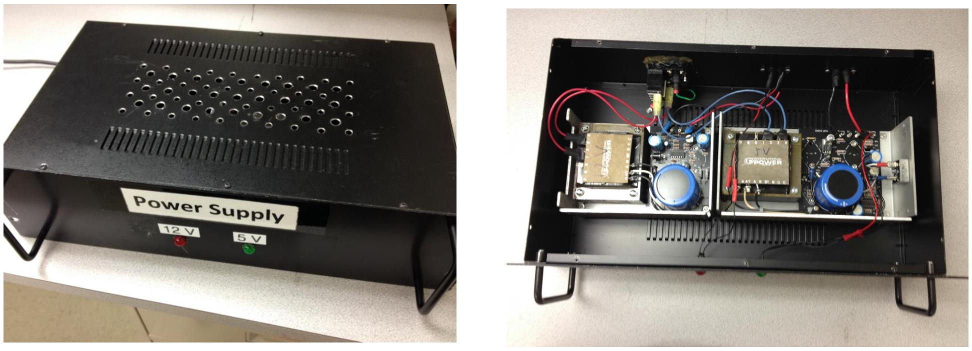

Figure 3.15: Power supply.

3.4.2 Local Oscillator Distribution Network

A picture of the LO distribution network and its block diagram are shown in Figure 3.16. The LO distribution network is designed to supply two signals (LO1 and LO2) for the LOs of each receiver cards. The input signals for LO1 and LO2 are generated by two signal generators, and the output power is 7 dBm for each 16 output port. The frequency of LO1 is determined by the frequency of input RF signal (2080 MHz for 1600 MHz input signal). The frequency of LO2 is fixed at 442.5 MHz.

Because the maximum output power of the signal generator is about 15 dBm, power amplifiers are needed to ensure that there is enough power for each of 16 outputs of the LO distribution network. The output 1 dB compression point (P1dB) of the power amplifier for LO2 (ZHL-2010) is about 30 dBm, which is enough to provide 7 dBm power signal for the 16 channels. However the output P1dB of the power amplifier (ZRL-3500) for LO1 is about 21 dBm, which fail to satisfy the required power for the 16 channels if including the losses of the cables and power splitters. Since the power amplifier with a high output P1dB is expensive, we use an additional 2-way power splitter and each path is connected to one power amplifier (ZRL-3500).

3.4.3 Analog receiver Cards

Analog receiver cards are used to filter, downconvert, and amplify the signals coming from the LNAs to the digital processing system. Figure 3.17 shows narrow-band receiver cards designed by Vikas Asthana and wide-band receiver cards designed by Michael Elmer. Each receiver card has four independent paths and block diagrams and one of the path is shown in Figure 3.18.

For the narrow-band receiver cards, the L-band RF input signal is mixed down to an IF signal having 2.8 MHz center frequency with 425 kHz bandwidth. For the wide-band receiver cards, the output IF signal is 20 MHz bandwidth centered at 37.5 MHz. Calculated and test results of gain, noise figure, and noise temperature of one receiver path are shown in Figure 3.18.

The Y-factor technique is used to measure the noise figure using a noise source (Agilent 346A). The excess noise ratio (ENR) of the noise source is 5.44 dB at 1.6 GHz. The noise figure (NF) can be calculated by

$$\mathrm{NF(dB)} = \mathrm{ENR} - 10\log_{10}(\mathrm{Y}-1) \tag{3.5}$$

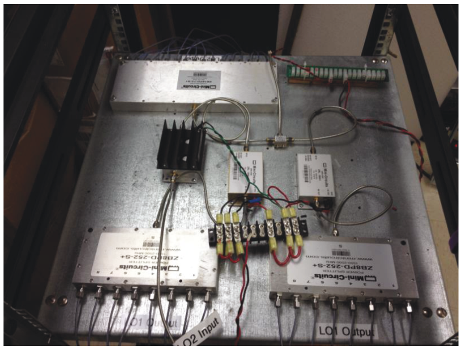

(a) Picture for local oscillator distribution.

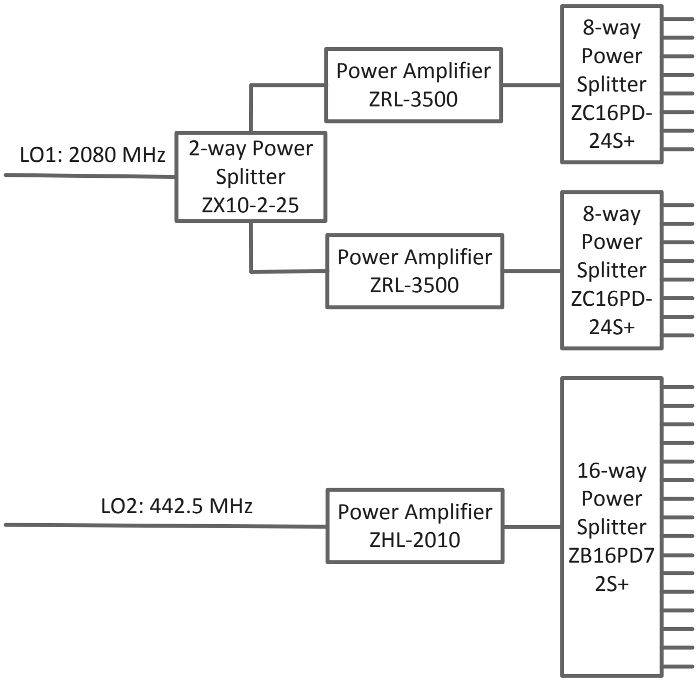

(b) Block diagram for local oscillator distribution.

Figure 3.16: Local oscillator distribution for wide-band receiver cards.

and the system noise temperature is

$$T_e = T_0(10^{\mathrm{NF(dB)}/10} - 1), \tag{3.6}$$

where T_0 represents the room temperature.

The test results for the noise temperature and noise figure for both receiver cards are higher than the calculated results. Possible reasons are the impedance mismatch and the dielectric and ohmic loss of the receiver PCB cards.

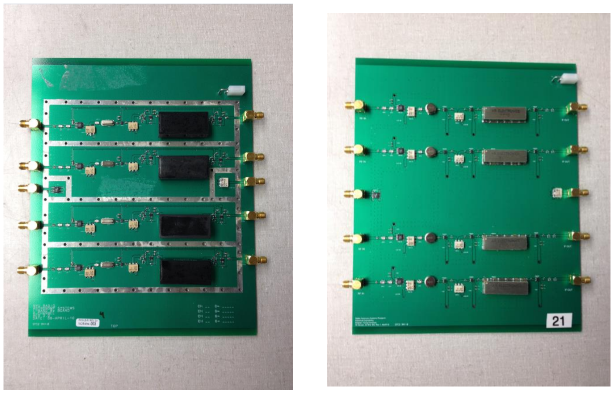

(a) Narrow-band. (b) Mid-band.

Figure 3.17: Pictures of analog receiver cards.

3.4.4 System Analysis

Narrow-band and wide-band receiver cards are used for experimental observations on the Green Bank Telescope and Arecibo Telescope. For each channel, the received signal will be amplified and transmitted to the receivers by lossy cables. Since the receiver input power must be less than the system P1dB to avoid harmonic waves, the power and noise flow in both systems are analyzed. A block diagram for the Green Bank system is shown in Figure 3.19.

The noise temperature for the input signal is assumed to be 25 K, and the corresponding power density is -184 dBm/Hz. After being amplified, filtered, and attenuated, the final power before the receiver is -90 dBm/Hz, which is higher than the 1 dB compression point of the receiver (-113 dBm/Hz), so that an 30 dB attenuator is needed prior to the receiver. Since the noise temperature for a cascade system depends on the gain and noise of the first stage of the system, the system noise temperature is increased from the 30 dB attenuator can be ignored. A similar approach is applied to the Arecibo Telescope analysis in Figure 3.20, and a 10 dB attenuator is used prior to the receiver.

3.5 Summary

A 19-element L-band phased array feed designed for the Green Bank Telescope has been analyzed and tested. Wide bandwidth performance for the GBT2 dipole is due to the advantage of the dipole arms with wide spread angles, which is helpful to fully utilize the space around the antenna. The antenna structure is electroplated by a copper material. Manufacturing errors for the dipole antenna have been measured using photogrammetry and the antenna S-parameters match well with the simulated results. Figures of merit for the L-band phased array feed have been analyzed using a noise model with the GBT reflector. A 20-MHz bandwidth downconverter system has been designed and measured, and has been successfully used at the Green Bank Telescope and Arecibo Telescopes [6].

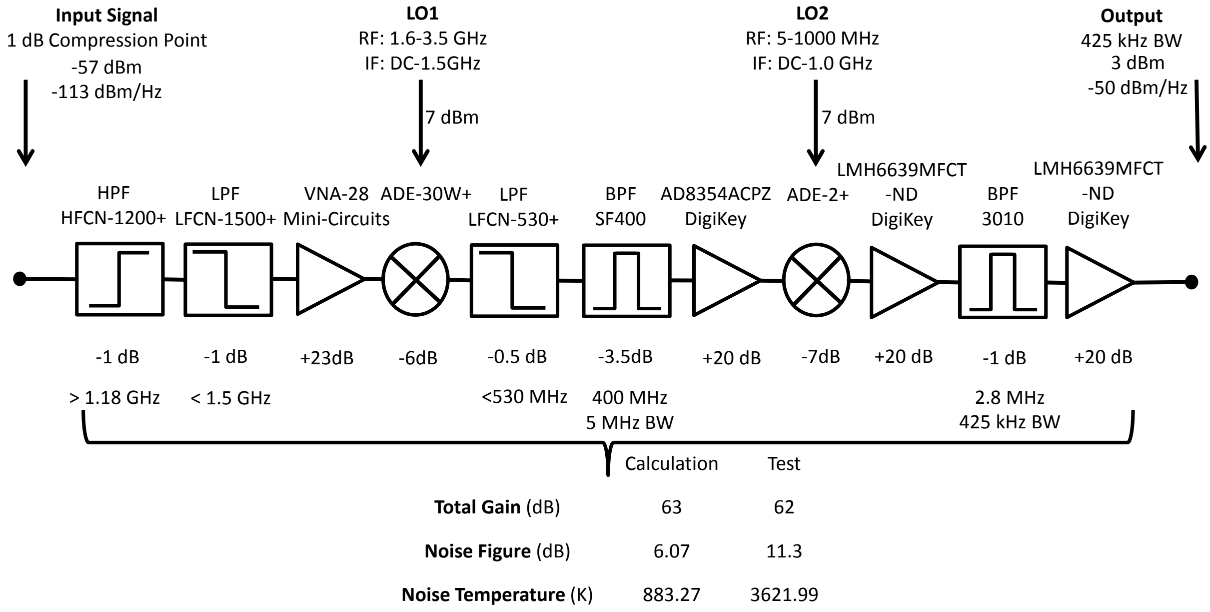

(a) Narrow-band.

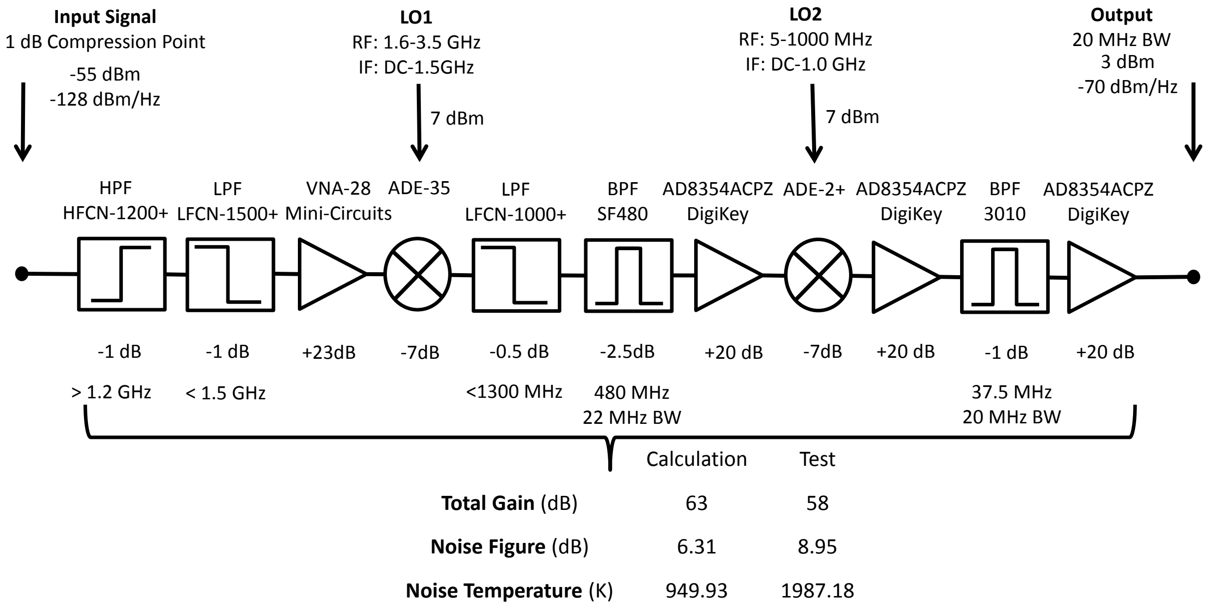

(b) Mid-band.

Figure 3.18: Block diagrams of analog receiver cards.

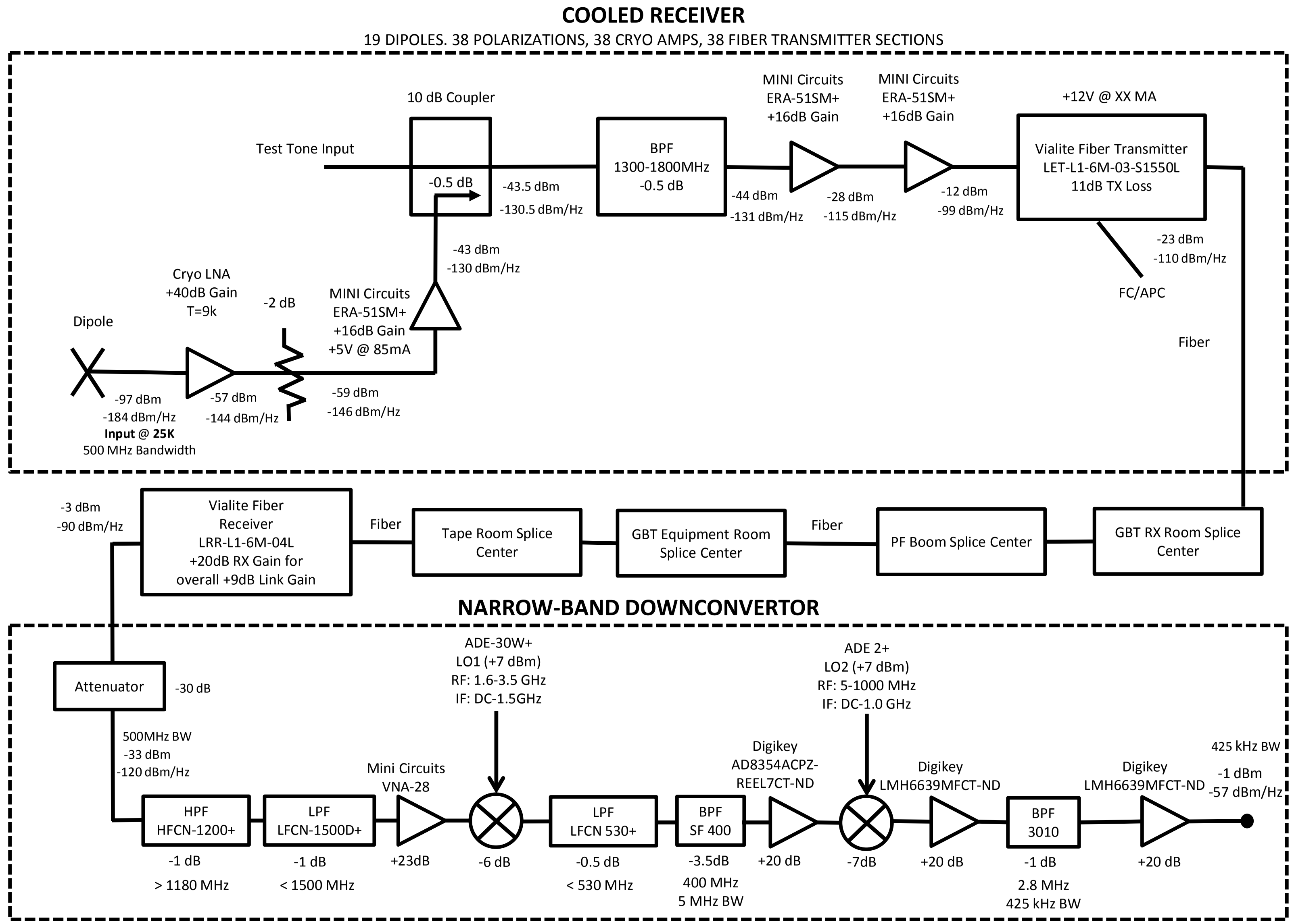

Figure 3.19: Block diagram of GBT PAF receiver system.

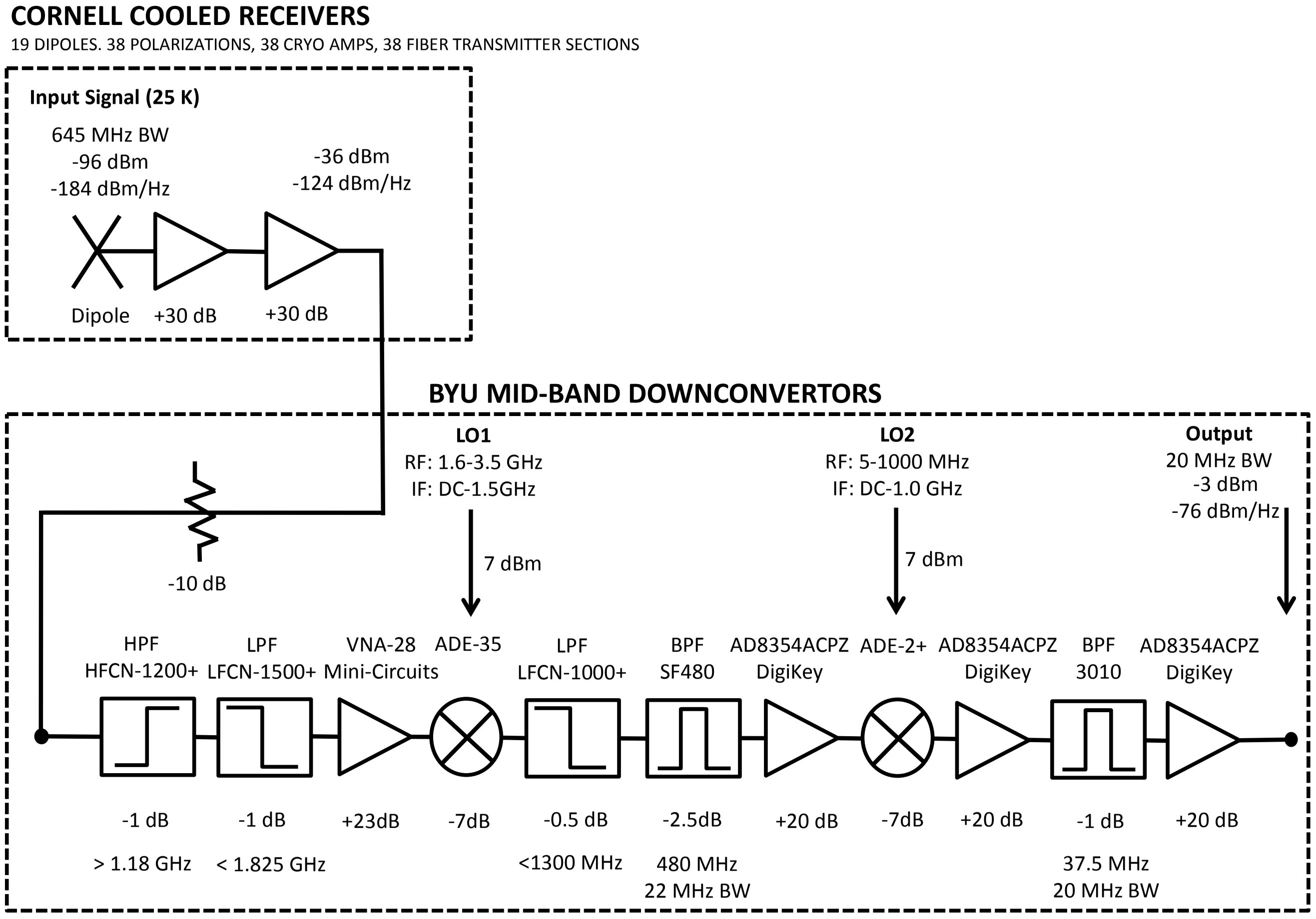

Figure 3.20: Block diagram of Arecibo PAF receiver system.

CHAPTER 4. ANALYSIS AND TESTING OF A 64-ELEMENT MM-WAVE CRYOGENIC PHASED ARRAY FEED FOR THE GREEN BANK TELESCOPE

4.1 Introduction

The spectrum between 30 GHz and 300 GHz is defined as mm-wave band, which corresponds to the wavelength from one to ten millimeters. Mm-wave radio astronomy is a powerful tool for studying the characteristics of enormous cold gas clouds where stars form. Such clouds are as cold as 20 K, leading to microwave and mm-wave. There are many chemical reactions in these cold clouds, producing molecules which emit radio waves in the millimeter range. By studying these molecules, astronomers can learn physical conditions in these clouds and understand the evolution of galaxies and the formation of stars.

In the range from 70 GHz to 95 GHz in the mm-wave band, abundant molecules such as N_2H^+, HCN and HNC emit strong spectral lines that provide important astronomical information. In recent decades, receivers for phased array feeds (PAFs) have been successfully demonstrated for the centimeter band, but the smaller required element size at the 3-mm wavelength requires miniaturized electronics and micromachining that has only recently become practical. Monolithic amplifiers can be fabricated at 100 GHz, making a mm-wave receiver practical in terms of circuitry.

The Umass Radio Astronomy group has extensive experience on developing PAFs at 3-mm wavelength based using of Monolithic Microwave Integrated Circuit (MMIC) amplifiers. The BYU Radio Astronomy group has been working on constructing and deploying high sensitivity L-band PAFs for the Green Bank Telescope (GBT) and Arecibo Telescope for many years. The BYU Radio Astronomy group and the UMass Radio Astronomy group have collaborated on developing a mm-wave PAFs prototype.

The Umass Radio Astronomy group has developed a low-noise 8×8 mm cryogenic wide-band PAF system. BYU provided calibration, beamforming, and digital signal processing hardware. This prototype mm-wave PAF has been mounted and tested on the GBT 100-meter reflector, which is the largest fully steerable radio telescope in the world.

4.2 Isolated Single Antenna Analysis

4.2.1 Antenna Model

For an array antenna, in order to avoid grating lobes, the element spacing should be one half wavelength or less. Using current technology, it is difficult to fabricate a complete receiver with a cross section less than 3×3 mm. Since each receiver block is directly connected to each antenna element, the antenna element spacing should be larger than the receiver block length to have enough space for the front end of the electronic system. Due to this limit, the structure and size of the antenna element was optimized for best illumination pattern quality with the largest possibility element size.

The mm-wave phased array feed element was designed by Neal Erickson's research group in UMASS. Figure 4.1 shows the antenna element model, which is designed as a combination of two small horn antennas connected to the same feed by a passive power splitter. The dual-horn antenna is considered as a pair of half size TE_{10}-mode single-horn antennas. The excitation fields are split by the power splitter and then radiated by two small horn antennas. The aperture field distribution of both small horn antennas are in phase.

The rectangular horn antenna is nearly an ideal antenna for the mm-wave feed in some respects compared to other antennas, due to simplicity of fabrication, wide band impedance match, and uniform distribution of the aperture field.

4.2.2 HFSS Simulation Results

To study the radiation and impedance performance, the UMASS's PAF model was simulated by HFSS (Ansys, Inc.). In the antenna HFSS model, a probe feed is replaced by a waveport feed as the excitation source to the antenna to simplify the HFSS model. To reduce calculation errors and save calculation time, the antenna is modified set as a PEC material. Compared to the L-band, the skin depth at the antenna surface and the conductivity of the conductor decrease at the

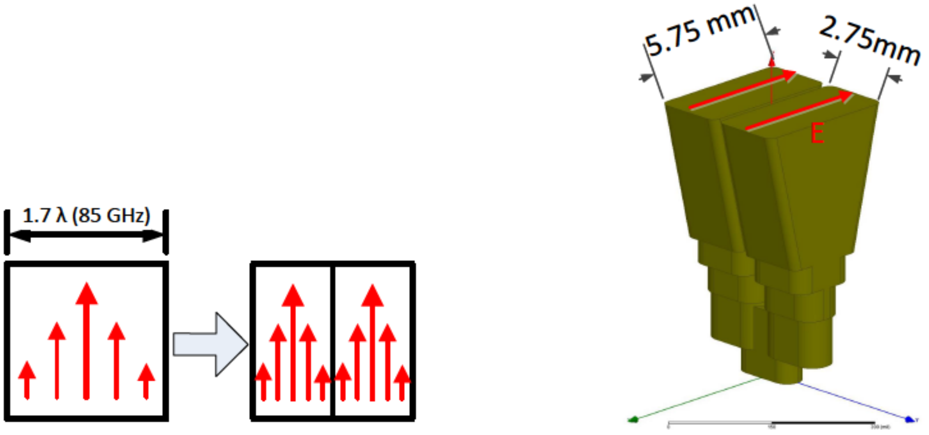

(a) Combination of two horn antennas.

(b) HFSS model for an antenna element.

Figure 4.1: Antenna element for mm-wave PAFs designed by UMass radio astronomy team.

mm-wave band, leading to a large ohmic loss in the antenna and a decrease in radiation efficiency. The surface current on the horn antenna is uniformly distributed, leading to a high radiation efficiency. Since the antennas is cryogenically cooled and the brightness temperature inside the Dewar is about 30 K, the antenna noise temperature can be ignored.

Figure 4.2a shows the simulated S_{11}. The antenna matches a 50 Ω load well within the frequency of interest from 70 GHz to 100 GHz.

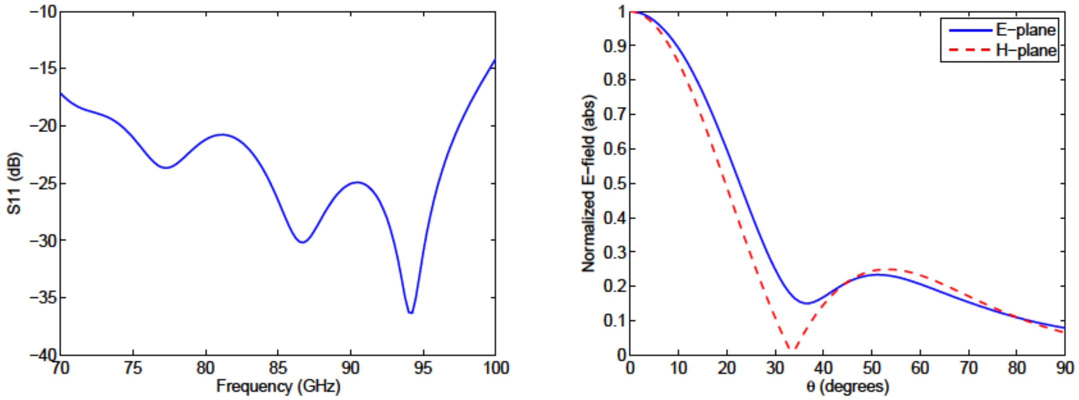

(a) S11.

(b) Radiated fields at 85 GHz.

Figure 4.2: Isolated single mm-wave dual-horn antenna.

Simulated far-field results in E and H planes are shown in Figure 4.2b. The E-fields on the two planes are slightly different. The reason is due to the aperture field distribution of the small horn antenna. The aperture field of TE_{10}-Mode horn antenna is uniformly distributed on the E-plane, but is sinusoidally distributed on the H-plane. Thus, the antenna beamwidth on the E-plane is narrower than that on the H-plane. Sidelobes are observed that is due to large distance between the two small horn antennas.

4.2.3 Analytical Model

Since the mm-wave array element is a combined by a pair of small horn antennas, the radiation pattern for the dual-horn antenna can be considered as that for a single small horn antenna with TE_{10}-Mode times an array factor. This assumption ignores the mutual coupling effect between the two small horn antennas, so that the embedded radiation pattern of the small horn antenna is the same as the radiation pattern of the isolated single small horn antenna.

The radiated fields for a TE_{10}-mode y-polarized horn antenna with an infinite ground plane can be written as

$$E_\theta = -\frac{\pi}{2} C \sin\phi \frac{\cos X}{(X)^2 - (\pi/2)^2} \frac{\sin Y}{Y} \tag{4.1}$$

$$E_\phi = -\frac{\pi}{2} C \cos\theta \cos\phi \frac{\cos X}{(X)^2 - (\pi/2)^2} \frac{\sin Y}{Y} \tag{4.2}$$

where

$$X = \frac{ka}{2} \sin\theta \cos\phi \tag{4.3}$$

$$Y = \frac{kb}{2} \sin\theta \sin\phi \tag{4.4}$$

$$C = j \frac{abkE_0 e^{-jkr}}{2\pi r} \tag{4.5}$$

a and b are the length and width of an aperture antenna respectively. E_0 is a constant for aperture field.

The array factor can be considered as the radiation pattern of two point sources, where the distance between which is equal to the length of a small horn antenna. The array factor is

$$A = \frac{1}{2}(e^{jkd\sin\theta/2} + e^{-jkd\sin\theta/2}) \tag{4.6}$$

Since equation (4.6) represents two point sources located along the z direction, the calculated pattern of the array factor should be rotated to the y direction.

The motivation of the array analytical model is to simplify the analysis of the system model. For instance, an 8×8 array antenna HFSS model takes about 24 hours to do the simulation and take up a large amount of computer memory, but only several minutes for the analytical model. At the same time, the analytical model is flexible and it is simple to change the parameters in the array model. Therefore, it is helpful to roughly analyze the PAF performance using an analytical model. For a single dual-horn antenna, the analytical radiation patterns are compared to the HFSS simulation results in Figure 4.3. The results are close in value.

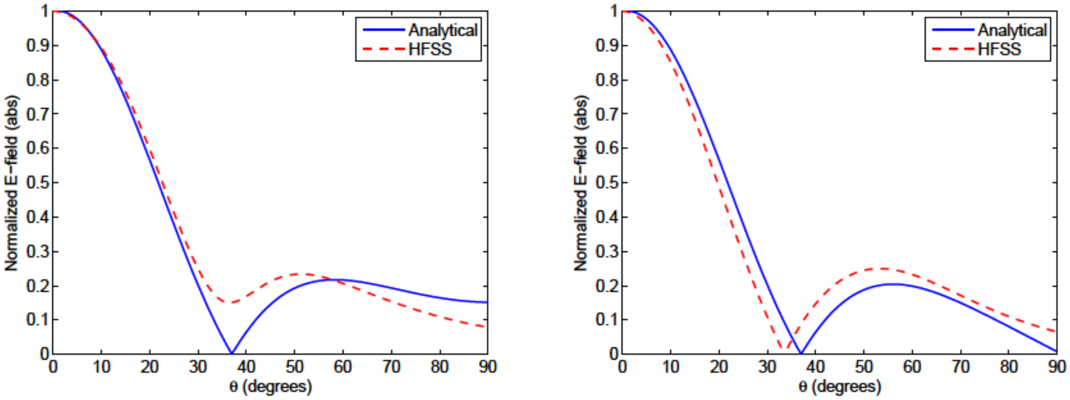

(a) E-plane.

(b) H-plane.

Figure 4.3: Comparison of analytical and full-wave modeled radiation patterns for an isolated single horn antenna.

4.3 Simulated Embedded Element Radiation Patterns

An 8×8 mm-wave array antenna HFSS model is shown in Figure 4.4. To fully utilize the array aperture area and reduce the grating lobes level, each antenna element is separated by a thin wall.

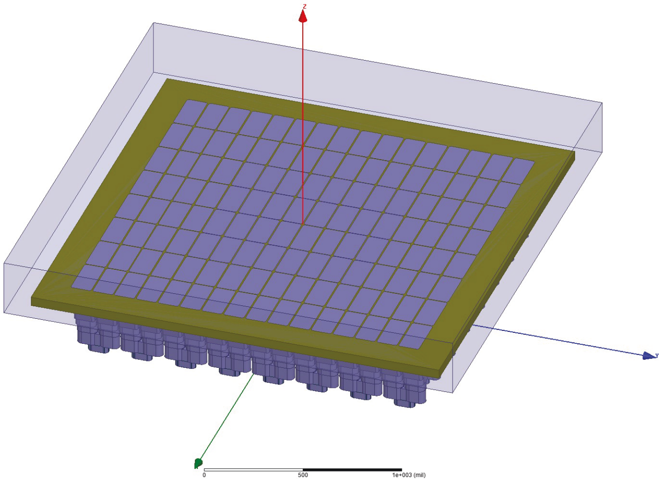

Figure 4.4: HFSS model for an 8×8 array antenna.

Since the length of the array antenna is larger than 15λ, the array HFSS model need to be optimized to achieve both high accuracy and minimum simulation time. The antenna body is built in an PEC background environment. With these settings, the radiation boundary condition needs to cover the top space of the ground plane. Since the antenna body is not included inside the radiation boundary, the simulation time and solution accuracy can be greatly improved. A large radiation box helps to improve the simulation accuracy, but it leads to a long calculation time and large computer memory utilization. The size of the radiation box was optimized and a trade off was made between solution accuracy and the simulation time.

After using these methods to improve the HFSS model, Figure 4.5 compares the simulated far-field pattern of the embedded center element for an 8×8 array using the full-wave method to the experimental measured results by UMass at the frequencies of interest. The simulation results are close to the test results on both the main lobe and the near side lobes.

The only large difference occurs at angles close to the horizontal plane ($\theta = 90°$). In practical applications, the radiation pattern in the horizontal plane is sensitive to the size of the

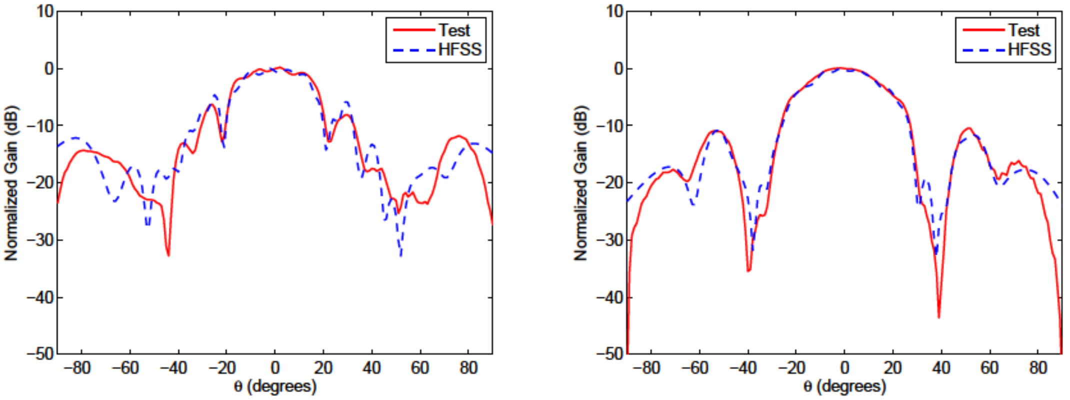

(a) 70 GHz.

(b) 80 GHz.

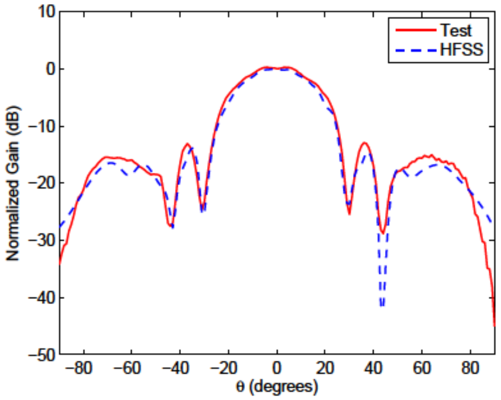

(c) 90 GHz.

Figure 4.5: For an 8×8 array feed, a comparison of radiation pattern for the embedded center element in the E-plane is made between the test results and the HFSS simulation results. (Test results courtesy of the UMass Radio Astronomy Research Group).

ground plane and the objects around the array feed. Based on this fact, it is necessary to study how much power is radiated near the horizontal plane compared to the total radiated power. $\eta_{\theta_\circ}$ is defined as a power ratio of the radiated power within an opening angle ($\theta_\circ$) to the total radiated power

$$\eta_{\theta_\circ} = \frac{\int_0^{2\pi}\int_{\theta_\circ}^{\pi} \mathrm{F}(\theta,\phi)\mathrm{r}^2 \sin\theta \,\mathrm{d}\theta\mathrm{d}\phi}{4\pi} \tag{4.7}$$

where $\mathrm{F}(\theta,\phi)$ represents the normalized radiation pattern.

Based on this formula, using the simulated fields from the simulated results, the power ratio over different opening angles is calculated for the embedded center element at 80 GHz in

Figure 4.6. From this plot, we can conclude that the power ratio near the antenna horizontal plane is less than 1%. Although there is a large difference for the radiation pattern on the horizontal plane between the test and simulation results, the influence to the system performance can be ignored.

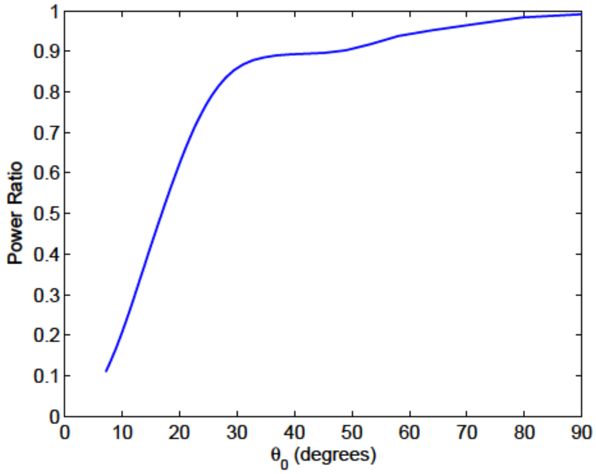

Figure 4.6: From the embedded radiation pattern of the center element in an 8×8 array feed, the power ratio defined in Equation 4.7 is calculated with different open angles θ_0.

4.4 Thermal Dewar Window Size Study

The system noise temperature for a PAF system depends on the LNAs noise temperature, which can be largely reduced by cryogenically cooling the electronics. A cryogenic system for the array antenna and LNAs were built by UMass to reduce the antenna ohmic loss and LNA electronic noise.

To study the phased array feed influenced by the cryogenic Dewar, a model for an array antenna associated with a Dewar box is shown in Figure 4.7. The array antenna located in a Dewar box blocks the transmission of the EM wave, so an open window on the Dewar is build on top of the array antenna to allow radiation form the feed to pass through the Dewar.

The Dewar window is covered by an air material to keep vacuum inside the Dewar and make the window transparent to the EM wave. To avoid multiple reflections between the Dewar wall and the array antenna, an absorber material is used on the surface of the Dewar wall. In terms of the noise radiation characteristic, the absorber material can be considered as an ideal black

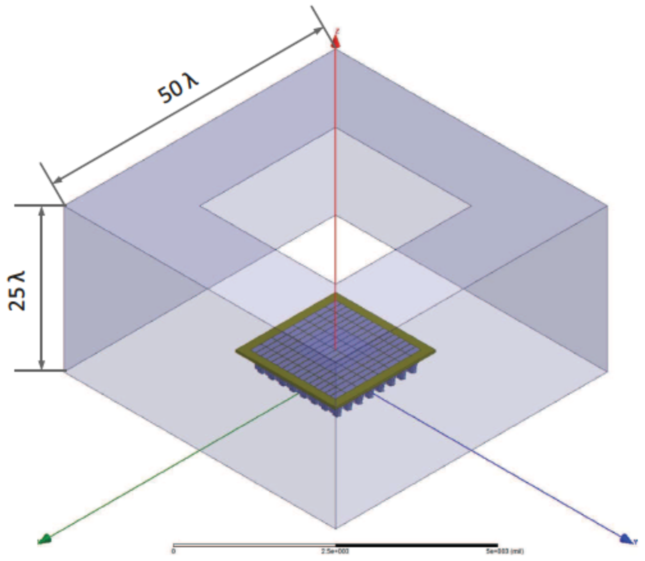

Figure 4.7: 8×8 array antenna with a Dewar window model.

body and its equivalent noise temperature is equal to the physical temperature. The brightness temperature inside the Dewar is about 30 K. Compared to the sky (55−300 K) and ground noise temperature (300 K), the system noise temperature contributed by the warm Dewar wall can be ignored.

As shown in Figure 4.3, the antenna element has a broad beamwidth, so that the sidelobes of the antenna radiation pattern will be blocked by the Dewar wall. In terms of the radiation performance of the array antenna, the Dewar window should be large enough to minimize the blockage of the EM wave radiation. But it will reduce the mechanical strength of the Dewar and air material. Hence, the size of the Dewar window need to be studied to make a trade-off between these two requirements.

4.4.1 Hybrid Method

A full-wave model is used to study the radiation performance of an 8×8 array antenna with Dewar influenced by the thermal Dewar window. The array antenna model can be easily solved by finite element method (FEM), but the Dewar window that is a large electrical structure is too hard to be analyzed using the same method. Based on this fact, physical optics (PO) method is used to overcome this problem.

For the optimization of Dewar window size, HFSS 15 is used to solve this hybrid solution problem. Since the FEM model cannot automatically export the radiated fields from the array model to the window model to calculate the secondary radiated fields using the PO method, a Visual Basic Scripting Edition (VBScript) is used to automatically call HFSS to do the FEM-PO hybrid simulation for antenna element. The steps of the simulation process operated by the VBScript are illustrated in the Figure 4.8.

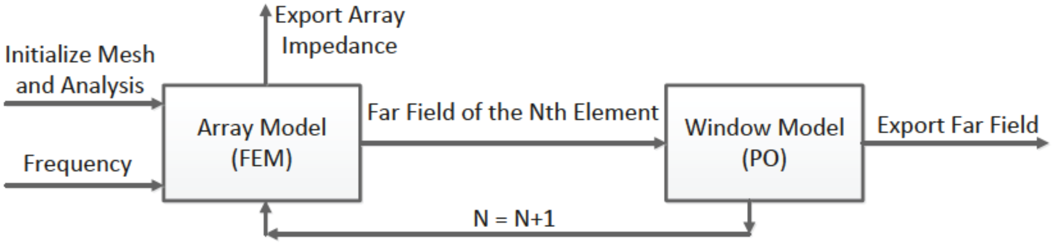

Figure 4.8: Steps of HFSS simulation process called by VBScript.

4.4.2 HFSS Simulation Results and Analysis

By using the hybrid method, Figure 4.9 shows the magnitude of the surface current distributions on the Dewar window for the excitation of corner element, center element and edge elements respectively. It is clear to see that the induced current distributions on the Dewar window are consistent with the position of the excited element.

When the array corner element is excited, the surface current behaves as a ring shape, which is circularly symmetric along the corner element. However, the magnitude of the surface current is not uniformly distributed along each current ring. The current on the top part of Dewar window is much larger than that on the left part. This is because the horn antenna is a single-pol antenna and the boundary condition of PEC limits the diffraction of the tangential electric field. This effect can be seen in Figure 4.10, which shows the surface current vector distribution on the window. The direction of the surface current is the same as the direction of the antenna polarization. On the top part of Dewar window, the E-field radiated by the antenna is perpendicular to the edge of the window, which could be easily diffracted from the edge of the window. On the left side of the

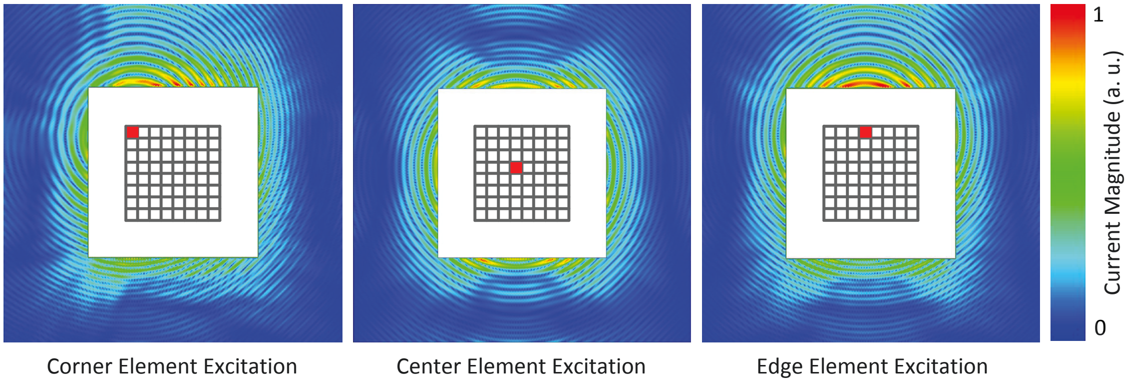

Figure 4.9: Surface current distributions on the Dewar window of three different element excitation (top view).

Dewar window, however, due to the boundary condition limiting the tangential field propagation on the PEC surface, there is little E-field diffracted from the edge of window. Based on this effect, stronger surface currents are induced on the top part of the window than that on the left part of the window.

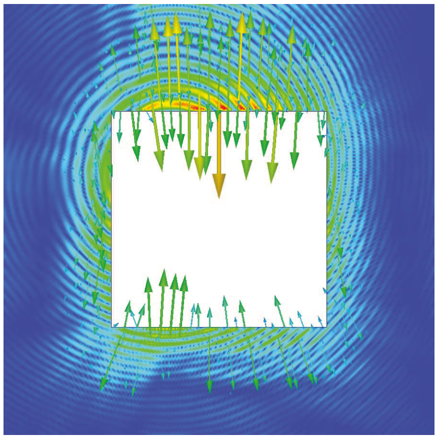

Figure 4.10: Surface vector current distribution on the Dewar window for the corner element of an 8×8 array.

Figure 4.11 shows comparisons of the radiation pattern in the E-plane and H-plane for different antenna element excitations with and without a blockage from a 3 inch Dewar window. It can be seen that the main lobe radiation pattern for the bare array is almost the same as that for the array with a window. But the side lobe comparison shows a large difference, which can be contributed to the blockage of Dewar walls. Meanwhile, the radiation pattern is different among the excited elements, and this difference mainly depends on the distance between the antenna element and the Dewar window edges.

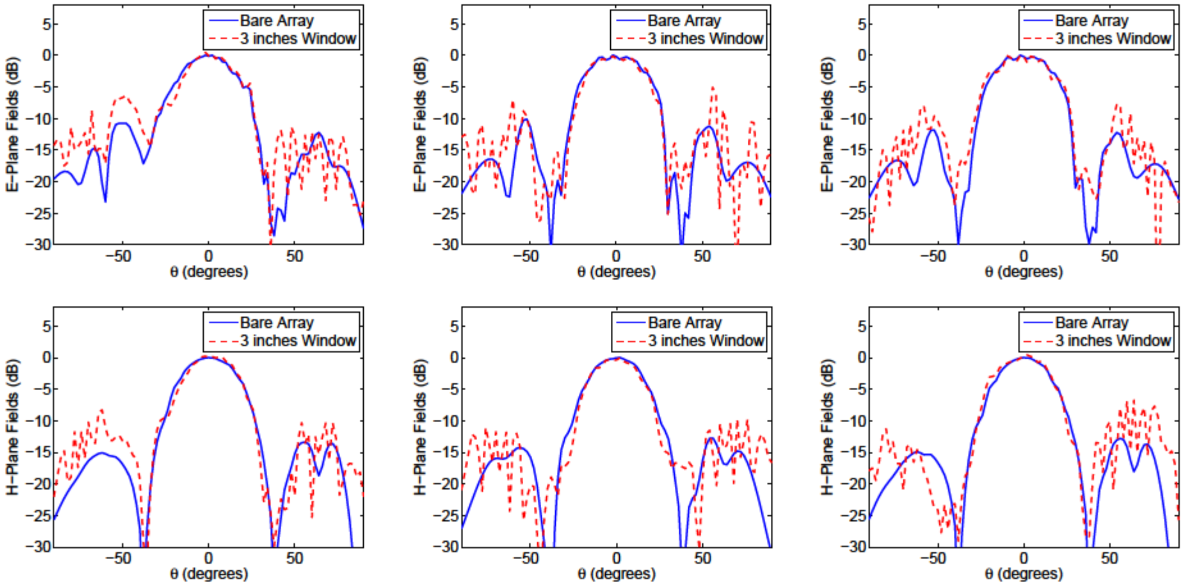

(a) Corner Element (b) Center Element (c) Edge Element

Figure 4.11: A comparison of E-plane and H-plane patterns between an 8×8 bare array and the array with a 3 inches window with different antenna element excitation.

Figure 4.12 shows the embedded radiated field comparison for the center element of an 8×8 array with different Dewar window sizes. As the Dewar window length is increased from 2 inches to 4 inches, there is less difference in the main lobe and side lobes between the bare array and the array with a window. The same phenomenon is observed at the three different frequencies of interest.

4.4.3 PAF Noise Model with Dewar Window

The GBT is an Gregorian parabolic off-axis reflector antenna. The secondary and primary reflector antenna can be approximately modeled as a single parabolic on-axis reflector antenna with a focal length to diameter ratio f/D chosen such that the opening angle is equivalent to that of the GBT secondary reflector. The aperture blockage by PAF system and the reflector edge

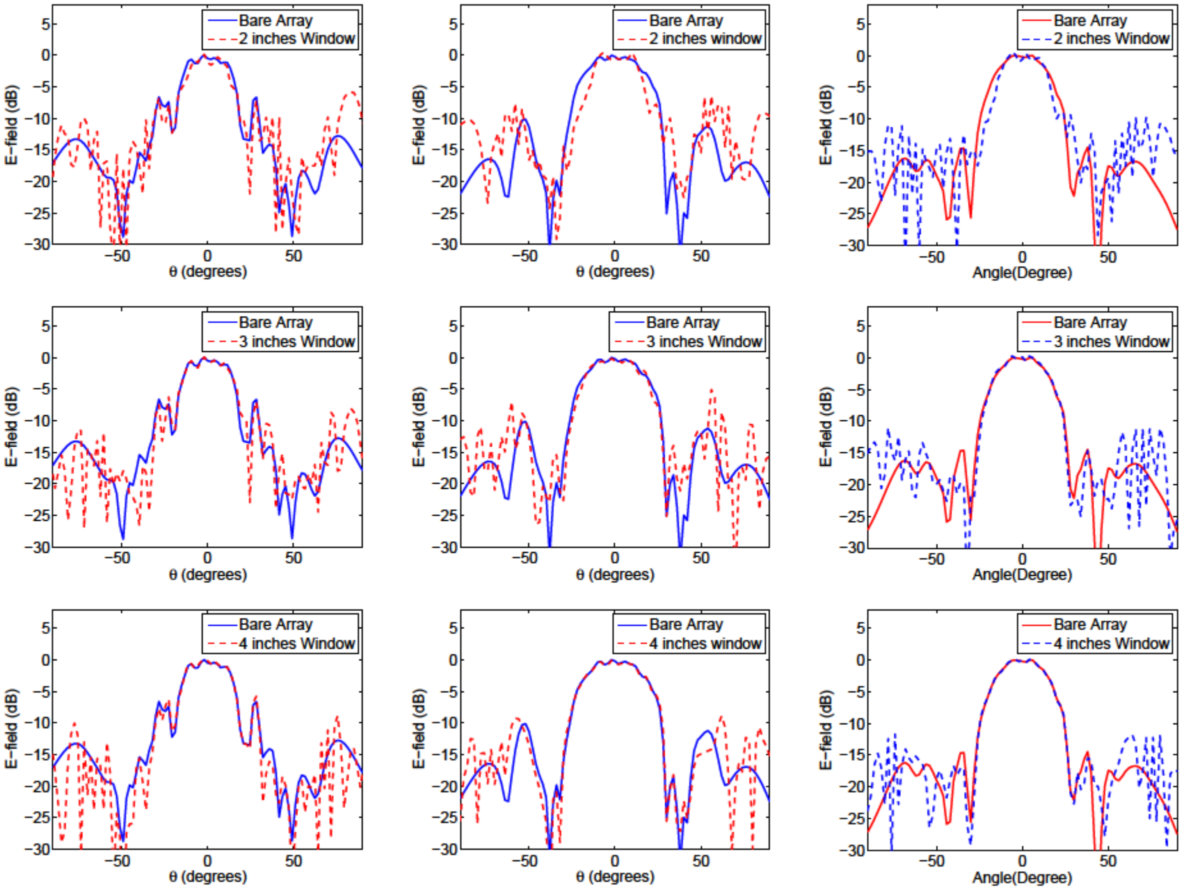

(a) 70 GHz. (b) 80 GHz. (c) 90 GHz.

Figure 4.12: Comparisons of normalized E-field on the E-plane of the center element in an 8×8 bare array antenna and the array antenna with different window sizes.

diffraction are ignored in the reflector optical model. Since illumination efficiency and spillover are essentially independent of reflector size for a fixed f/D, the equivalent reflector diameter is chosen to be 1 meter to reduce the computational cost of the model. The reflector model and PAF structure are depicted in Figure 4.13. The modeled noise sources are as follows:

1) *Sky noise:* Atmospheric and cosmic background noise is received by the formed main beam of the feed and reflector system. The equivalent brightness noise temperature of the sky at zenith is approximately equal to 55 K at the frequencies of interest.

2) *Spillover noise:* Beyond the main beam, received noise include a non-uniform warm sky noise increasing to ambient temperature (290 K) as the arrival angle relative to the receiver boresight approaches the horizon.

3) *Receiver noise:* The electronic noise of receivers is dominated by LNAs noise in the cryogenic font end. Noise due to losses in the antenna is ignored.

The Dewar walls are covered by absorber materials to avoid multiple reflectors between array antennas and Dewar walls. Because the brightness noise temperature of Dewar walls is smaller than the sky and ground noise temperature, to simplify the noise model, the noise fields received by array antennas from the Dewar walls are ignored.

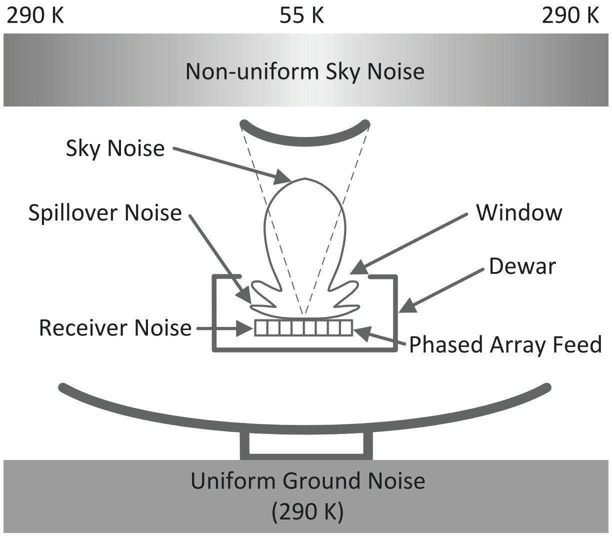

Figure 4.13: Noise sources that contribute to the system noise budget include sky noise from warm sky, spillover noise from the non-uniform war sky and ground, and receiver noise from system electronics. The off-axis GBT reflector and secondary reflector are modeled approximately as a single parabolic on-axis symmetric reflector with $f/$D equivalent to the GBT secondary.

4.4.4 System Performance with Different Dewar Window Size

The radiated fields influenced by the Dewar window size has been studied in the previous section. In this section, system performance of an 8×8 array feed for different frequencies, reflector f/D, and window sizes is studied based on the above noise model. The equivalent reflector f/D for GBT can be changed by adjusting the apparent opening angle of the optics using a set of lenses.

Figure 4.14 shows the aperture efficiency η_{ap}, system noise temperature T_{sys} and sensitivity for the boresight formed beam. The Dewar window changes the system noise temperature, but has little influence on the aperture efficiency. The reason is because aperture efficiency mainly depends on the main lobe radiation pattern illuminating the reflector antenna. Since the Dewar window has a large influence on the side lobe power but only causes a small change to the main lobe radiation pattern, the aperture efficiency of the array feed with Dewar window is close to that of the bare array feed.

The system noise temperature includes sky brightness noise, spillover noise and electronic noise of LNAs. The electronics noise mainly depends on the impedance match between the antenna and the LNAs. Since the element spacing in the frequency range is larger than 1.4 λ, the mutual coupling effects among the array elements can be ignored. The active impedance of the array element is stable over the beamforming coefficients, leading to a constant electronic noise. The variation of the system noise temperature over different window sizes is due to the variation of the sky and spillover noise temperatures. An obvious diffraction effect is observed when the Dewar window size becomes small, which leads to a large spillover of radiation pattern to the warmer sky. Hence, the system noise temperature increases with decreasing Dewar window size.

Using the same method, the system figures of merit are studied in Figure 4.15 for the case of a steered formed beam on the boundary of the field of view. Compared to the boresight formed beam, both the aperture efficiency and the system noise temperature become worse for the steered beam. When the beam is steered away from the boresight direction, there will be more blockage of the Dewar window, leading to a larger change in the radiation pattern.

Field of view (FoV) of the PAF with different f/D is shown in Figure 4.16. There is no significant change in FoV for different Dewar window sizes. The reason is because for a given f/D, FoV mainly depends on the number and spacing of array elements. Meanwhile, it can be seen that FoV is inversely proportional to f/D, which is independent of Dewar window size and frequency.

4.5 Offset Array Feed Analysis

The installation position of the mm-wave feed is limited by the available mounting port in the GBT feed cabin. The phase center for the installed PAF will be offset slightly from the focal

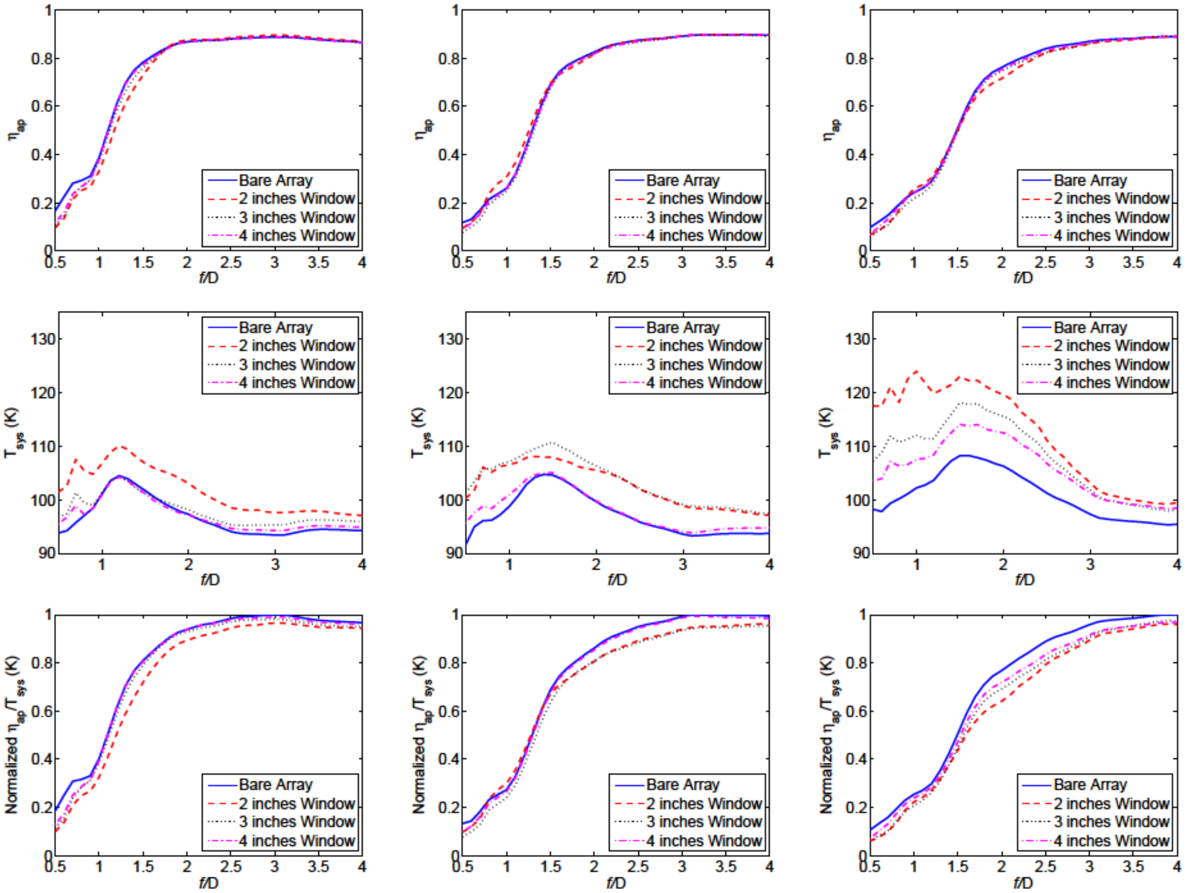

(a) 70 GHz. (b) 80 GHz. (c) 90 GHz.

Figure 4.14: Comparisons of aperture efficiency η_{ap}, system noise temperature T_{sys} and normalized sensitivity $\eta_{\text{ap}}/T_{\text{sys}}$ for an 8×8 array feed with different window sizes at different frequencies for the boresight formed beam.

point of the reflector. We have conducted simulation work based on the noise model in section 4.4.3 to determine the effect of the offset on system performance.

The physical optics (PO) method is used to calculate the far-field pattern of the reflector antenna with different offset distances from the focal point in the lateral and axial directions at 80 GHz. Sensitivity distribution for the lateral and axial shift over the steered angle are shown in Figure 4.17. Under the same offset distance, the lateral shift shows more influence to the PAF sensitivity than the axial shift. The peak sensitivity over the feed field of view is shown in Figure 4.18. The 8×8 feed antenna can be offset in the x and z direction up to ∼22 cm and ∼3 cm respectively, with less than 0.1 dB sensitivity reduction, and the field of view is not sensitive to the changing of the offset distance.

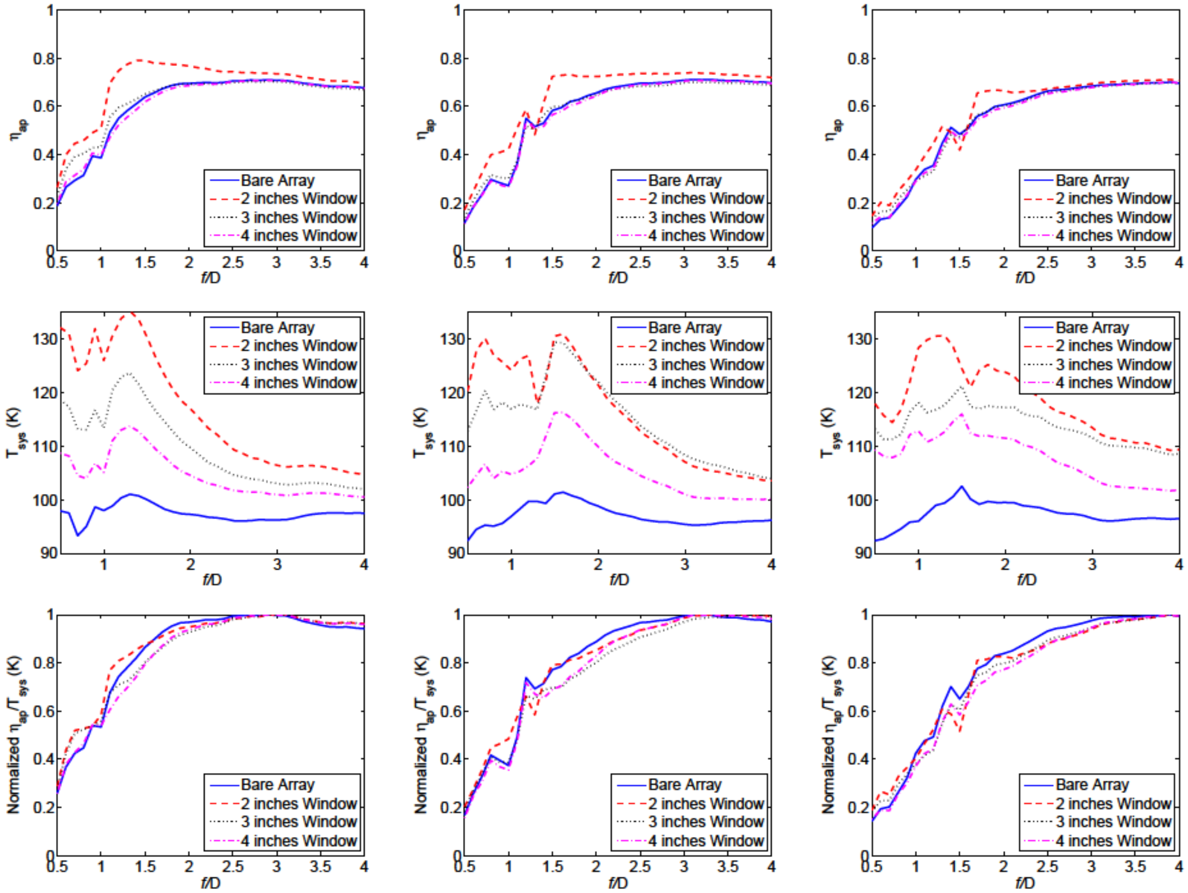

(a) 70 GHz. (b) 80 GHz. (c) 90 GHz.

Figure 4.15: Comparisons of aperture efficiency, system noise temperature and normalized sensitivity for an 8×8 array feed with different window sizes at different frequencies when the formed beam is steered to the boundary of the effective field of view.

4.6 Required Number of Elements per Beam for the mm-wave PAF

Beamformer has been widely used for signal processing technique. In a narrow bandwidth, the beamformer can change the radiation pattern of an array antenna by combining the array elements with specified phase and amplitude. In terms of its application to radio astronomy, beamforming improves the illumination pattern of an array feed by increasing aperture efficiency and spillover efficiency, which leads to relatively stable radiation pattern for the steered beam, achieving a wider uniform field of view compared to the conventional cluster horn feeds.

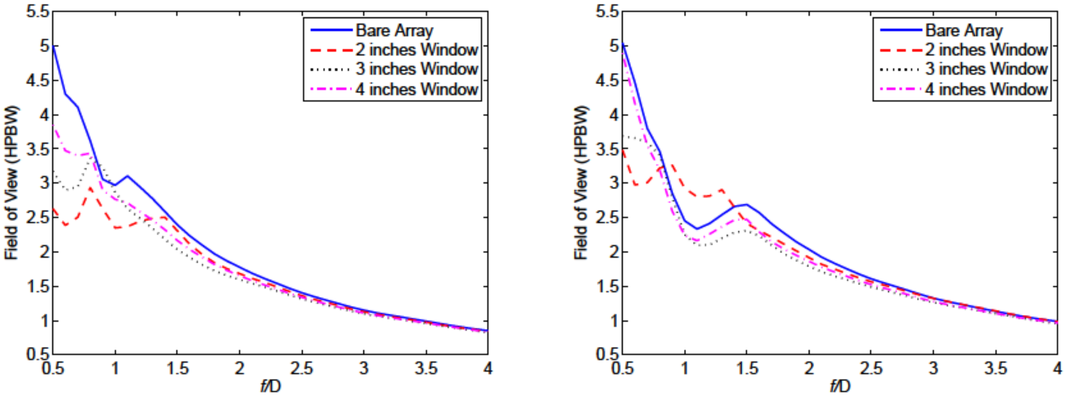

(a) 70 GHz.

(b) 80 GHz.

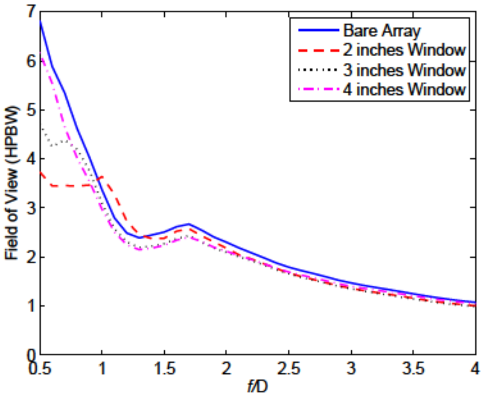

(c) 90 GHz.

Figure 4.16: Comparisons of effective field of view for different window sizes and f/D for an 8×8 array feed at three different frequencies.

In digital beamforming, the operation of amplitude scaling and phase shifting of the antenna elements and the summation of receiving signal are done digitally. Since each PAF element channel needs to be digitized, a large amount of hardware is required.

The beamformer weights of array feed elements reflect to the first order of the Airy pattern of the focal plane fields for high beamformed aperture efficiency. When the incident wave arrives from the reflector boresight direction, the center array element matches the main lobe of the Airy pattern, and the other array elements around the center element match the sidelobes of the Airy pattern. Since the sidelobe level is relative low compared to the main lobe level, the values of element weights used to match the sidelobes are relatively small compared to the peak of the Airy pattern.

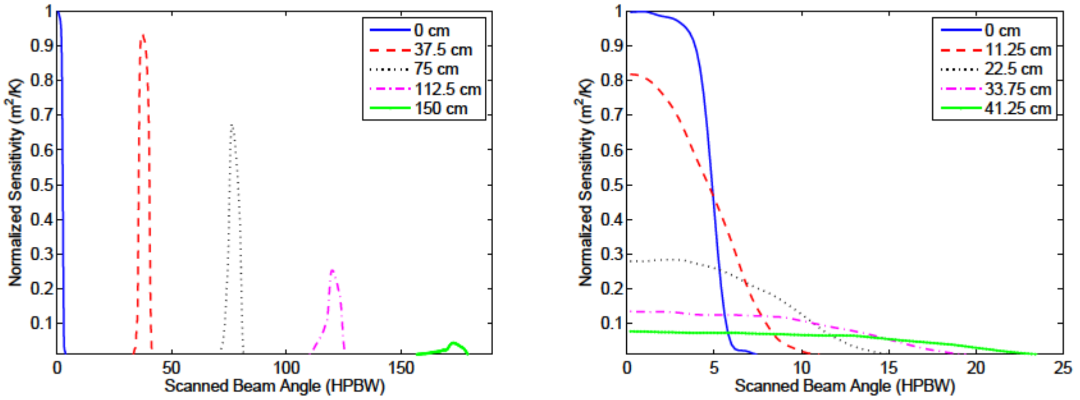

(a) Lateral shift. (b) Axial shift.

Figure 4.17: Normalized sensitivity distribution with different steered angles for an 8×8 offset array feed at different lateral (x/y) and axial offset (z) distances.

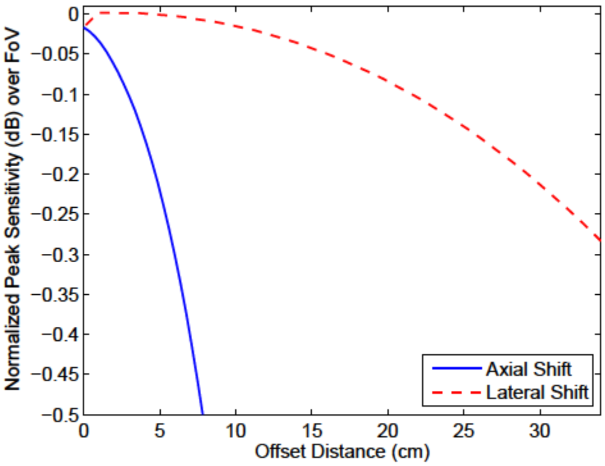

Figure 4.18: Peak sensitivity (dB) over field of view as a function of lateral and axial offset distances.

In view of the wide amplitude variation of beamformer weights, a threshold could be used to eliminate elements with small weights to reduce the computational load of real time beamforming. If the absolute values of beamformer weights are larger than the threshold, those elements would be used for the beamforming. If the absolute value of beamformer weights is less than the threshold, the weights of these elements are set to zero, which means these elements will not be used in the beamformer.

The maximum-sensitivity beamformer weights before using the threshold can be calculated by

$$\mathbf{w} = \mathbf{R}_{\text{noise}}^{-1}\mathbf{V}_{\text{sig}}(\Omega_{\text{s}}) \tag{4.8}$$

where $\mathbf{R}_{\text{noise}}$ is the correlation matrix corresponding to the system noise and $\mathbf{V}_{\text{sig}}(\Omega_{\text{s}})$ is the received signal resulting from a plane wave arriving at an angle Ω_{s}. When applying a threshold to the beamformer weights, the weights become

$$\mathbf{w}'(n) = \begin{cases} 0 & \text{if } |\mathbf{w}(n)| \leq \tau \\ \mathbf{w}(n) & \text{if } |\mathbf{w}(n)| > \tau \end{cases} \tag{4.9}$$

where τ is the beamformer weights threshold value. $\mathbf{V}_{\text{sig}}$, $\mathbf{R}_{\text{noise}}$, $\mathbf{R}_{\text{iso}}$ and $\mathbf{R}_{\text{t}}$ are reduced in size including the remaining nonzero elements used for beamforming and then become $\hat{\mathbf{V}}_{\text{sig}}$, $\hat{\mathbf{R}}_{\text{noise}}$, $\hat{\mathbf{R}}_{\text{iso}}$ and $\hat{\mathbf{R}}_{\text{t}}$, respectively.

Resulting from the received signal power response when an incident plane wave with an angle, the correlation matrix $\mathbf{R}_{\text{sig}}$ becomes

$$\hat{\mathbf{R}}_{\text{sig}} = S_{\text{sig}}\hat{\mathbf{V}}_{\text{sig}}\hat{\mathbf{V}}_{\text{sig}}^{H} \tag{4.10}$$

where S_{sig} is the signal power density in one polarization. The antenna polarization direction assumes match to the incident signal. The squeezed beamformer weights $\hat{\mathbf{w}}$ resulting from the squeezed correlation matrix becomes

$$\hat{\mathbf{w}} = \hat{\mathbf{R}}_{\text{noise}}^{-1}\hat{\mathbf{V}}_{\text{sig}}(\Omega_{\text{s}}) \tag{4.11}$$

After squeezing the correlation matrix, the aperture efficiency η_{ap} can be calculated by

$$\eta_{\text{ap}} = \left(\frac{k_{\text{b}}T_{\text{iso}}B}{S_{\text{sig}}A_{\text{phy}}}\right)\left(\frac{\hat{\mathbf{w}}^{H}\hat{\mathbf{R}}_{\text{sig}}\hat{\mathbf{w}}}{\hat{\mathbf{w}}^{H}\hat{\mathbf{R}}_{\text{iso}}\hat{\mathbf{w}}}\right) \tag{4.12}$$

where k_b is Boltzmann's constant, T_{iso} is the noise temperature for the isotropic noise response, B is the bandwidth of receiving signal, and A_{phy} is the physical area of the reflector. The system noise temperature T_{sys} is given by

$$T_{\text{sys}} = T_{\text{iso}} \frac{\hat{\mathbf{w}}^H \hat{\mathbf{R}}_{\text{noise}} \hat{\mathbf{w}}}{\hat{\mathbf{w}}^H \hat{\mathbf{R}}_{\text{t}} \hat{\mathbf{w}}} \tag{4.13}$$

Finally, the sensitivity S can be calculated by

$$S = \frac{\eta_{\text{ap}} \eta_{\text{rad}} A_{\text{phy}}}{T_{\text{sys}}} \tag{4.14}$$

where η_{rad} is radiation efficiency of the antennas, and is approximated to unity because the antenna is plated with copper and can be considered as PEC.

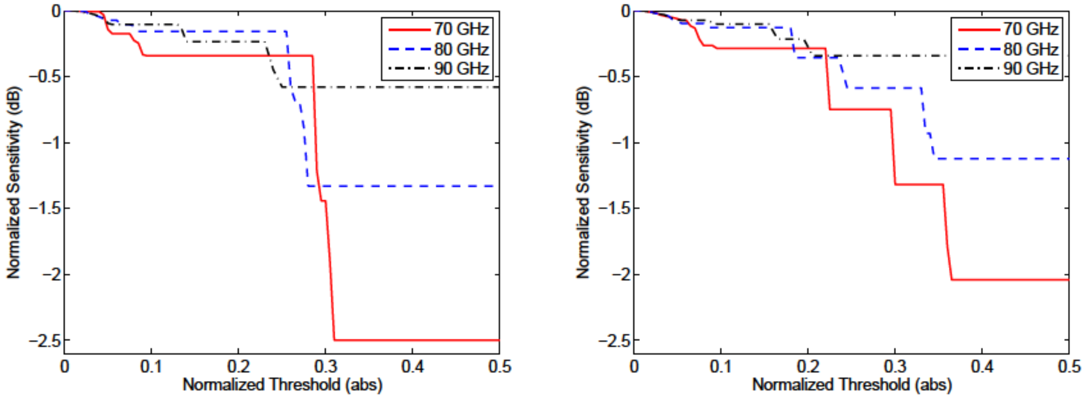

(a) Boresight direction.

(b) Boundary of field of view.

Figure 4.19: Influence of beamformer weight threshold for an 8×8 array on sensitivity at the boresight direction and at the boundary of the field of view.

For an 8×8 mm-wave array feed, the influence of the beamformer weights threshold on sensitivity is shown in Figure 4.19. Performance is more sensitive to the threshold at low frequencies than that at high frequencies. The reason is because when the frequency is decreased, the size of Airy pattern becomes larger, which means more elements are needed for each beam. This explanation can be proved by Figure 4.20, which depicts the beamformer weights distribution for an 8×8 array when the formed beam is at the direction of boresight and the boundary of field of view, respectively.

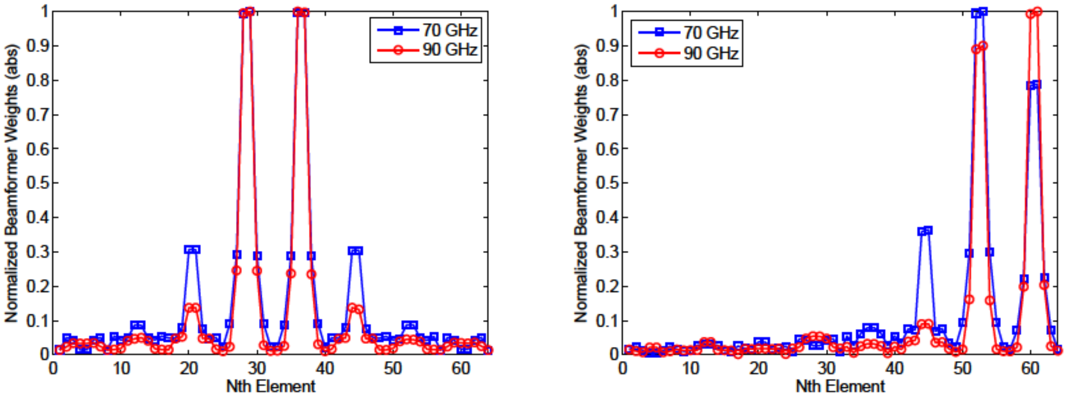

(a) Boresight direction.

(b) Boundary of field of view.

Figure 4.20: Beamformer weights for an 8×8 array without using beamformer weights threshold.

The number of non-zero beamformer weights is shown in Figure 4.21. From this plot we can get the conclusion that in the worst case, beamforming with 28 of 64 elements causes a drop of 0.1 dB in sensitivity, and in the best case, only 8 elements are needed per pixel, leading to a considerable savings of computational resources.

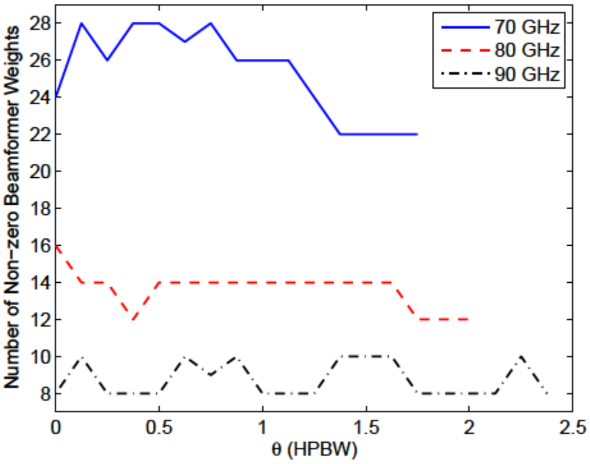

Figure 4.21: Number of non-zero beamformer weights for an 8×8 array when the beam is steered over the field of view with threshold selected for a maximum 0.1 dB sensitivity reduction.

4.7 Performance Analysis of the mm-wave PAF

The array element of the UMass PAF is designed as a combination of two small horn antennas, which can be considered as a pair of half size TE_{01}-model single-horn antennas. To prove the antenna structure to be an optimized design, the performance of an analytical 8×8 dual-horn array feed is compared to a single full size TE_{10}-mode array feed over the operation frequency. The survey efficiency for the dual-horn array feed is analyzed over different reflector f/D.

4.7.1 Comparison of Full-Wave and Analytical Feed Model

Compared to the full-wave model, the analytical feed model shows advantage of speed up of the analysis of phased array feed. This model neglects the surface waves, edge element effects, and details of the response of the waveguide feeds. To assess these higher-order aspects of the feed, we also modeled the feed with a full-wave modeling tool.

In order to verify the models, we compare the aperture efficiency within the frequencies of interest obtained with the analytical model. Figure 4.22 shows that the bulk aperture efficiency with the analytical model is close to that obtained with the full-wave simulation results in overall level but does not include details associated with higher-order mode formation and other fine-scale frequency-dependent effects with the feed horns.

Figure 4.23 shows a comparison of the feed sensitivity map at 80 GHz using FEM and analytical models. Due to the array edge effect that degrades the radiation pattern of the edge elements, the sensitivity for the full-wave model drops faster for steered beams than the predicted results from the analytical model, leading to a smaller field of view.

4.7.2 Comparison of Dual-Horn and Single-Horn PAF using Analytical Model

The radiation characteristics of the single and dual-horn arrays can be compared using the reflector aperture efficiency. The max-gain beamformer for a beam steered to the reflector boresight direction is applied over the band 25-100 GHz. The max-gain beamformer is used here instead of the max-sensitivity beamformer to emphasize the illumination pattern quality in the comparison.

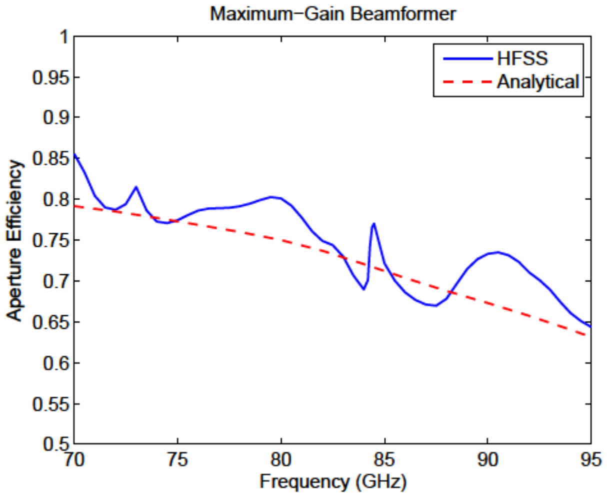

Figure 4.22: Comparison of aperture efficiency of an 8×8 mm-wave array feed with full-wave and analytical models.

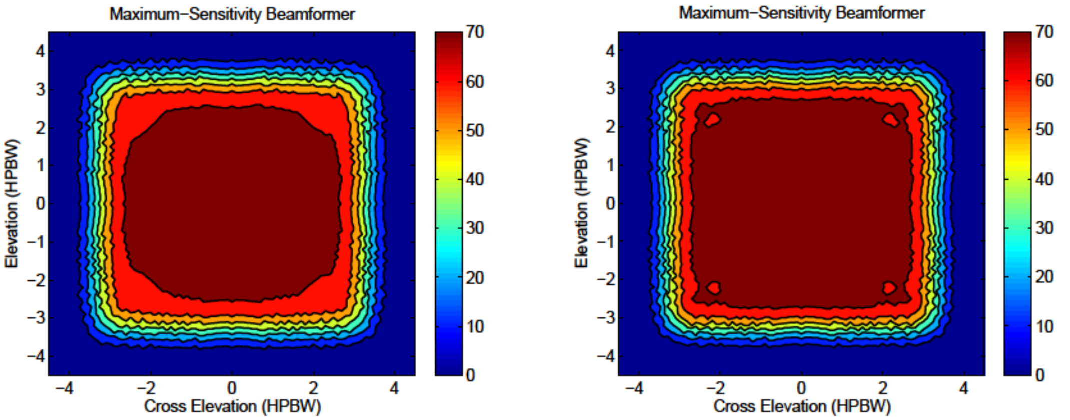

(a) FEM model.

(b) Analytical model.

Figure 4.23: Comparison of sensitivity map at 80 GHz using full-wave and analytical array feed models.

To further understand the performance of the mm-wave array feed, the aperture efficiency η_{ap} achieved by the feed can be factored as

$$\eta_{\mathrm{ap}} = \eta_{\mathrm{sp}}\eta_{\mathrm{t}}\eta_{\mathrm{p}}\eta_{\mathrm{x}}\eta_{\mathrm{r}} \tag{4.15}$$

where η_{sp} is spillover efficiency, η_{t} is taper efficiency which describes the uniformity of the amplitude distribution of the feed radiation pattern over the surface of the reflector, η_{p} is the phase

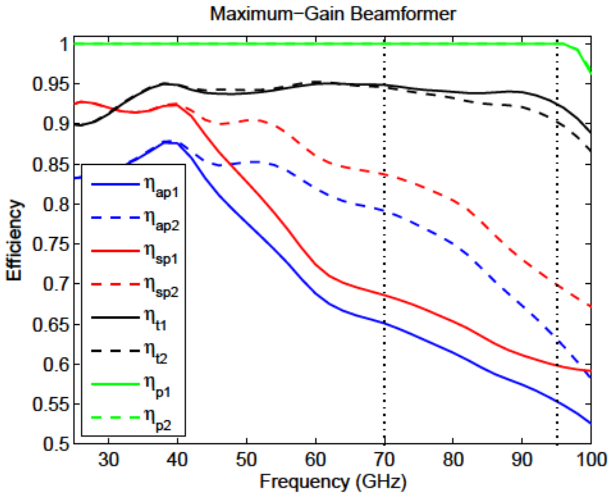

Figure 4.24: Aperture, spillover, taper and phase efficiency of an 8×8 array feed with reflector f/D = 1.9 using a simple analyticial model for the element radiation patterns. The max-gain beamformer is used to form a boresight beam. Subscripts 1 and 2 represent the single-horn array and dual-horn array, respectively. The vertical lines bracket the designed operating bandwidth of the feed.

uniformity of the field over the aperture plane, η_x is the polarization uniformity of the field over the aperture plane, η_b is the blockage efficiency, and η_r is random reflector surface error efficiency. Among these efficiencies, η_x, η_b and η_r are ignored in the reflector model to simplify the analysis.

Results comparing the various efficiencies are shown in Figure 4.24. Over the band of interest, the dual-horn antenna element achieves larger aperture efficiency than that of the single-horn antenna. This is due to the more uniform aperture field distribution of the dual-horn antenna. The single-horn element exhibits a wider radiation pattern and higher spillover loss. The results verify that the dual-horn array has better radiation performance over the designed operating bandwidth than that of the conventional single-horn antenna.

We now consider the survey efficiency of the feed, in order to analyze the overall system performance including spillover and receiver noise. The noise model in Section 4.4.3 is simplified to satisfy the wideband analysis of the analytical model. The diffraction effect from the Dewar window edge is not considered in the simplified model to save calculation time. The spillover noise is the noise field received by array antennas from the Dewar walls, the noise temperature of which is assumed to 30 K.

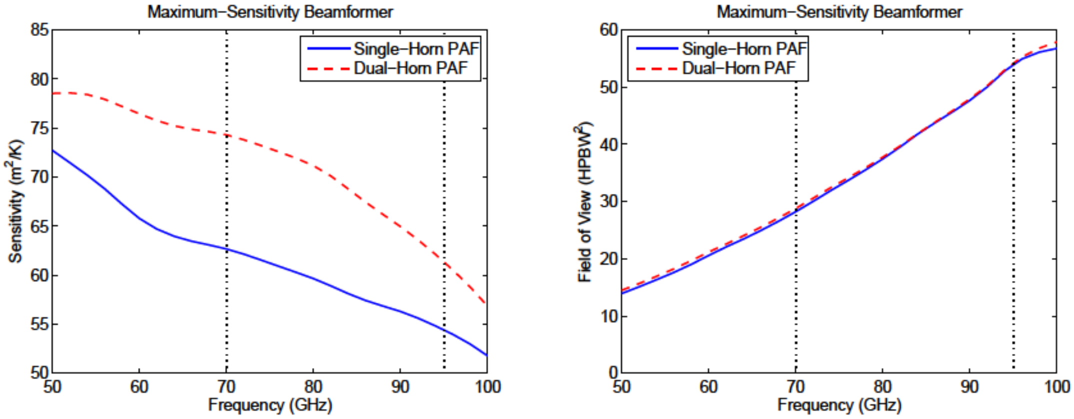

(a) Sensitivity.

(b) Field of view.

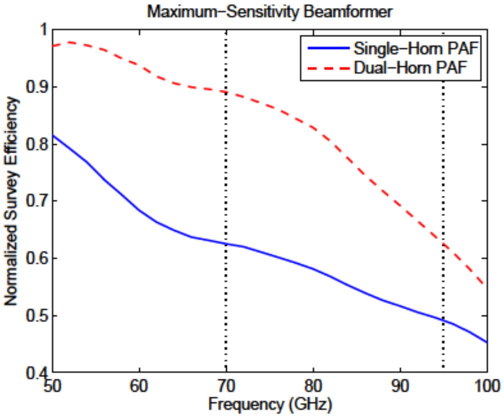

(c) Normalized survey efficiency.

Figure 4.25: Comparisons of sensitivity, field of view and survey efficiency of analytical 8×8 array feeds with reflector $f/\mathrm{D} = 1.9$, using the max-sensitivity beamformer for boresight direction.

Using the simplified model, Figure 4.25a and Figure 4.25b compare the sensitivity and field of view results for the two arrays as a function of frequency. The higher sensitivity is mainly due to the larger spillover efficiency. Field of view depends mainly on the array aperture size, number of elements, and the reflector geometry, and is similar for both arrays. From the survey efficiency results shown in Figure 4.25c, we can conclude that the element size is the optimal design, and the dual-horn antenna array shows better overall system performance than that of the commonly used single-horn antenna over the frequencies of interest.

4.7.3 Survey Efficiency Analysis for Different Reflector f/D using Analytical Model

The equivalent f/D of the GBT secondary reflector is 1.9. The apparent opening angle of the secondary could be changed using a lens to potentially increase the aperture efficiency of the realized illumination patterns formed by the array feed. This would add additional loss and make the system more complex.

Survey efficiency (S.E.) is defined by

$$\text{S.E.} = \int\limits_{\text{FoV}} S^2(\theta,\phi)\,d\Omega. \tag{4.16}$$

Figure 4.26 shows that the normalized survey efficiency performs the highest performance near the equivalent f/D of GBT, so the lens is not needed in the system.

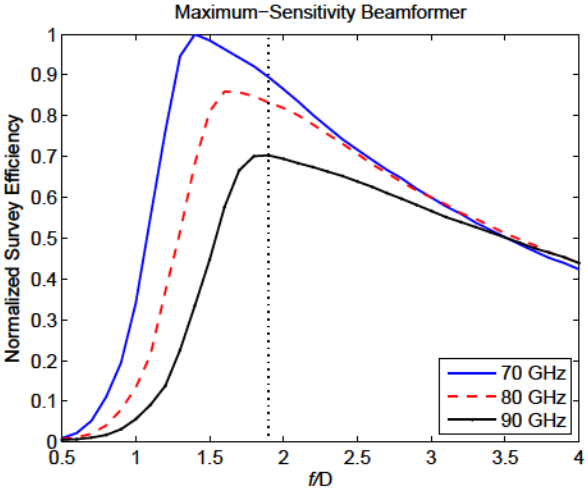

Figure 4.26: Comparison of the normalized survey efficiency of the 8×8 dual-horn PAF as a function of f/D at frequencies of interest. The vertical line marks the equivalent f/D for the GBT secondary reflector.

From the above analysis, we can conclude that the UMass array element antenna is an optimal design compared to a conventional single-horn antenna element and shows best performance combined with the GBT optics.

4.8 Analysis of a Wide Band Uniform Square Array Feeds

In this section, an analytical model of a 6×6 mm horn antenna with uniform aperture field distribution is used to study the aperture efficiency of an N×N array feed over a wide bandwidth. This study helps us to understand the influence of array size on the PAF performance.

In the model, the maximum gain beamformer is used to simply the analysis and focus on the characteristics of the antenna radiation pattern. The *f*/D of the reflector antenna is 1.9. The array element spacing is equal to the element length.

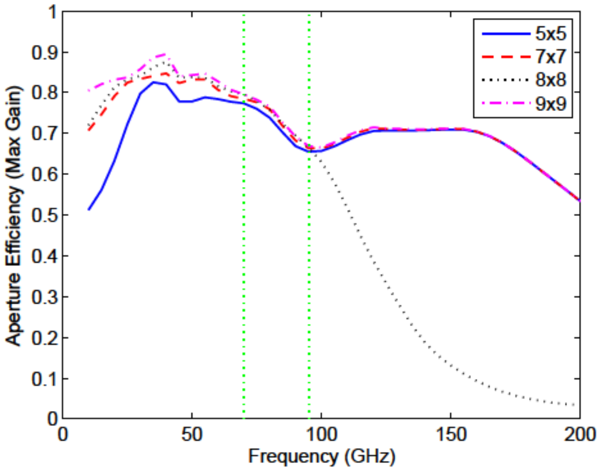

Figure 4.27: Aperture efficiency at the boresight direction for N×N array feeds at different frequencies, with reflector *f*/D = 1.9.

Aperture efficiency for the boresight beam over frequencies are shown in Figure 4.27. In the frequency range from 70 GHz to 95 GHz, aperture efficiency keeps the same as the array element number increases from 25 to 81. However, the aperture efficiency for the 8×8 array is significantly decreased from 100 GHz to 200 GHz. The reason is that when the array has an even number of elements, the center element is not at the focal point of the reflector, so that the two center elements dominate the beamformer weights. When the element spacing is larger than 2 λ (100 GHz), grating lobes appears for the formed beam, which leads to a decrease in the aperture efficiency.

In order to investigate the details of differences between the even number array and odd number array, the aperture efficiency maps of a 7×7 array and an 8×8 array at 90 GHz and 120

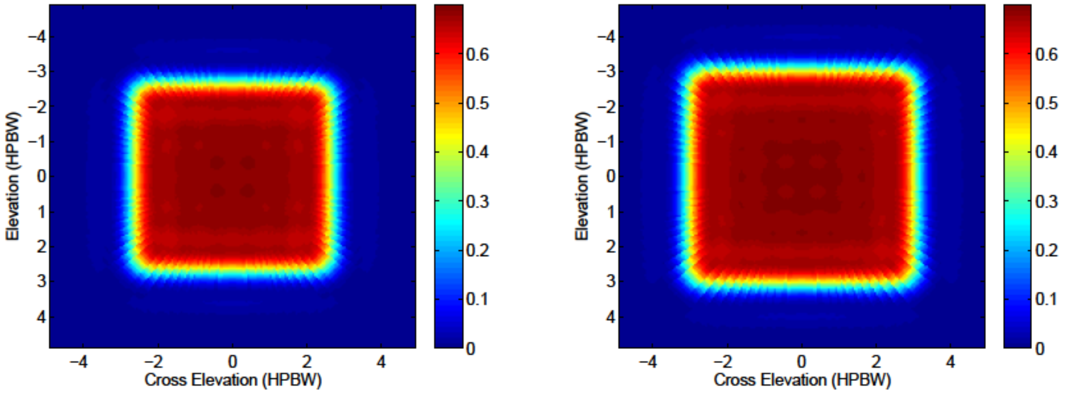

(a) 7×7 array at 90 GHz.

(b) 8×8 array at 90 GHz.

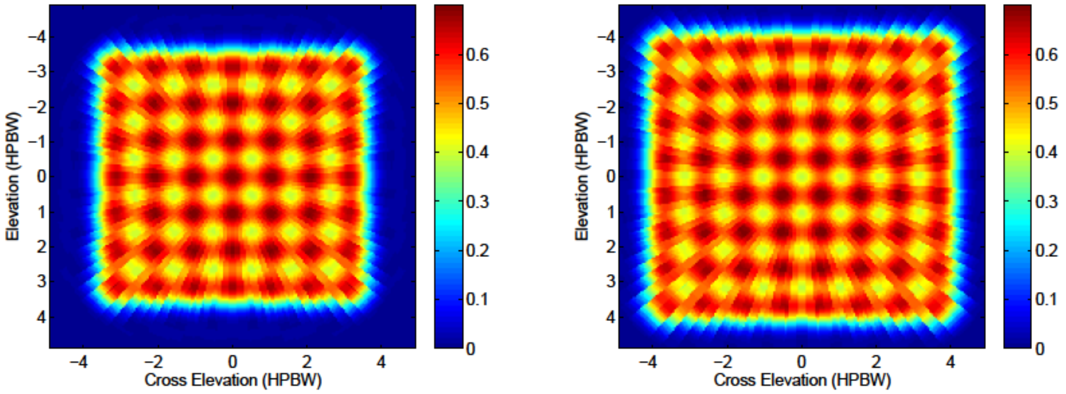

(c) 7×7 array at 120 GHz.

(d) 8×8 array at 120 GHz.

Figure 4.28: Aperture efficiency maps with f/D = 1.9.

GHz are compared in Figure 4.28. At 90 GHz, since the Airy pattern can be fully sampled within the field of view, the map of aperture efficiency is uniform. However, ripples appear in the map of aperture efficiency for both arrays when the frequency is increased from 90 GHz to 120 GHz. The reason for the ripples within the field of view is due to the large element electrical spacing at high frequencies leading to fewer samples of the Airy pattern when the beam is steered.

From the above study, we can conclude that at the frequencies of interest, aperture efficiency is close among different element number arrays. Sensitivity map for an 8×8 array feed is uniform within the field of view at the frequencies of interest.

4.9 Accuracy Analysis of PAF Noise Model

A noise model has been developed by Professor Karl Warnick and other graduate students to analyze the performance of a PAF system. A Matlab package for this model is used to calculate the figures of merit for the PAF system with the embedded radiation pattern and impedance of an array feed combined with an analytical reflector antenna model. For the calculation of aperture efficiency using the maximum-gain beamformer, there are three main parts in the Matlab package:

1) When each antenna element in the array is excited by an input 1 W source, the embedded field and impedance of each antenna element are exported from the array HFSS model. The embedded radiated field of the array element with the terminals of other elements loaded is then transferred to the array element with 1 A current excitation and the terminals of other elements open circuited.

2) Calculate the pattern overlap matrix from the embedded radiated field of each array element and other quantities.

3) Combine an analytical reflector model using physical optics (PO) method to calculate aperture efficiency.

The accuracy of this PAF noise model will be analyzed for calculating aperture efficiency with the maximum-gain beamformer. The reason for analyzing the aperture efficiency is that the system noise budget is complicated, such as the parameters of LNAs, impedance matches between antennas and LNAs, noise environment variation and so on. Aperture efficiency with the maximum-gain beamformer relates to the antenna radiation pattern, which is helpful to simplify the analysis and easily check the accuracy of each part in the Matlab package.

In this section, the conversion of array element radiated fields from the open circuit to impedance load will be studied, and the predicted results will be verified by an antenna HFSS model with different excitations. The overlap matrix will be calculated using the independent code to compare the results from the Matlab package. An HFSS reflector model is used to compare the analytical reflector model. In order to better understand the calculated results from the PAF noise model, array feeds with wave port and probe excitation, the GBT2 dipole PAF and mm-wave PAF are studied in this section.

4.9.1 Array Embedded Radiated Fields Conversion

In this section, a general formula for converting the embedded radiated fields from an array antenna with open circuit and impedance load is derived. Based on this general formula, a conversion of HFSS lumped port fields to open circuit fields is derived. Using a full-wave method, this formula will be proven by comparing a single bow-tie antenna and the corresponding array antenna with lumped port feed and current feed.

Conversion of Array Embedded Radiated Fields with Different Loads

A conversion of an array embedded radiated fields between different loads is studied. As shown in Figure 4.29, the mth element is excited by an input current i_{in} and the corresponding embedded radiated fields with loads Z and Z' are E and E', respectively. The object of this study is to find the relationship of the embedded radiated fields between different source impedances.

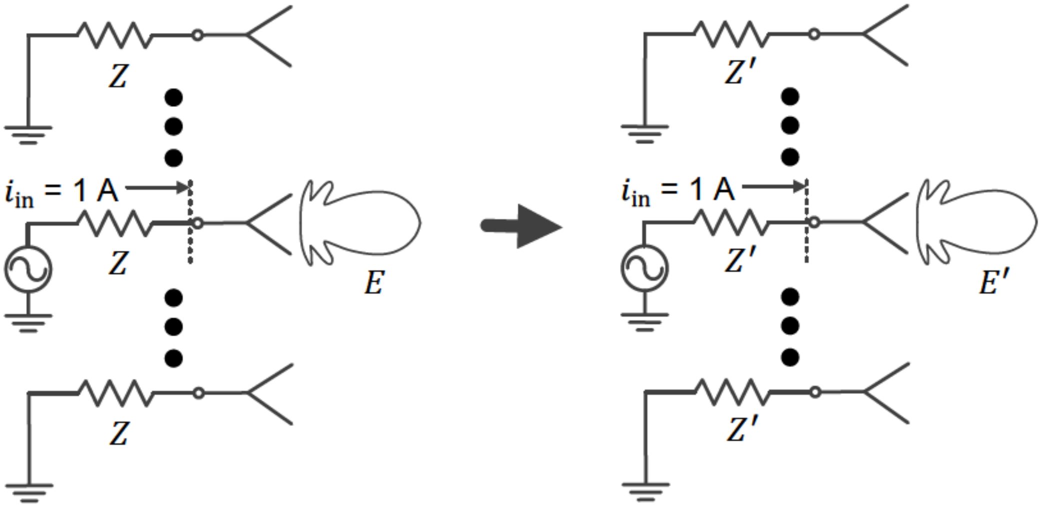

Figure 4.29: Block diagrams for an array antenna with loads Z and Z'.

We first convert an array element with load Z to open circuit terminations. In Figure 4.30, when the nth element of the array is excited, the radiation pattern E_n with load Z can be considered

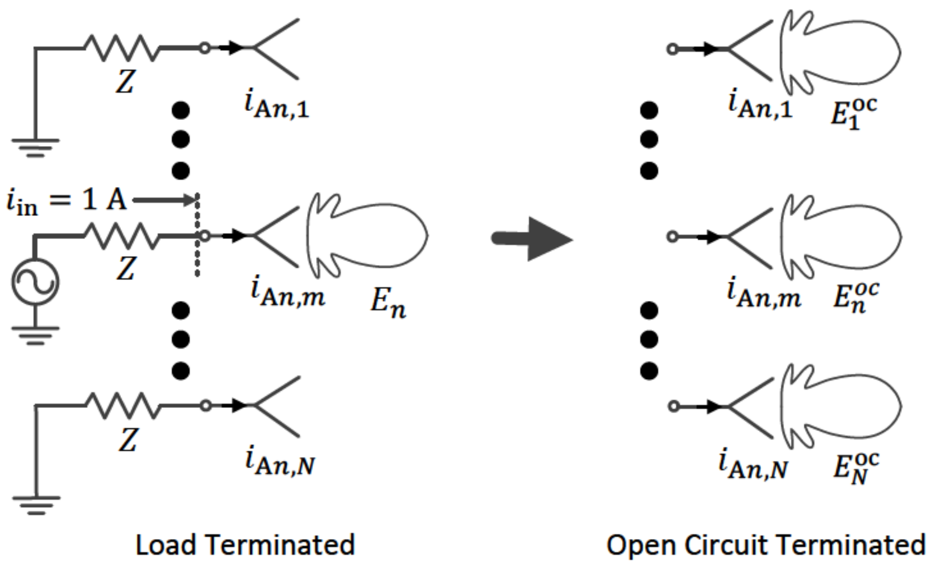

Figure 4.30: Block diagrams for converting array embedded radiated fields with the terminals of load Z to open circuit terminated.

as a combination of the open circuit radiation pattern E_m^{oc} with weights $i_{\mathrm{An},m}$ by

$$E_n = \sum_{m=1}^{N} i_{\mathrm{An},m} E_m^{\mathrm{oc}}. \tag{4.17}$$

where $i_{\mathrm{An},m}$ represents the current distribution on the mth element of an array when the nth element is excited by an input current i_{in}. $\bar{i}_{\mathrm{An}}$ can be written as

$$\begin{aligned} \bar{i}_{\mathrm{A}n} &= (\mathbf{I} - \mathbf{S})\bar{i}_{\mathrm{in}} \\ &= \underbrace{[\mathbf{I} - (\mathbf{Z}_{\mathrm{A}} + Z\mathbf{I})^{-1}(\mathbf{Z}_{\mathrm{A}} - Z\mathbf{I})]}_{\mathbf{T}}\bar{i}_{\mathrm{in}} \end{aligned} \tag{4.18}$$

where $\mathbf{Z}_\mathrm{A}$ is the array antenna impedance matrix, and $\mathbf{S}$ is an S-parameter matrix. In terms of the nth element excitation, $\bar{i}_\mathrm{in}$ is equal to $(0,\ldots,0,1,0,\ldots,0)^\mathrm{T}$ and $\bar{i}_{\mathrm{A}n}$ is

$$\begin{bmatrix} i_{\mathrm{A}n,1} \\ i_{\mathrm{A}n,2} \\ \vdots \\ i_{\mathrm{A}n,\mathrm{N}} \end{bmatrix} = \begin{bmatrix} T_{11} & T_{12} & \cdots & T_{1N} \\ T_{21} & T_{22} & \cdots & T_{2N} \\ \vdots & \vdots & \ddots & \vdots \\ T_{N1} & T_{N2} & \cdots & T_{NN} \end{bmatrix} \begin{bmatrix} 0 \\ \vdots \\ 0 \\ 1 \\ 0 \\ \vdots \\ 0 \end{bmatrix} = \begin{bmatrix} T_{1n} \\ T_{2n} \\ \vdots \\ T_{Nn} \end{bmatrix} = \mathbf{T}^{(n)}, \tag{4.19}$$

or

$$i_{\mathrm{A}n,m} = T_{m,n}. \tag{4.20}$$

If the radiation pattern for the loaded array is written as a vector $\overline{E}$, then

$$\begin{bmatrix} E_1 \\ E_2 \\ \vdots \\ E_N \end{bmatrix} = \mathbf{i}_\mathrm{A} \begin{bmatrix} E_1^\mathrm{oc} \\ E_2^\mathrm{oc} \\ \vdots \\ E_N^\mathrm{oc} \end{bmatrix}. \tag{4.21}$$

Since the matrix $\mathbf{i}_\mathrm{A}$ is equal to $\mathbf{T}^T$, $\overline{E}$ can be written as

$$\begin{bmatrix} E_1 \\ E_2 \\ \vdots \\ E_N \end{bmatrix} = \mathbf{T}^T \begin{bmatrix} E_1^\mathrm{oc} \\ E_2^\mathrm{oc} \\ \vdots \\ E_N^\mathrm{oc} \end{bmatrix}, \tag{4.22}$$

and $\overline{E}^{\text{oc}}$ is

$$\begin{bmatrix} E_1^{\text{oc}} \\ E_2^{\text{oc}} \\ \vdots \\ E_N^{\text{oc}} \end{bmatrix} = (\mathbf{T}^T)^{-1} \begin{bmatrix} E_1 \\ E_2 \\ \vdots \\ E_N \end{bmatrix}. \tag{4.23}$$

Therefore, the relationship of the radiated fields between the open circuit array and the terminal loaded Z_{L} array is

$$\begin{aligned} \overline{E}^{\text{oc}} &= [(\mathbf{I}-\mathbf{S})^T]^{-1}\overline{E} \\ &= \{[\mathbf{I}-(\mathbf{Z}_{\text{A}}+\mathbf{Z})^{-1}(\mathbf{Z}_{\text{A}}-\mathbf{Z})]^T\}^{-1}\overline{E} \end{aligned} \tag{4.24}$$

Using the same method, the field $\overline{E}^{\text{oc}}$ with terminal loaded $Z^{'}$ is

$$\begin{aligned} \overline{E}^{\text{oc}} &= [(\mathbf{I}-\mathbf{S}^{'})^T]^{-1}\overline{E}^{'} \\ &= \{[\mathbf{I}-(\mathbf{Z}_{\text{A}}+\mathbf{Z}^{'})^{-1}(\mathbf{Z}_{\text{A}}-\mathbf{Z}^{'})]^T\}^{-1}\overline{E}^{'} \end{aligned} \tag{4.25}$$

Combine Equation 4.24 and 4.25, the relationship of the radiated fields with terminators of load $Z^{'}$ and Z is

$$\overline{E}^{'} = (\mathbf{I}-\mathbf{S}^{'})^T[(\mathbf{I}-\mathbf{S})^T]^{-1}\overline{E} \tag{4.26}$$

Conversion of HFSS Lumped Port Fields to Open Circuit Fields

For convenience, the radiated field for an array element used in a PAF noise model is the embedded far field evaluated at one meter away from the antenna, when the antenna element is excited by an 1 A current source and the terminals of the other elements are open circuited. However, in a HFSS model with the lumped port excitation, the excited source is a 1 W input power. In order to qualify the fields requirement for the PAF noise model, it is necessary to convert the radiated fields from the lumped port excitation with the terminals of the other elements loaded to the current excitation with open circuited. The corresponding block diagrams are shown in Figure 4.31.

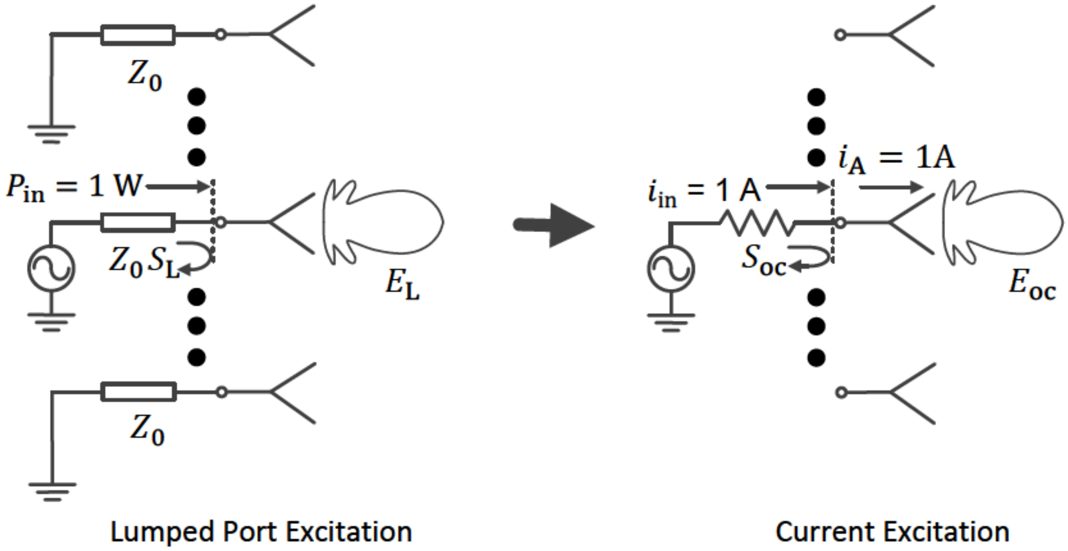

Figure 4.31: (Left) E_{L} is the embedded radiated field when the nth element is excited by an input power with the terminals of the other elements loaded. (Right) E_{oc} is the embedded radiated field when the nth element is excited by an input current with the terminals of the other elements open circuited.

Using Equation 4.26, the open circuit embedded radiated fields in Figure 4.31 can be written as

$$\overline{E}_{\text{oc}} = \sqrt{\frac{2P_{\text{in}}}{Z_{\text{L}}}}(\mathbf{I}-\mathbf{S}_{\text{oc}})^T[(\mathbf{I}-\mathbf{S}_{\text{L}})^T]^{-1}\overline{E}_{\text{L}} \tag{4.27}$$

where $\sqrt{2P_{\text{in}}/Z_{\text{L}}}$ is a scaled factor used to normalize 1 W input power to 1 A input current, and $\mathbf{S}_{\text{oc}}$ and $\mathbf{S}_{\text{L}}$ are the scattering matrix for the current excitation and lumped port excitation array model, respectively.

For the nth element in the antenna current excitation model, since the excited current i_{in} is equal to antenna current i_{A}, the diagonal elements in the scattering matrix $\mathbf{S}_{\text{oc}}$ is zero due to the impedance matching between the antenna and load impedance. Because the terminals of all the other elements are open circuited, there is no energy coupled to the terminals of these elements, which causes the off-diagonal elements in $\mathbf{S}_{\text{oc}}$ to be zero. Based on the these facts, $\mathbf{S}_{\text{oc}}$ is a zero matrix and $\overline{E}_{\text{oc}}$ becomes

$$\begin{aligned}\overline{E}_{\text{oc}} &= \sqrt{\frac{2P_{\text{in}}}{Z_{\text{L}}}}[(\mathbf{I}-\mathbf{S}_{\text{L}})^T]^{-1}\overline{E}_{\text{L}} \\ &= \sqrt{\frac{2P_{\text{in}}}{Z_{\text{L}}}}[\mathbf{I}-(\mathbf{Z}_{\text{A}}+Z_0\mathbf{I})^{-1}(\mathbf{Z}_{\text{A}}-Z_0\mathbf{I})])^T]^{-1}\overline{E}_{\text{L}} \qquad (4.28)\end{aligned}$$

Verification by HFSS Lumped Port and Current Feed

In order to verify Equation 4.28 for the radiation pattern conversion, a single planar bow-tie dipole antenna and its corresponding array antenna are studied using a full-wave method.

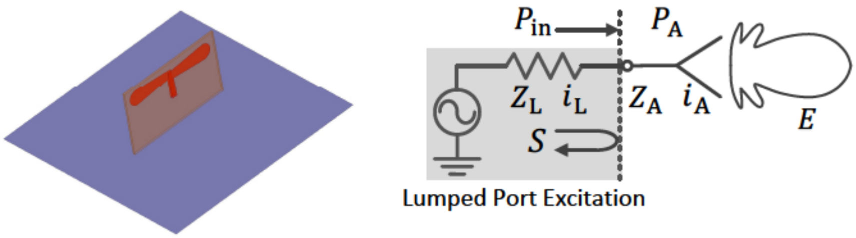

(a) HFSS model (b) Lumped port feed circuit model.

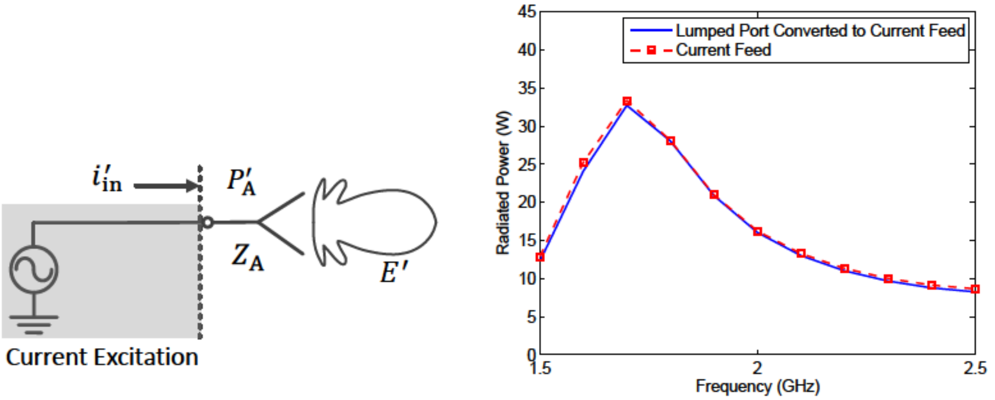

(c) Current Feed circuit model. (d) Comparison of radiated power.

Figure 4.32: The first figure shows a single bow-tie antenna with a finite ground plane. The second and third figures shows the corresponding circuit block diagrams for the lumped port feed and the current feed. The fourth figure shows a comparison of the radiated power of a single antenna with the converted current feed HFSS model using Equation 4.28 and the current feed HFSS model.

A single antenna is helpful to simplify the model and can be easily understood because there is no mutual-coupling effect. The model for a single bow-tie antenna is shown in Figure 4.32a.

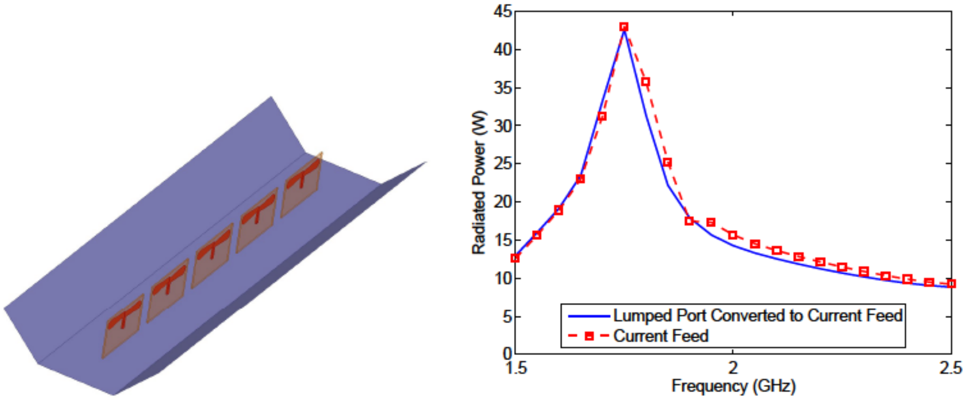

(a) Array HFSS model.

(b) Radiated power.

Figure 4.33: Comparison of the radiated power of an array antenna with the converted current feed HFSS model using Equation 4.28 and the current feed HFSS model.

The block diagrams of the corresponding circuit models with the lumped port feed and the current feed are shown in Figure 4.32b and Figure 4.32c, respectively. For the lumped port feed model, the impedance of lumped port is complex conjugated matched to the characteristic impedance of the transmission line connecting to the antenna. For current feed model, the excited current source is implemented by placing a surface between two conductors, which enforces the tangential component of magnetic field related to the surface current. The excited surface current between the two conductors is equal to the antenna current.

Using Equation 4.28, the radiated fields with lumped port feed can be converted to the radiated fields with current feed. Radiated power is studied to verify the accuracy of the converted fields. After integrating the embedded radiated fields of the center element over an entire sphere, the radiated power of the converted current feed from the lumped port feed is compared to that of the current feed. The results are shown in Figure 4.32d, where the radiated powers are close in value.

Using the similar method, Equation 4.28 is applied to the planar bow-tie array antenna model in Figure 4.33a. The radiated power from the integral of radiated fields of the array center element is studied. As shown in Figure 4.33b, a comparison of the radiated power is made between the converted current feed and the current feed. The result shows that the radiated power for two cases are close.

The radiated power over frequency for the single and array antenna models show a small difference. The reason is that in the current feed model, there is parasitic capacitance between the two conductors of transmission line connecting to the antenna, which leads to a small change in the antenna impedance.

4.9.2 Comparison of Aperture Efficiency with Different Reflector Models

A reflector antenna model is based on the physical optics (PO) approximation to calculate the secondary radiated far-field of the PAF. The edge diffraction effect is ignored in the reflector model. In this section, the accuracy of the analytical reflector model will be verified by a HFSS reflector model. Reflector aperture efficiency with the maximum gain beamformer for a 5×5 PAF model will be studied. The models for comparison include an array and reflector analytical model, an array HFSS model with a reflector analytical model, and an array and reflector HFSS model.

In this section, the HFSS-FEM solver is used to simulate the radiated field and impedance of an array antenna. The embedded E-field of each array element sets as an incident field to a reflector antenna using the HFSS-PO solver.

A comparison of different PAF models is shown in Figure 4.34, including an array HFSS model and reflector analytical model, an array and reflector analytical model, and an array and reflector HFSS model. From these plots, it can be seen that when using the simulated radiated field and impedance from the array HFSS model, the aperture efficiency of the reflector analytical model is higher than that of the reflector HFSS model. The reason is attributed to diffraction effects that are ignored in the reflector analytical model, leads to less spillover loss. Meanwhile, in the calculation of aperture efficiency using the Matlab package for the array model, the total radiated power from PAF is calculated from the PAF antenna impedance by

$$P_{\mathrm{rad}} = \frac{1}{2}\mathbf{i}_{\mathrm{A}}^{H}\mathrm{Re}[\mathbf{Z}_{\mathrm{A}}]\mathbf{i}_{\mathrm{A}}. \tag{4.29}$$

Theoretically, for a lossless antenna, the radiated power from Equation 2.26 is the same as Equation 4.29. Due to the numerical errors in HFSS, P_{rad} in Equation 4.29 is smaller than that in Equation 2.26, which leads to a higher aperture efficiency when using the Matlab package to calculate the array HFSS model and reflector analytical model.

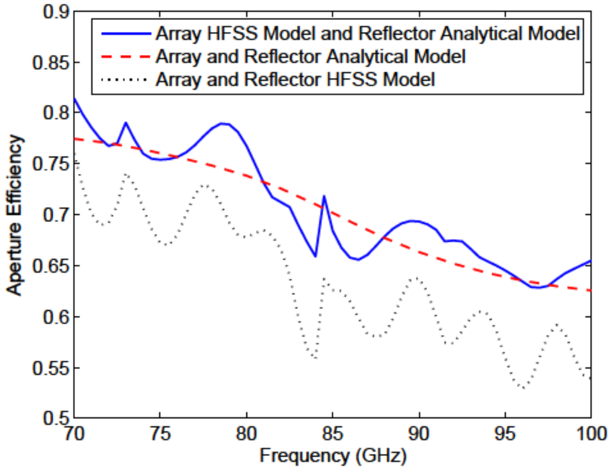

Figure 4.34: Comparison of aperture efficiency between an array and reflector analytical model, an array HFSS model with a reflector analytical model, and an array and reflector HFSS model. A 64-element mm-wave phased array feed associated with a reflector with 1.9 f/D is used for analysis.

4.9.3 Comparison of a mm-wave Array Element with Probe and Wave Port Feed

The excitation for a horn antenna in the full-wave model can be either a probe feed or a wave port feed. The characteristic impedance for the probe feed is constant over frequencies, but is frequency dependent for the wave port feed. To validate the accuracy of the PAF model for different excitation methods, a 5×5 PAF model with probe feed and wave port feed are studied in this section.

As shown in Figure 4.35, for a transmitting antenna system, a voltage source with a generator impedance Z_g transmits signals to an antenna with impedance Z_A via a transmission line with characteristic impedance Z_0. In order to achieve the maximum power transfer, the input impedance of the antenna Z_{in} (the reference plane is between the transmission line and the excitation source) should be complex conjugate match to the impedance Z_g. In the PAF model analysis, the antenna is a receiving antenna and the impedance Z_g is the impedance of LNAs, which is assumed to be complex conjugate matching to the impedance Z_0.

In the FEM model, the excitation for a horn antenna can be set as a wave port feed or a probe feed. As shown in Figure 4.36a, a horn antenna using the wave port excitation can be considered as an antenna fed by an infinite long waveguide transmission line. The wave port

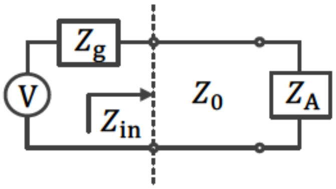

Figure 4.35: Block diagram for a transmitting antenna system.

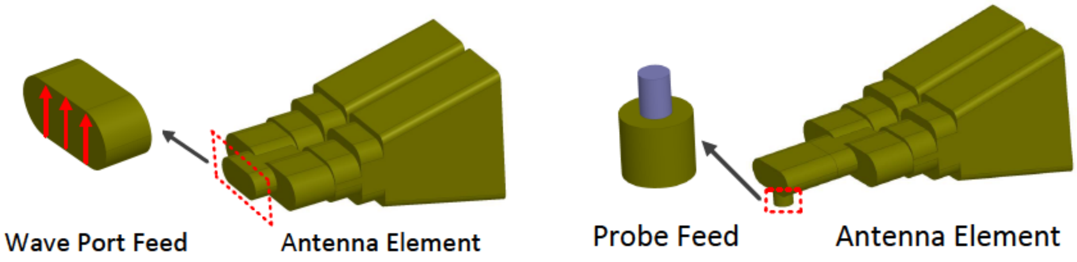

(a) Wave port excitation.

(b) Probe excitation.

Figure 4.36: An array element model with different excitation methods.

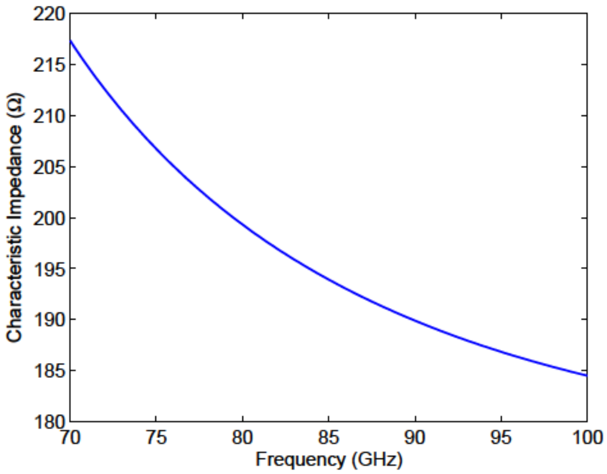

Figure 4.37: Characteristic impedance of a waveguide transmission line (as shown Figure 4.36a) with the fundamental mode excitation.

impedance is related to the characteristic impedance Z_0 of the waveguide transmission line, which is complex conjugated matched to the generator impedance Z_g. Figure 4.36b shows that a probe connecting to the inner conductor of a coaxial line is used as the feed of the horn antenna. The antenna impedance Z_A can be close to the conjugate match of the coaxial line impedance Z_0 by adjusting the length and position of the probe.

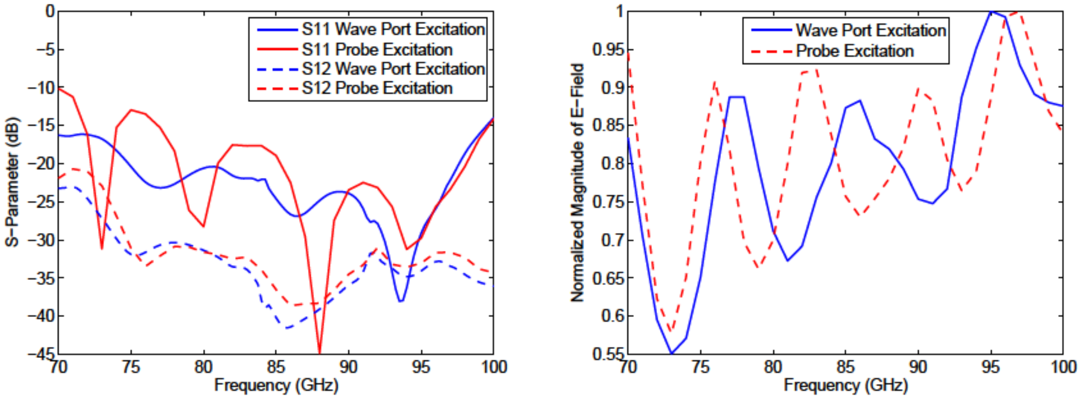

(a) S-parameters.

(b) E-field in the boresight direction.

Figure 4.38: Comparison between wave port and probe excitation for the radiation performance of the embedded center element of a 5×5 array.

The characteristic impedance Z_0 for the coaxial line is fixed to be a constant of 50 Ω, but that for the waveguide transmission line changes with frequency. The reason is that the field distribution at the cross section of the waveguide is changed with the frequency but is constant for the coaxial line. Figure 4.37 shows the characteristic impedance Z_0 of the waveguide transmission line in Figure 4.36a over frequency.

In a PAF model, in order to satisfy the requirement for noise match between the LNAs and the antennas, the impedance of the LNAs is assumed to be 50 Ω for the probe excitation but changing with frequency (as shown in Figure 4.37) for the wave port excitation.

The radiated field and impedance of the embedded center element of a 5×5 array for two different excitation methods are compared over frequency. Figure 4.38a shows a comparison of S parameters, which is related to the input impedance of the antennas. Figure 4.38b shows a comparison of the normalized magnitude of E-field at the boresight direction after using Equation 4.28. It can be seen that the antenna input impedance and radiation pattern versus frequency for the wave port and probe excitations are close. The reason for the difference is that only the dominant mode is excited for the wave port feed, but the high order modes are excited by the probe feed.

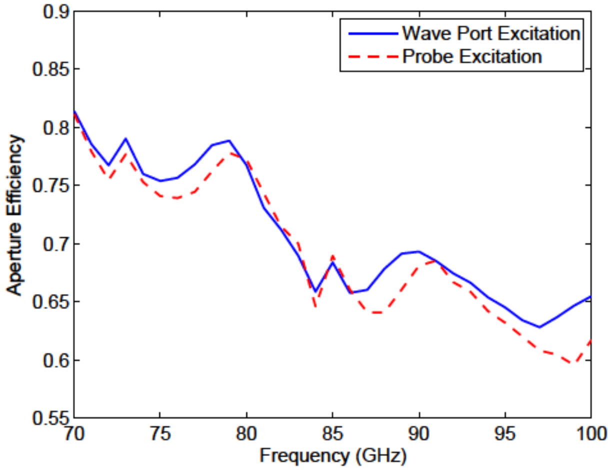

Figure 4.39: Comparison of aperture efficiency for a 5×5 array feed using the wave port and probe excitation.

Combined with a reflector model, the radiation pattern and impedance of the array antenna are used to calculate the aperture efficiency with the maximum-gain beamformer over frequency. A comparison result for the two different excitation methods is shown in Figure 4.39, where the predicted aperture efficiency are close.

From the above study, we can conclude that the PAF noise model can be used to accurately analyze the array antenna with different excitation methods. If we assume that the impedance of the LNAs are complex conjugate matched to the characteristic impedance of the transmission lines, the performance for a PAF system with different excitation methods are close.

4.9.4 Comparison of Aperture Efficiency between L-band and mm-wave PAF

In this section, aperture efficiency with the maximum-gain beamformer for an L-band 19-element GBT2 dipole array feed and a 25-element mm-wave UMass horn array feed are compared by using the PAF noise model.

In order to simplify the analysis and ignore the mutual-coupling effects between each element, we begin with the study of a single isolated array element. Figure 4.40a and 4.40b show the aperture efficiency for an isolated single GBT2 dipole antenna and the UMass horn antenna respectively. The *f*/D of the reflector for the array feeds is 0.7 and 1.9 respectively. It is expected that both antenna feeds will exhibit low aperture efficiency, because the single antenna fails to form

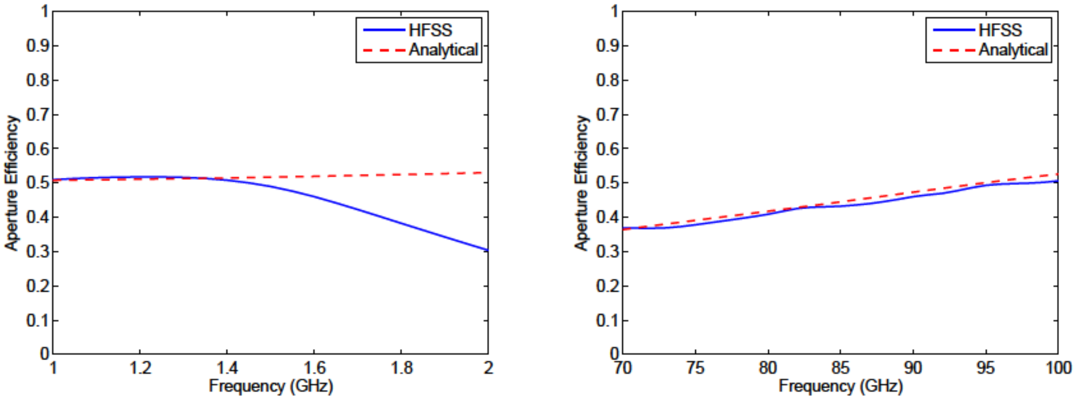

(a) Single GBT2 Dipole Antenna feed (b) Single UMass horn Antenna feed

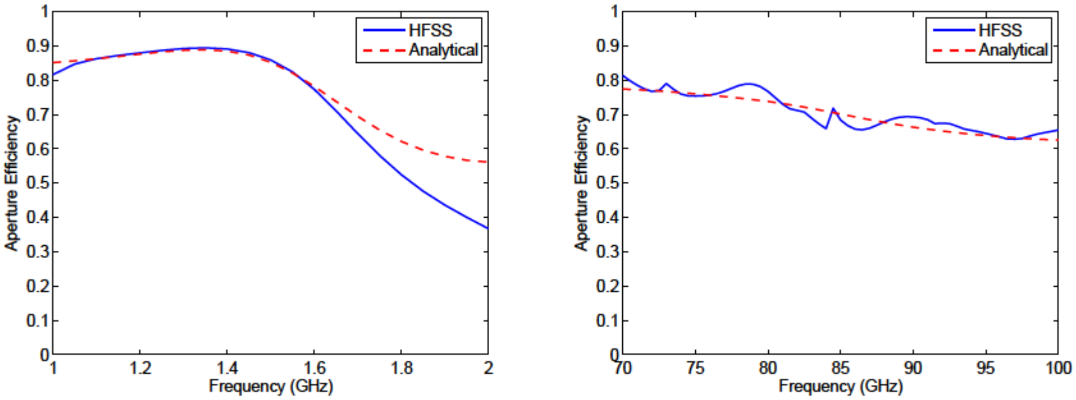

(c) 19-element GBT2 Dipole array feed (d) 25-element UMass horn array feed

Figure 4.40: Aperture efficiency for GBT2 L-band dipole antenna and UMASS mm-wave horn antenna. Upper plots are single antennas and the bottom plots are their corresponding array antennas. f/D of the reflector used for dipole array feed and horn array feed is 0.7 and 1.9 respectively.

a narrow enough beam to illuminate the reflector antenna. The differences in aperture efficiency between the antennas is due to the differences of the f/D of the reflector and the antenna radiation patterns. In terms of comparison between the full-wave and analytical model, there is a good match for the single UMass horn antenna feed, but a significant difference for the single GBT2 dipole antenna feed at high frequencies. This is because that the analytical model for the dipole antenna is a half wavelength dipole antenna, but there is a big gap between the two arms in the full-wave dipole antenna model, which makes the effective length of the real dipole antenna less than that of an analytically modeled dipole antenna.

Figure 4.40c and 4.40d show the aperture efficiency for a 19-element GBT2 dipole array feed and a 25-element UMass horn array feed. It can be seen that there is less difference between the HFSS and analytical result for the dipole array feed.

The aperture efficiency in HFSS for the horn array feed shows more variation over frequency than the dipole array feed. The aperture efficiency for horn array feed changes from 0.66 at 84 GHz to 0.71 at 84.5 GHz. In order to investigate the details of this problem, we studied the radiation pattern and the antenna aperture field distribution at these frequencies. The magnitude of E-field for the isolated single horn antenna is shown in Figure 4.41a and the embedded center element radiated E-field are shown in Figure 4.41b. It can be seen that there is less difference in the E-field between 84 GHz and 84.5 GHz for the isolated single antenna than that for the embedded array center element. Figure 4.42 shows the aperture field distribution on the array aperture at two frequencies when the center element is excited. The aperture fields on the excited element and other array elements show a large difference. Since the aperture efficiency depends on the radiated field of the array antenna, which is related to the antenna aperture field distribution, we can conclude that the changing of aperture field distribution of the array embedded element over frequency causes a variation of reflector aperture efficiency.

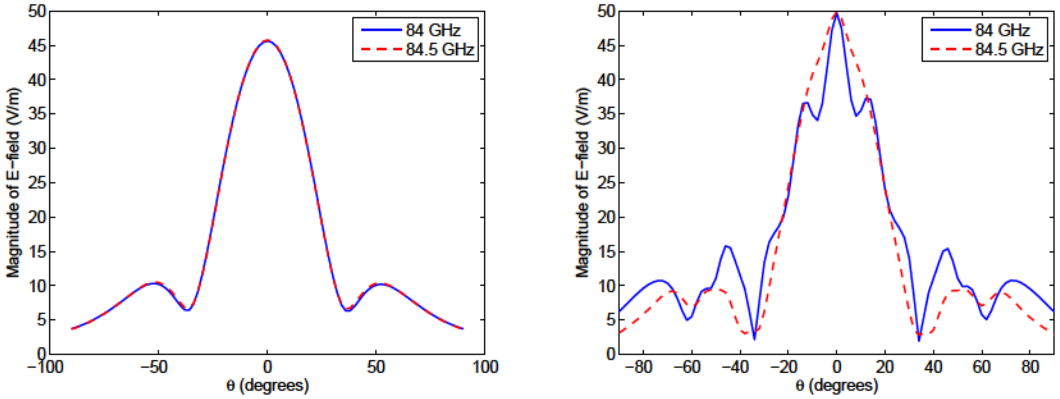

(a) Isolated single antenna.

(b) Embedded array center element.

Figure 4.41: Simulated magnitude of E-field from HFSS for an isolated single UMass mm-wave antenna feed and the corresponding 5×5 array feed at 84 GHz and 84.5 GHz respectively.

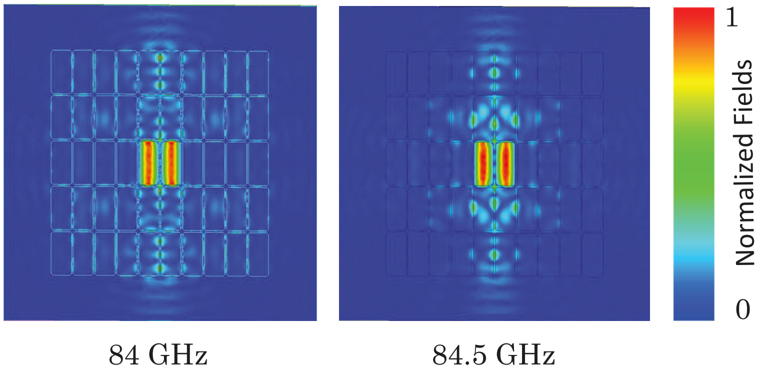

Figure 4.42: Magnitude of aperture field distribution for an 5×5 UMASS mm-wave array at 84 GHz and 84.5 GHz when the center element is excited.

4.10 Experimental Test for the Green Bank Telescope

The 64-element mm-wave phased array feed was mounted and test in the Green Bank telescope with 100-meter diameter dish on November, 2015. This section first introduces formulas used to analyze the raw data from the test results, and then shows the test results for the phased array feed.

4.10.1 System Noise Temperature for Single Element

When the antenna points to an absorber at the room temperature, the output power of the array feed is

$$P_{\text{hot}} = k_{\text{b}}(T_{\text{rec}} + T_{\text{amb}})B \tag{4.30}$$

where k_{b} is the boltzmann constant, B is the system bandwidth, T_{rec} is the receiver equivalent noise temperature and T_{amb} is the absorber equivalent brightness temperature.

When the antenna points to the cold sky, the output power of the array feed is

$$\begin{aligned} P_{\text{cold}} &= k_{\text{b}}T_{\text{sys}}B && (4.31) \\ &= k_{\text{b}}(T_{\text{rec}} + T_{\text{sky}} + T_{\text{spillover}})B && (4.32) \end{aligned}$$

where T_{sky} and $T_{\text{spillover}}$ is the equivalent noise temperature contributed by the warm sky and the spillover from the reflector respectively.

From (4.30) and (4.32), T_{rec} can be written as

$$T_{\text{rec}} = \frac{P_{\text{cold}}T_{\text{amb}} - P_{\text{hot}}T_{\text{sky}} - P_{\text{hot}}T_{\text{spillover}}}{P_{\text{hot}} - P_{\text{cold}}} \tag{4.33}$$

Then T_{sys} becomes

$$\begin{aligned} T_{\text{sys}} &= T_{\text{rec}} + T_{\text{sky}} + T_{\text{spillover}} \\ &= \frac{P_{\text{cold}}T_{\text{amb}} - P_{\text{hot}}T_{\text{sky}} - P_{\text{hot}}T_{\text{spillover}}}{P_{\text{hot}} - P_{\text{cold}}} + T_{\text{sky}} + T_{\text{spillover}} \\ &= \frac{P_{\text{cold}}(T_{\text{amb}} - T_{\text{sky}} - T_{\text{spillover}})}{P_{\text{hot}} - P_{\text{cold}}} \end{aligned} \tag{4.34}$$

For the UMASS method, T_{sky} and $T_{\text{spillover}}$ are approximately equal to 0, and T_{sys} becomes

$$T_{\text{sys}}^{\text{UMASS}} = \frac{P_{\text{cold}}T_{\text{amb}}}{P_{\text{hot}} - P_{\text{cold}}} \tag{4.35}$$

4.10.2 System Noise Temperature with Beamforming

Steering vector $\mathbf{v}$ can be calculated from

$$\mathbf{R}_{\text{source}}\mathbf{v} = \lambda_{\max}\mathbf{R}_{\text{cold}}\mathbf{v}, \tag{4.36}$$

where the $\mathbf{R}_{\text{source}}$ and $\mathbf{R}_{\text{cold}}$ are correlation matrix when the telescope points to the source and cold sky, respectively. $\lambda_{\max}$ is the maximum generalized eigenvalue.

The maximum sensitivity beamformer weights can be calculated from

$$\mathbf{w} = \mathbf{R}_{\text{cold}}^{-1}\mathbf{v}. \tag{4.37}$$

After applying beamformer weights to each receiving element and summing all the elements output power, the total output power becomes

$$P_{\mathrm{cold}}^{\mathrm{bf}} = \mathbf{w}^H \mathbf{R}_{\mathrm{cold}} \mathbf{w} \tag{4.38}$$

$$P_{\mathrm{hot}}^{\mathrm{bf}} = \mathbf{w}^H \mathbf{R}_{\mathrm{hot}} \mathbf{w} \tag{4.39}$$

$$P_{\mathrm{source}}^{\mathrm{bf}} = \mathbf{w}^H \mathbf{R}_{\mathrm{source}} \mathbf{w} \tag{4.40}$$

From these formulas, the receiver noise temperature $T_{\mathrm{rec}}^{\mathrm{bf}}$ and system noise temperature $T_{\mathrm{sys}}^{\mathrm{bf}}$ using beamformer can be calculated from (4.33) and (4.34).

The strict way to calculate the system noise temperature is

$$\begin{aligned} T_{\mathrm{sys}}^{\mathrm{bf}} &= T_{\mathrm{amb}} \frac{\mathbf{w}^H \mathbf{R}_{\mathrm{noise}} \mathbf{w}}{\mathbf{w}^H \mathbf{R}_{\mathrm{t}} \mathbf{w}} && (4.41) \\ &= T_{\mathrm{amb}} \frac{\mathbf{w}^H \mathbf{R}_{\mathrm{cold}} \mathbf{w}}{\mathbf{w}^H \mathbf{R}_{\mathrm{t}} \mathbf{w}} && (4.42) \\ &= T_{\mathrm{amb}} \frac{P_{\mathrm{cold}}^{\mathrm{bf}}}{P_{\mathrm{t}}} && (4.43) \end{aligned}$$

where $\mathbf{R}_{\mathrm{t}}$ is the correlation matrix for isotropic noise response of the array feed if assuming the receiver is lossless.

Assuming the array antennas are under impedance match with the loads and the antenna is lossless, the isotropic input power P_{t} to the antenna load can be written as

$$P_{\mathrm{t}} = k_{\mathrm{b}} T_{\mathrm{amb}} B \tag{4.44}$$

$P_{\mathrm{hot}}^{\mathrm{bf}}$ including the isotropic external noise and the receiver noise can be written as

$$\begin{aligned} P_{\mathrm{hot}}^{\mathrm{bf}} &= P_{\mathrm{t}} + P_{\mathrm{rec}}^{\mathrm{bf}} \\ &= k_{\mathrm{b}} T_{\mathrm{amb}} B + k_{\mathrm{b}} T_{\mathrm{rec}}^{\mathrm{bf}} B && (4.45) \end{aligned}$$

From (4.44) and (4.45), P_t becomes

$$P_\mathrm{t} = \frac{T_\mathrm{amb}}{T_\mathrm{amb} + T_\mathrm{rec}^\mathrm{bf}} P_\mathrm{hot}^\mathrm{bf} \tag{4.46}$$

Finally, the system noise temperature with beamforming is

$$T_\mathrm{sys}^\mathrm{bf} = \frac{(T_\mathrm{amb} + T_\mathrm{rec}^{bf}) P_\mathrm{cold}^\mathrm{bf}}{P_\mathrm{hot}^\mathrm{bf}} \tag{4.47}$$

4.10.3 Test Results

Using the above formulas, the calculated test results are based on the raw data from scan 27 to 29 on November 15th, 2015. The source is SiO OrionKL maser and the integration time is 10 sec. The sky and spillover noise temperature and the system noise temperature are assumed to be 70 K and 110 K respectively. Due to the failure of some LNAs, as illustrated in Figure. 4.43, 38 of 64 element were working by the time of measurement on the GBT.

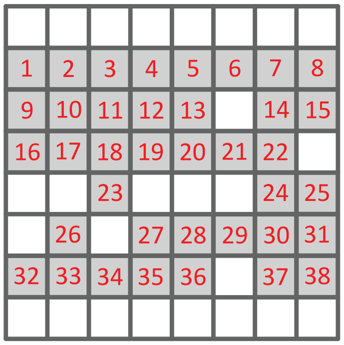

1	2	3	4	5	6	7	8
9	10	11	12	13		14	15
16	17	18	19	20	21	22	
		23				24	25
	26		27	28	29	30	31
32	33	34	35	36		37	38

Figure 4.43: Array layout for 38 of 64 elements used in the observation.

Output powers for each array element are shown in Figure. 4.44. The array element index number corresponds to the number in Figure 4.43. The power is integrated over the dwelling time and frequency bandwidth. The output power for the hot source is higher than that for the other sources. When the telescope points to the astronomical source, the increased output power corresponds to the position of the focal point of the reflector antenna.

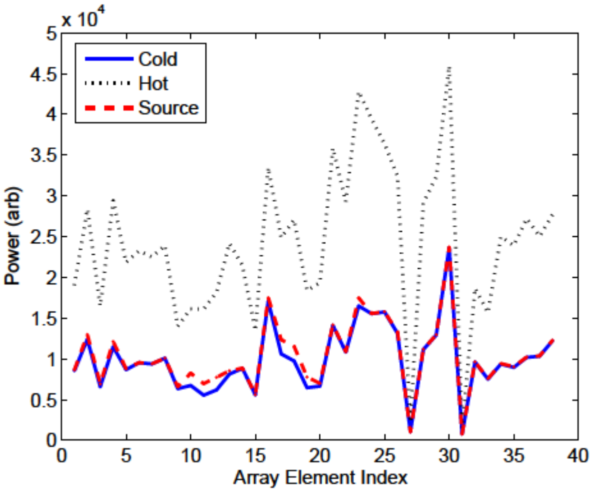

Figure 4.44: Output power for each array element.

The normalized beamformer weights are shown in Figure 4.45, where the Airy disk is located around the 11th element in Figure 4.43. The elements 10, 12, 13, 17, 18, 19 and 20 with relatively low beamformer coefficients correspond to the side lobes of the Airy disk. Elements 3, 27 and 31 with high beamformer coefficients contribute to the low gain LNAs.

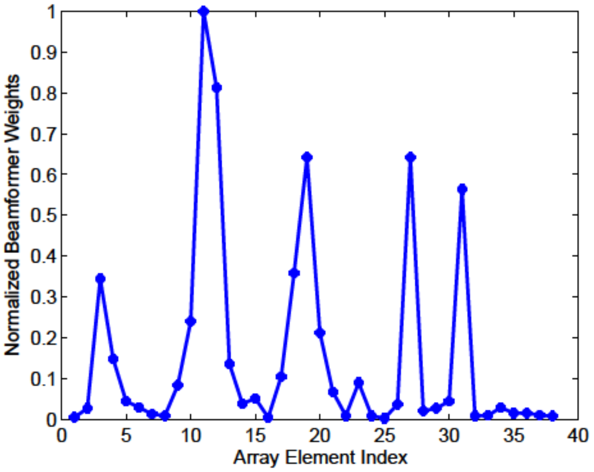

Figure 4.45: Normalized beamformer weights for each array element.

The system output SNR calculated from $(P_{\text{source}} - P_{\text{cold}})/P_{\text{cold}}$ is shown in Figure 4.46. The output SNR for the maximum SNR beamformer is about 3 times higher than that for the single element. However, using the analytical model, the PAF SNR gain is about 1.33 . This might be due to the poor accuracy reflector surface at the W-band, where the gain of the SNR for the test result is higher than that for the simulated result.

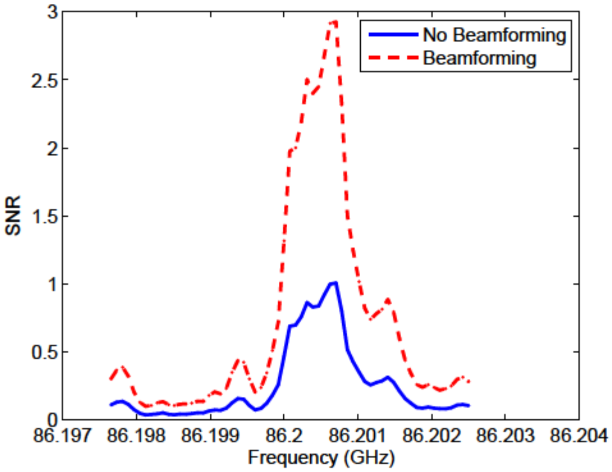

Figure 4.46: System output SNR.

4.11 Summary

In this chapter, the performance of a 64-element mm-wave phased array feed has been analyzed based on a noise model associated with the GBT reflector model. An analytical model has been introduced to speed up the analysis process and the accuracy has been verified by a full-wave model. System performance related to the size of thermal Dewar window, installation position offset from the reflector focal position, required minimum number of array element for beamformer, expected figures of merits on the GBT telescope were studied. The phased array feed was mounted on the GBT and the effectiveness of beamforming has been experimentally demonstrated.

CHAPTER 5. ON THE BANDWIDTH GAP BETWEEN THE ARRAY FEED AND CLUSTER FEED REGIMES FOR BROADBAND MULTIFEED SYSTEMS

For reflector antennas with broadband multiple feed systems, under optimal beamforming conditions the feed operates at low frequencies as a phased array feed, with multiple elements contributing to a synthesized illumination pattern, whereas at high frequencies, each element forms a single independent beam. There is a frequency range between these two regimes where it is difficult to achieve high aperture efficiency, which limits the ultimate performance of broadband multifeed systems. We show that this bandwidth gap is largely independent of the formed beam angle, number of array elements, array layout, and element radiation patterns. We use simulation and modeling to study the origins and nature of this physical effect and develop an upper bound on the sensitivity bandwidth of a high-efficiency array feed, and consider several possible methods for improving the efficiency of multifeed systems in the bandwidth gap.

5.1 Introduction

Hight sensitivity receivers for reflector antennas have been widely developed for remote sensing, radio astronomy, and satellite communications. Detecting extremely weak signals from deep-space radio sources and attaining high SNR with small diameter terrestrial dish antennas require highly sensitive receiver electronics and feed systems that achieve high aperture efficiency. Notable large-scale astronomical instruments include the 100 meter Green Bank Telescope (GBT) [7,8], 305 meter Arecibo Telescope [9,10], the Chinese Five-hundred meter Aperture Spherical Telescope (FAST) currently under construction [11,12], and the proposed international Square Kilometre Array (SKA) [13,14].

Considerable work has been done in recent years to create multi-feed systems for reflector antennas that achieve performance competitive with traditional single-pixel horn-type feeds [2,15,16]. For astronomical applications, the key figure of merit is survey speed, or the time required to map a region of the sky to a given source flux density. Survey speed is proportional to the frequency bandwidth, the field of view or observable region of the sky, and the squared sensitivity, where sensitivity is related to reflector aperture efficiency and system noise temperature [17]. In terms of achieving higher survey speed for large reflector antennas, single-pixel feeds are a mature technology, with most recent research focusing on achieving ultrawideband operation [18–21].

As sensitivity and bandwidth for single-pixel feeds are nearing practical limits and fundamental physical bounds, the only remaining factor in the receiver survey speed with room for substantial improvement is the field of view. Two basic technologies are available for wide-field or multipixel receivers. The first approach is a cluster of single feeds, each feed of which produces a beam to match the reflector antenna [22–24]. Cluster feeds are used for astronomical applications as well as satellite terminals that communicate with 3-5 satellites simultaneously. The disadvantage is that the individual feeds in the cluster are electrically large and cannot be spaced closely enough to fully sample the reflector antenna field of view, and beams on the sky are separated by unobservable regions that must be covered by mechanically raster-scanning the reflector [25].

A second approach to achieving wide-field operation is a phased array feed (PAF). A PAF consists of electrically small elements that fully sample a contiguous field of view by combining the array outputs with beamformer coefficients to produce high quality illumination pattern for multiple overlapping pixels on the sky. Research efforts are underway around the world to improve the efficiency and system noise temperature of PAF systems to the point that they are comparable in sensitivity to single feeds and cluster feeds [26–29].

Both approaches to wide-field imaging are receiving significant attention in the astronomical community. Cluster feeds are now in routine use, and PAFs have been demonstrated as prototypes on large reflectors [30, 31]. The basic theory and techniques for analysis of array feeds are well understood [32–36]. Development challenges for PAFs that are currently under study including noise temperature minimization, high-throughput, multichannel real time digital signal processing hardware, and deployment of fully operational PAF systems.

While PAFs have demonstrated improvements in field of view over existing receiver technologies, the relative bandwidth of existing PAF systems is smaller than that of state-of-the-art ultrawideband single-pixel feeds. For a wideband array feed, the weighting of elements in the array changes qualitatively over the operating bandwidth. As the system operating bandwidth of an array feed increases, the spacing between elements becomes electrically large at the high end of the band, and the formed beams degenerate to independent, single-element beams similar to that of a cluster feed. At very high frequencies, the array feed elements become electrically large enough to realize high aperture efficiency illumination patterns. For a broadband multifeed system, that is between the low-frequency or "PAF" regime and the high frequency cluster feed regime, the analysis presented in this paper shows that there is a bandwidth gap in which the elements are too far apart to operate in concert to create high quality illumination pattern, but too small to individually illuminate the reflector efficiently.

To study this effect and its implications for optimal design of multifeed systems, we use models for arrays with various configurations to extract the intrinsic parameters of the bandwidth gap between the PAF and cluster feed regimes that are independent of the array layout and element design. Aperture efficiency for a broadband array feed is poor when the array element spacing is equal to the distance between the center and the first null of the Airy pattern that governs the field distribution in the reflector focal plane. A relationship is found between the array element spacing in wavelength corresponding to the critical frequency that divides these regimes and the reflector focal length to diameter ratio (f/D), and the behaviors of the spillover efficiency and focal plane field distribution in the bandwidth gap are used to provide insight into the physics of this effect. Methods for mitigating poor aperture efficiency in the transition region are explored, design guidelines are obtained for a given reflector f/D for wideband array feeds, and a physical sensitivity bandwidth limit bound is proposed for high-efficiency array feeds.

5.2 Model and Analysis

5.2.1 Feed Model

A schematic describing a transmitting array feed model is shown in Fig. 5.1. The feed system is modeled as a collection of antennas with embedded element patterns $\overline{E}_n$ ($n = 1, 2, \ldots, N$), which represents the far electric field with input current I_0 into the port of the nth array element and all other elements open circuited. The embedded element patterns can be modeled using a full-wave numerical method, but to speed up sweeps over key feed parameters, we approximate the embedded element patterns by the isolated antenna pattern for each element. We have extensively validated this approximation by comparison to full wave simulations with the finite element method (FEM).

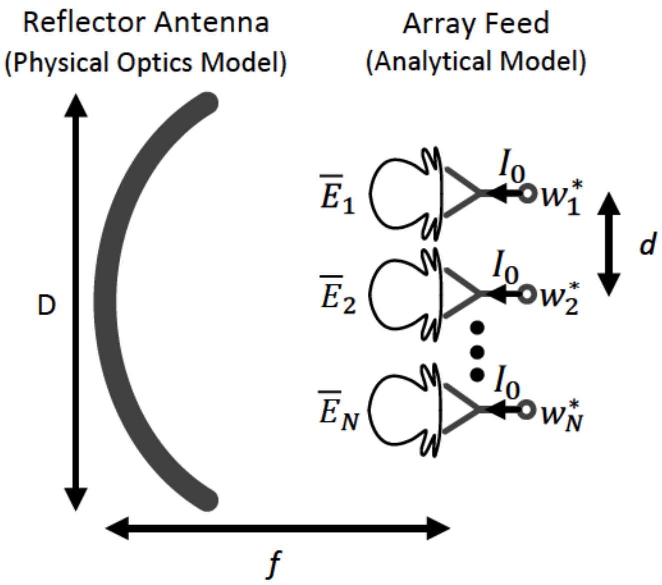

Figure 5.1: Schematic describing the array feed model.

To account for the first order mutual coupling between elements, we use the element radiation pattern overlap integral formulation [37]. That only considers the far field pattern, so no information about the effect of near field interaction between each element is included. In this treatment, an overbar denotes a three-dimensional field vector, and bold font indicates an N-element vector with one value for each array element. All fields are phasors relative to $e^{j\omega t}$ and the superscript H represents the Hermitian conjugate. The total radiated electric field from the array feed is

$$\overline{E}(\bar{r}) = \frac{1}{I_0} \sum_{n=1}^{N} w_n^* \overline{E}_n(\bar{r}) \tag{5.1}$$

To achieve the maximum aperture efficiency, the optimal beamformer weights can be shown to be

$$\mathbf{w} = \mathbf{A}^{-1}\mathbf{E}_R(\bar{r}) \tag{5.2}$$

where the column vector $\mathbf{E}_R(\bar{r})$ has elements $\hat{p} \cdot \overline{E}_{Rn}(\bar{r})$ and the unit vector $\hat{p}$ represents the polarization of the secondary beam. For an array with large element spacing, coupling between elements is small, and $\mathbf{A}$ is a strongly diagonal matrix. In the case of no coupling between elements, Eq. (5.2) becomes the conjugate field matching (CFM) solution. For a cluster feed, the radiated field in the direction $\hat{r}$ is strongly dominated by one feed in the cluster, and both $\mathbf{E}_R(\bar{r})$ and $\mathbf{w}$ are proportional to an elementary vector with one nonzero element.

When the array feed operates in the receiving mode, in view of the electromagnetic reciprocity principle, the CFM beamformer $\mathbf{w} = \mathbf{E}_R(\bar{r})$ matches beamformer weights to the complex amplitude of the electric field in the plane of the array feed sampled at the array element positions. For a paraboloidal reflector, the field distribution in the focal plane is an Airy pattern. Since the Airy pattern is approximately circularly symmetric for a linearly polarized wave incident on the reflector from the boresight direction [38], we only consider symmetric array layouts here.

To validate this model for the aperture efficiency of a reflector with an array feed system, we compare the model to full wave simulations with the finite element method (HFSS, Ansys, Inc.) for the array feed. Fig. 5.2 shows a comparison of reflector aperture efficiency over frequency for a 3×3 array feed with full-wave and analytical models. The array element is a traditional pyramidal horn antenna with TE_{10}-mode aperture field distribution. Ripples of the aperture efficiency with the full-wave model are due to the excited surface waves and the near field interaction between the array elements. The array feed analytical model agrees well with the full wave model, validating the use of the analytical model for embedded element patterns in the following studies.

5.2.2 Bandwidth Gap Using a Hexagonal Array Model

Based on the above modeling approach, a four-ring (61-element) hexagonal array of circular horn elements feeding a reflector is analyzed. The element aperture field distribution is uniform, and the element spacing d is equal to the element diameter. Fig. 5.3a shows a comparison of aper-

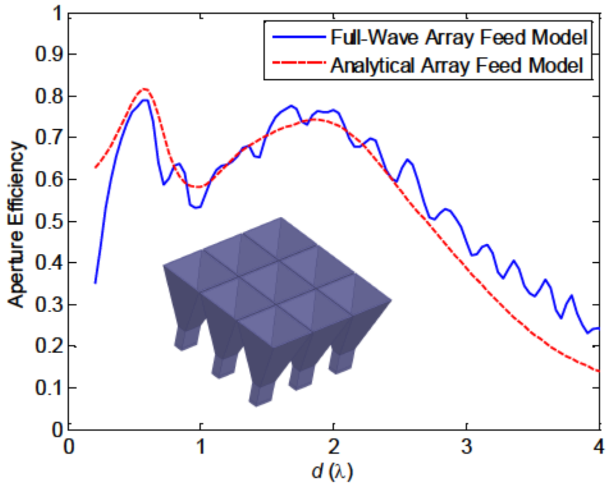

(a) Reflector $f/D = 1$.

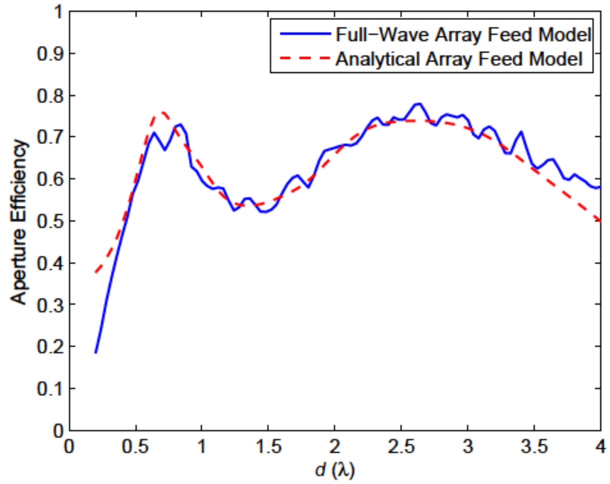

(b) Reflector $f/D = 1.5$.

Figure 5.2: Comparison of aperture efficiency over frequency with a full-wave FEM simulation and a simple, analytical model for element patterns. The antenna is a 3×3 TE_{10}-horn array feed.

ture efficiency for different reflector geometries over element spacing with a formed beam in the boresight direction. For a given reflector f/D, the aperture efficiency behaves as a "saddle" shape that represents a decrease of aperture efficiency between the low and high frequency operating regimes. The element spacing d_0 corresponding to the center of this operating bandwidth gap (marked with square dots in Fig. 5.3a) increases with f/D.

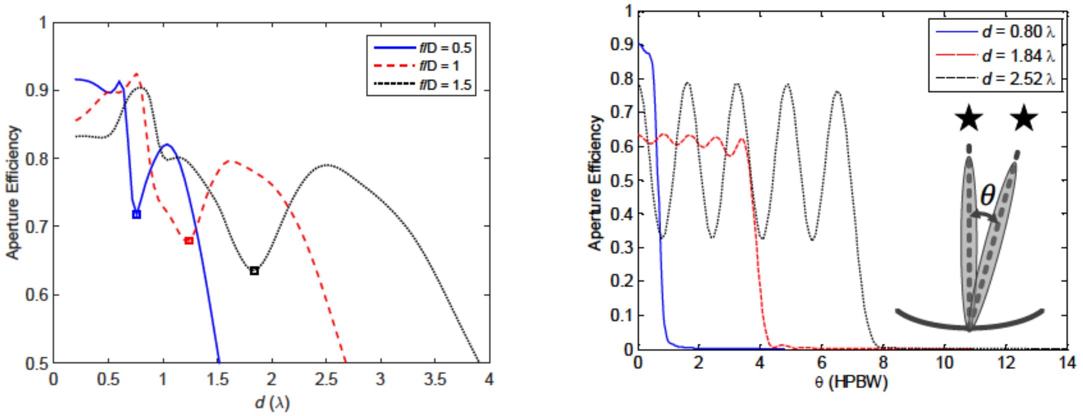

(a) Boresight beam for a 4-ring array feed over different f/D.

(b) Steered beam for a 4-ring array feed when reflector $f/D = 1.5$.

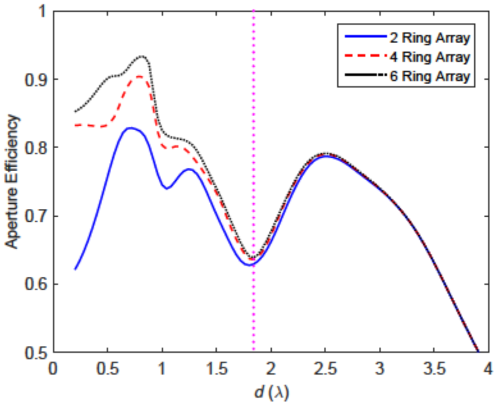

(c) Boresight beam when reflector $f/D = 1.5$.

Figure 5.3: Modeled aperture efficiency over frequency for a hexagonal array feed with different values of the reflector f/D, beam steering angle, and array size. The aperture field distribution for the horn array elements is uniform.

Fig. 5.3b shows the aperture efficiency for a steered beam with element spacings 0.8 λ, 1.84 λ, and 1.52 λ. These values correspond respectively to the peak aperture efficiency in the PAF regime, the gap between operating modes, and the peak of the higher frequency cluster feed regime with reflector f/D is 1.5. Within the field of view, the aperture efficiency for spacing 1.84 λ is always lower than that for 0.8 λ. When d is 2.52 λ, the large element spacing undersamples the focal plane field distribution and ripples appear in the aperture efficiency distribution over beam steering angle. When the peak of the focal plane field distribution is located between two neighboring elements, the Airy pattern is poorly sampled and aperture efficiency decreases. Fig. 5.3c shows that if the array size is increased from two rings to six, the position and values of the bandwidth gap between regimes remains fixed, indicating that the critical electrical spacing d_0 is largely independent of array size.

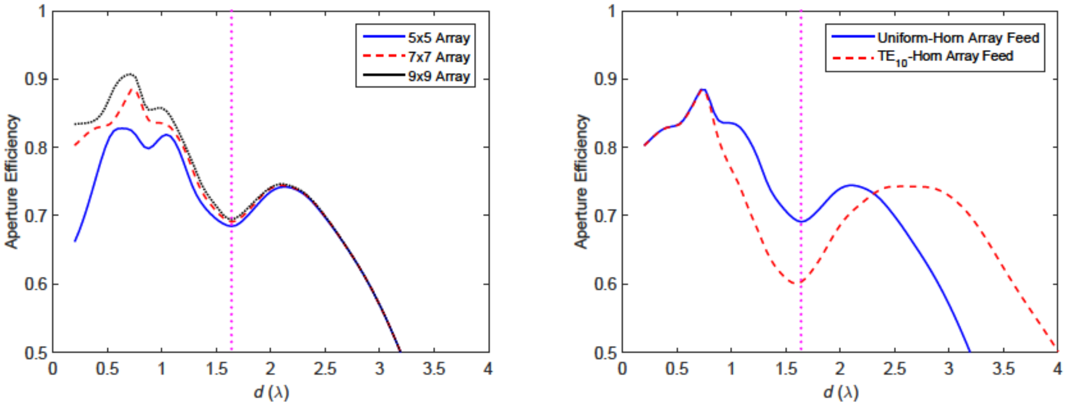

(a) Uniform-horn array feed.

(b) 7×7 uniform-horn and TE_{10}-horn array feed.

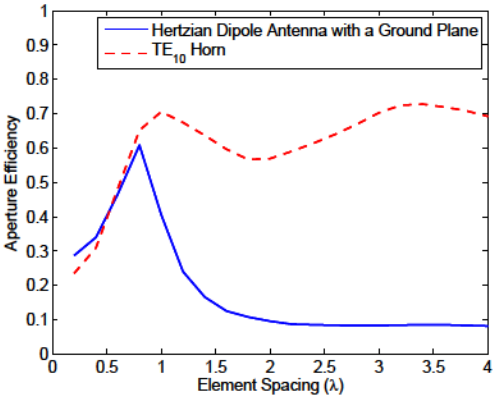

(c) Comparison between Hertzian dipole and horn element when reflector f/D equals to 2.

Figure 5.4: Aperture efficiency over frequency for a rectangular array feed with different array sizes and element aperture field distributions with reflector f/D of 1.5. Two horn element aperture field distributions are considered, uniform and the TE_{10} mode.

To study the wideband aperture efficiency behavior of an array feed with a different element layout, a rectangular array feed with a square horn antenna element is used as a second comparison case. The aperture field on the square horn elements is uniformly distributed and the element spacing is equal to the element side length. Fig. 5.4a shows the aperture efficiency of a rectangular array feed over frequency with different element numbers when the reflector f/D is 1.5. As with the hexagonal array feed, d_0 is invariant with respect to the size of the array feed. When the aperture field distribution of the square horn array element is changed from the uniform distribution to the TE_{10}-mode distribution, as shown in Fig. 5.4b, the critical spacing between regimes remains fixed.

From these results, it appears that for a multifeed system, the critical element spacing between the low frequency array feed regime and the high frequency cluster feed regime at which neither operating mode can achieve high efficiency is largely independent of the number of array elements, beam steering angle, array layout, and element radiation pattern, and is primarily controlled by the reflector geometry (f/D). We now turn to a more detailed analysis that provides insight into the underlying cause of this bandwidth gap.

5.3 Spillover and Focal Field Behavior for Broadband Multifeed Systems

5.3.1 Subefficiencies in the Array Feed and Cluster Feed Regimes

To understand the behavior of the efficiency of a broadband multifeed system over frequency, subefficiencies can be used to attribute changes in performance to specific physical mechanisms. Aperture efficiency can be factored as

$$\eta_{\mathrm{ap}} = \eta_{\mathrm{sp}}\eta_{\mathrm{t}}\eta_{\mathrm{p}} \tag{5.3}$$

where η_{sp} is spillover efficiency, which measures the amount of radiated power from feed reflected by the reflector, η_{t} is taper efficiency, which describes the uniformity of the amplitude distribution of the feed radiation pattern over the surface of the reflector, and η_{p} is the phase efficiency that represents the deviation of the phase of the illumination pattern from ideal over the aperture plane. Polarization efficiency, blockage efficiency and reflector surface error efficiency are ignored in the analysis, as they are not relevant to understanding the mechanisms that drive the operating regimes of the feed system over frequency. Formulas used to calculate each subefficiencies can be found in [39].

For a 4-ring hexagonal array feed with uniform aperture field distribution, a comparison of subefficiencies distribution over frequencies is shown in Fig. 5.5. The results show that the aperture efficiency signature associated with the gap between operating regimes is dominated by a decrease in spillover efficiency, indicating energy loss due to overillumination of the reflector.

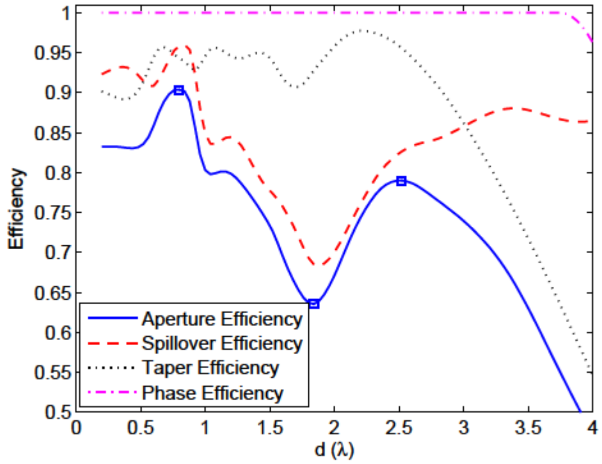

Figure 5.5: Aperture, spillover, taper and phase efficiency for a 4-ring hexagonal array feed with reflector $f/D = 1.5$ and beam steered to the boresight direction.

To confirm this, Fig. 5.6 shows the formed array feed illumination pattern and the corresponding beamforming weights of each ring element, where the selected frequencies correspond to the first peak, the minimum, and the second peak of the aperture efficiency distribution in Fig. 5.5 respectively. The reflector rim angle is marked at 18.9°. As shown in Fig. 5.6a, when the electrical element spacing is 0.8 λ and 2.52 λ, radiated power from the beamformed feed pattern is concentrated within the rim angle of reflector antenna.

When d is 2.52 λ, the array element is electrically large enough to form a narrow beam to fully illuminate the reflector antenna, so the beam is dominated by the center element. When d is 0.8 λ, only using the center element is not enough to form a narrow beam to illuminate the reflector antenna, so more elements are needed in the beamformer to form a high quality illumination pattern. At the critical frequency ($d = 1.84\lambda$), the center element is also electrically small. The beamformer weights for 1.84 λ are similar to that for 2.52λ and are dominated by the center element as well, but at that frequency, one element fails to form a narrow enough beam to illuminate the reflector antenna. Consequently, the spillover efficiency decreases, and the overall aperture efficiency exhibits a minimum at the critical frequency.

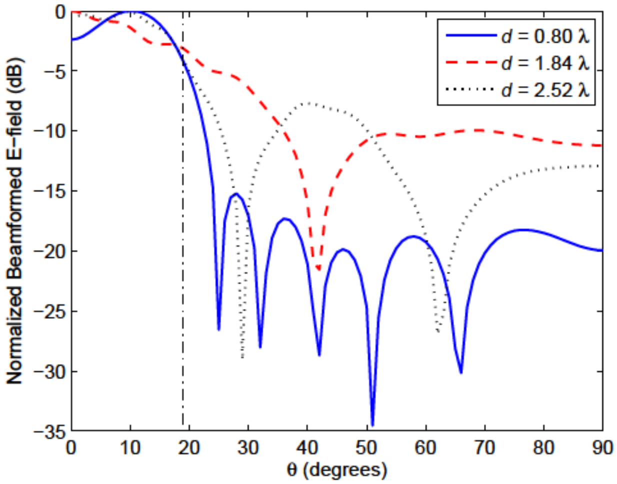

(a) Formed array feed illumination pattern using beamformer. The reflector rim angle is marked at 18.9°.

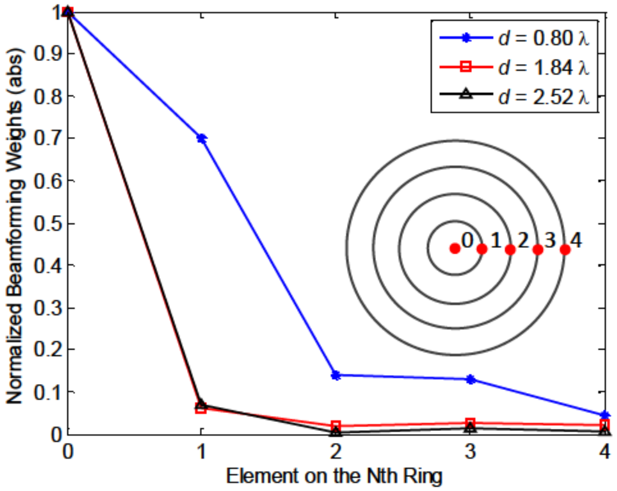

(b) Beamformer weights by array ring index.

Figure 5.6: A comparison of the beamformed radiation pattern and the corresponding beamformer weights for a 4-ring hexagonal array feed. The element spacings correspond to the first peak, the minimum, and the second peak of aperture efficiency over frequency in Fig. 5.5

5.3.2 Focal Plane Field Distribution Over Frequency

We have considered the performance gap between the array feed and cluster feed regimes in terms of the illumination pattern of the feed on the reflector, which is essentially a transmitting mode analysis. For the receiving mode, this effect can be analyzed in terms of the field distribution in the plane of the array feed over frequency. While the transmit analysis links the aperture efficiency decrease to well-known parameters of reflector-feed systems, the receiving analysis provides more direct insight into how this effect is related to the array feed geometry and configuration.

The focal plane field distribution for a paraboloidal reflector is a so-called Airy pattern. For the array examples considered above, the critical frequency occurs when the first null of the Airy pattern overlaps with the center point of the neighboring element nearest to the center element of the array feed. This is illustrated in Fig. 5.7. At this frequency, the array element spacing d is equal to the distance W from the center to the first null of Airy pattern. The beamformer weights as shown in Fig. 5.6b for the first ring elements are close to zero, which prevents the array from fully sampling the Airy pattern and capturing all of the energy focused by the reflector in the plane of the feed.

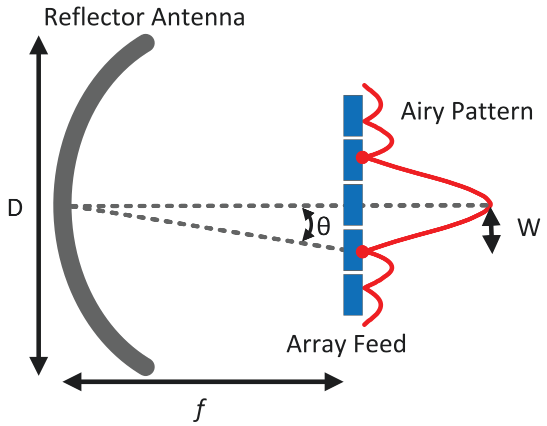

Figure 5.7: Aperture efficiency over frequency is minimized when the first null of the Airy pattern overlaps with the centers of the nearest neighbor array feed elements.

The position of the first null of Airy pattern is

$$\sin\theta = 1.22\frac{\lambda}{D} \tag{5.4}$$

where θ is the angle between the axis of the reflector antenna and the first null of Airy pattern. Since θ is very small, the offset position of the null in the focal plane can be approximated as

$$\tan\theta = \frac{W}{f} = 1.22\frac{\lambda}{D} \tag{5.5}$$

Thus, with a simple one-dimensional array feed analysis, the critical element spacing d_0 is

$$d_0/\lambda = W/\lambda = 1.22 f/D. \tag{5.6}$$

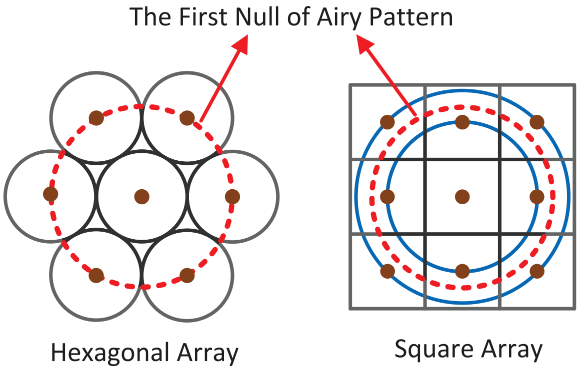

Figure 5.8: Position of the first null of the focal plane Airy pattern for a hexagonal array feed and rectangular array feed at the critical frequency.

For a two-dimensional array feed, the relationship between the Airy pattern null and element locations at the critical electrical spacing is similar to the 1D case, as illustrated by Fig. 5.8. For a hexagonal array feed, the center points of the first ring elements coincide with the first null of the Airy pattern, so the expected relationship between d_0 in wavelengths and reflector f/D is 1.22, which is same as the value in Eq. (5.6). For the rectangular array, at the critical frequency, the first null of Airy pattern lies between the two circles marked in the figure. The expected value of d_0/λ for this layout is between $1.22/\sqrt{2}f/D$ and $1.22\,f/D$.

5.3.3 Comparison of Theoretical and Calculated Results

Aperture efficiency can be modeled over element spacing and the reflector f/D to verify the relationship in Eq. (5.6). Using the array feed model of the previous section, Fig. 5.9 shows a nearly linearly relationship between the critical spacing d_0 and the reflector f/D for a hexagonal and rectangular array feed. The slope of the curve can be calculated by the average ratio of d_0 to the reflector f/D. Fig. 5.10 shows the calculated and predicted ratio of d_0 to the reflector f/D over array size for both layouts.

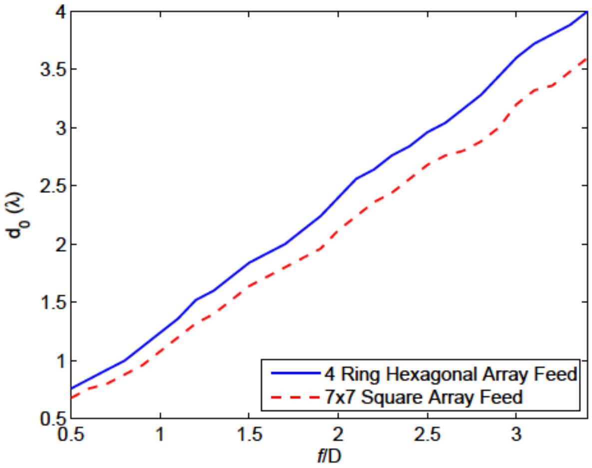

Figure 5.9: Calculated relationship between d_0 (λ) and reflector f/D for a 4 ring hexagonal and 7×7 rectangular array feed.

For a hexagonal array feed, the slope converges to 1.21, which is very close to the predicted value of 1.22. For a hexagonal array feed, the relationship between d_0 and the reflector f/D is therefore

$$d_0/\lambda = 1.21 f/D. \tag{5.7}$$

For a rectangular array feed, the relationship is

$$d_0/\lambda = 1.07 f/D. \tag{5.8}$$

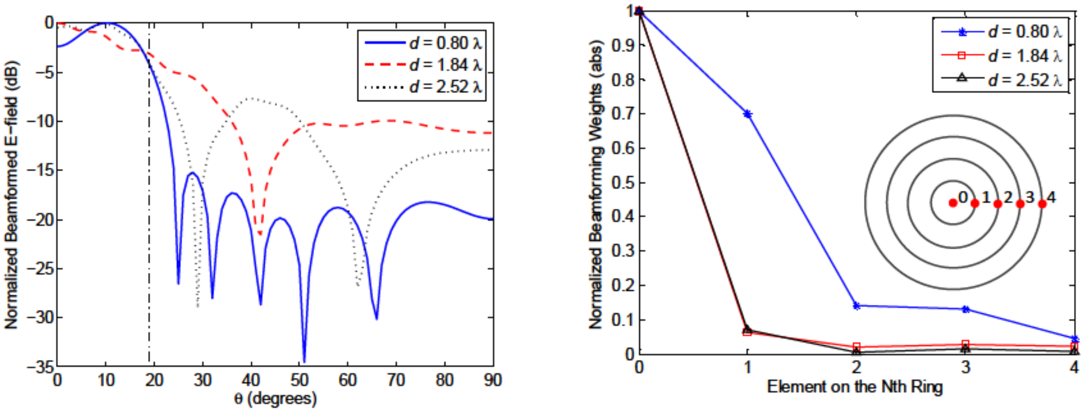

(a) Hexagonal array feed.

(b) Rectangular array feed.

Figure 5.10: A comparison of the calculated and theoretical ratio of d_0 (λ) to the reflector f/D.

In Fig. 5.6b, the beamforming weights for d with 0.8 λ are non-negligible for the near center elements, so this case is in the phased array feed regime. The beamforming weights for $d = 2.52\ \lambda$ is dominated by the center element and other elements do not contribute significantly, so the system behaves as a cluster feed. Therefore, we consider d_0 as the boundary between the array feed and cluster feed regimes.

5.3.4 Improving Efficiency in the Bandwidth Gap

Aperture efficiency at the critical frequency between the array feed and cluster feed regimes is significantly lower than the peak value. The maximum value of aperture efficiency in Fig. 5.5 is 91%, whereas the minimum value is 64%, which is a serious degradation in performance for satellite communications, remote sensing, and particularly radio astronomy applications. For a broad bandwidth phased array feed system, the optimal center frequency might not fall into the frequency bandwidth gap. But the upper frequency driven by application requirements may fall in this region. Meanwhile, at W-band or even higher frequencies, the smallest array element spacing is limited by the cross section size of a receiver element and associated electronics [40]. In this section, two methods will be suggested for improving performance near the critical frequency.

Optimization of Array Layout

From a comparison between Fig. 5.3c and Fig. 5.4a, the minimum aperture efficiency for a rectangular array feed is $\sim$5% higher than that for a hexagonal array feed. The reason is because the aperture efficiency decrease requires an overlap between the first null of Airy pattern and the center points of the near center elements. As shown in Fig. 5.8, a hexagonal array feed satisfies this requirement perfectly, but for the rectangular array feed, the elements are not completely aligned with the null. The four neighbored center elements and the four corner elements are inside and outside the ring of the first null of Airy pattern respectively. To best match the Airy pattern and achieve the maximum gain, the beamformer weight of the center element is in phase with the four neighbored center elements and out of phase with the four corner elements. Therefore, compared to a hexagonal array feed, the phase distribution of beamforming weights for the near center elements of a rectangular array feed can be better matched to the the first null of the Airy pattern, which improves the performance of the rectangular array and leads to a higher aperture efficiency. The improvement is modest, however, and better approaches are desirable.

Superdirective Elements

The primary reason for the aperture efficiency decrease is that when the beamformer weights of the other elements are close to zero, the effective receiving area of the center element is too small to fully sample the main lobe of Airy pattern. While mainly of theoretical rather than practical interest, we wish to determine if superdirective elements can be used to solve this problem. Fig. 5.11 shows the aperture efficiency at the critical frequency of a 4-ring hexagonal array feed over a ratio of the element effective length to the element physical length. It can be seen that when the aperture field is uniformly distributed on each element, $L_{\text{eff}}/L_{\text{phy}}$ becomes unity and the aperture efficiency is 64%. When $L_{\text{eff}}/L_{\text{phy}}$ is larger than 1, the antenna element behaves as a superdirective antenna and the main lobe of the Airy pattern is better sampled. When the ratio becomes 1.4, the aperture efficiency is maximized at 79%. Further increasing $L_{\text{eff}}/L_{\text{phy}}$ makes the feed pattern too narrow to illuminate the reflector antenna and leads to a decrease of the aperture efficiency.

Although the superdirective array feed shows a better performance at d_0 (λ) than a uniform array feed, practical issues including gain reduction due to large ohmic losses, narrow bandwidth,

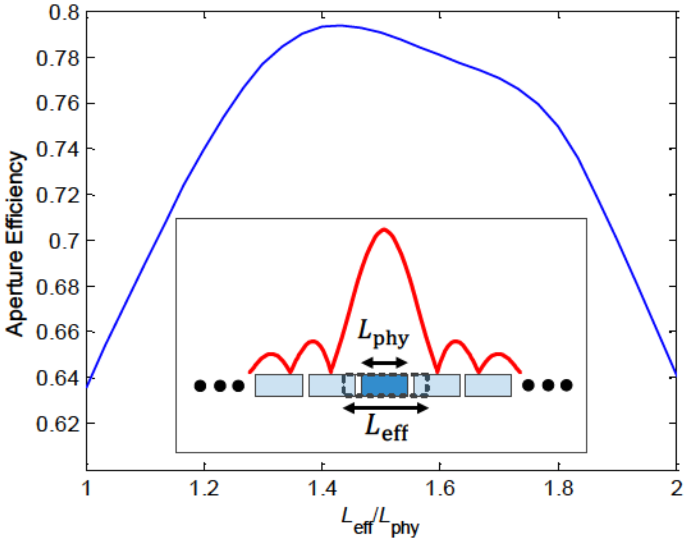

Figure 5.11: Aperture efficiency at the critical frequency of a 4-ring hexagonal array feed at the reflector boresight direction over a ratio of the element effective length (diameter of circular horn antenna element) to the element physical length.

and high accuracy requirements for the element aperture field distribution make the superdirective approach difficult to implement [41–43]. The study of superdirective elements is of interest as it represents a method for changing the characteristics of elements in the array in a systematic way to improve performance of the multifeed system in the bandwidth gap. There may be other more practical element designs that do not rely on superdirectivity, but still improve efficiency over the full operating frequency range of a broadband feed.

5.3.5 Physical Bandwidth Limit for a High-Efficiency Array Feed

For conventional array elements that do not compensate for poor aperture efficiency near the critical frequency, there is an inherent bandwidth limit for a high-efficiency focal plane array feed. The focal field distribution in relation to the array elements at the upper and lower band edges are illustrated in Fig. 5.12. Since the curve of aperture efficiency distribution over frequency behaves as a saddle shape, the effect of aperture efficiency decrease limits the maximum frequency

$f_{\max}$ of a high-efficiency array feed:

$$\frac{d}{\lambda_{\min}} = 1.22f/\mathrm{D} \tag{5.9}$$

The upper frequency limit is

$$f_{\max} = 1.22\frac{c}{d}f/\mathrm{D}, \tag{5.10}$$

where c is the speed of light.

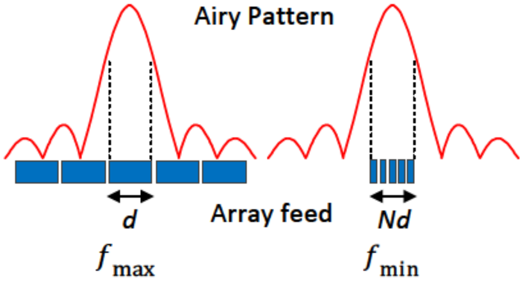

Figure 5.12: Illustration of high and low frequencies limits for a focal plane array feed.

As the frequency is decreased, the Airy pattern becomes wider. When the array feed size is too small to sample the main lobe of Airy pattern, the aperture efficiency will again decrease. The overall array size limits the minimum frequency $f_{\min}$ of the array feed according to

$$\frac{Nd}{\lambda_{\max}} = 1.22f/\mathrm{D}, \tag{5.11}$$

The minimum operating frequency is

$$f_{\min} = 1.22\frac{C}{Nd}f/\mathrm{D} \tag{5.12}$$

where N is the element number of a one dimensional array feed.

The relative bandwidth limit for the high aperture efficiency regime of a one-dimensional array feed is therefore

$$B = \frac{f_{\max} - f_{\min}}{(f_{\max} + f_{\min})/2} = 2 - \frac{4}{N+1} \tag{5.13}$$

where $N > 1$. If we expand the one dimensional array feed to a hexagonal or rectangular array feed, the bandwidth limit becomes

$$B = 2 - \frac{2}{N_{\text{ring}} + 1} \tag{5.14}$$

where $N_{\text{ring}} > 0$ and represents the number of element rings in the array. The relationship between the bandwidth limit and the array element number for the hexagonal and square array feed is shown in Fig. 5.13.

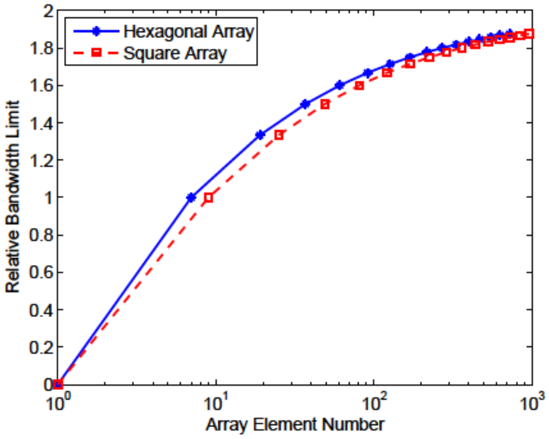

Figure 5.13: Fundamental bandwidth limit for a phased array feed from Eq. 5.14. For a hexagonal array feed, there are $1 + 3N_{\text{ring}}(N_{\text{ring}} + 1)$ elements, and $(2N_{\text{ring}} + 1)^2$ for a square array feed.

The achievable high-efficiency bandwidth of an array feed increases with array size, but approaches a relative bandwidth of two as the number of elements in one dimension becomes large. The increase in bandwidth is reflected in Fig. 5.3c and 5.4a, where the aperture efficiency is seen to be fixed at the critical spacing d_0, whereas for smaller spacing the aperture efficiency increases with array size.

This bandwidth limit can not be applied to nonconventional or superdirective antenna elements. Because the effective array area of a superdirective antenna is larger than Nd, which makes the array feed better sample the main lobe of Airy pattern, the minimum frequency limit becomes smaller and the bandwidth is larger.

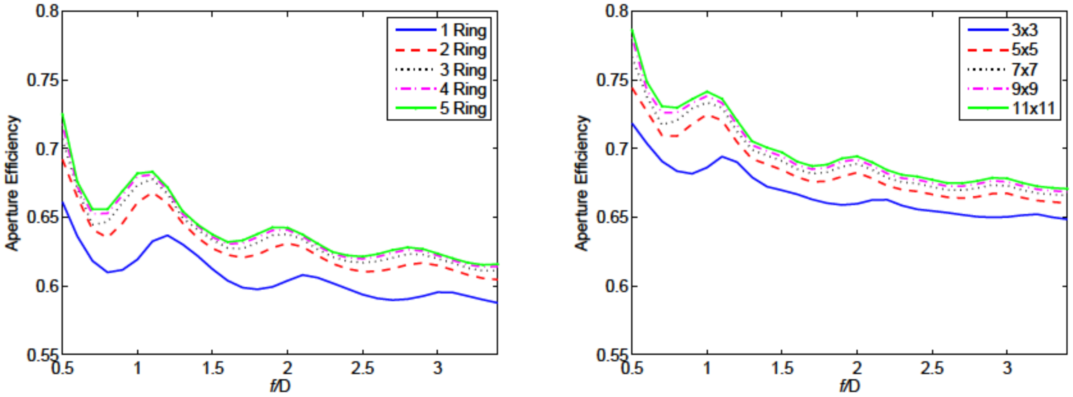

(a) Hexagonal array feed.

(b) Rectangular array feed.

Figure 5.14: Aperture efficiency at the critical frequency for different array sizes over reflector f/D.

The appropriate choice of the aperture efficiency threshold used to define a "high-efficiency" array feed can be determined using the array feed model of the previous section. Fig. 5.14 shows that the aperture efficiency at the critical frequency is roughly 60% for a uniform hexagonal array feed and 65% for a uniform rectangular array feed over a wide range of reflector geometries. Thus, the high-efficiency operating bandwidth for a hexagonal array feed can be approximately defined as above 60%. Similarly, for a high-efficiency rectangular array feed the threshold is 65%. These are modeled efficiencies that do not include blockage, feed support scattering, or other non-ideal effects, so the practical expected efficiency thresholds would be slightly lower.

It is interesting to compare this bandwidth bound to the Wheeler-Chu limit for the impedance bandwidth of a single antenna [1]. Since the definition of aperture efficiency is based on available power, aperture efficiency is independent of the impedance match between the antenna and load, and is only influenced by the element radiation pattern. Thus, the aperture efficiency bandwidth limit can be considered as a formed radiation pattern bandwidth limit for array feeds. Impedance mismatch between the antennas and LNAs increases the system noise temperature. The sensitivity for an array feed system is proportional to the ratio of the reflector aperture efficiency to the system noise temperature, which means that the variation of aperture efficiency in the bandwidth gap is also reflected in the receiver sensitivity and signal to noise ratio. Hence, the sensitivity bandwidth limit of a high-sensitivity array feed is an approximate intersection of the impedance bandwidth limit and the formed radiation pattern bandwidth limit.

5.4 Summary

For multifeed systems, we have shown that there is a bandwidth gap between array feed and cluster feed operating regimes that occurs at a critical frequency such that the element spacing in wavelengths is roughly $1.22\ f/D$. Aperture efficiency is poor near this frequency due to increased spillover loss and the coincidence of the null in the focal field distribution with array element locations. Optimization of array layout and modification of the element patterns can improve the aperture efficiency near the critical frequency to some extent.

For phased array feeds, a formed radiation pattern bandwidth limit for array feeds is proposed that can be combined with the Wheeler-Chu impedance bandwidth limit to confine the performance bandwidth of a high-efficiency array feed with conventional array elements. In future work, it would be of interest to find practical element designs that eliminate the reduction in multifeed system performance near the critical frequency.

CHAPTER 6. ANTENNA LOSS AND RECEIVING EFFICIENCY FOR MUTUALLY COUPLED ARRAY ANTENNAS

For phased arrays used in satellite communications and radio astronomy, high sensitivity is required, and minimizing antenna losses is critical. Losses for single antennas can be minimized by using high conductivity materials. It is less well understood that loss for array antennas is also influenced by mutual coupling between array elements and the beamformer weights applied to the signal from each element. In this paper, we study the antenna loss and receiving efficiency for phased array antennas and focal plane phased array feeds. To better elucidate the physics of array antenna loss related to mutual coupling and beamformer weights, losses for a coupled array can be lumped into an array effective resistance similar to the loss resistance of an equivalent single antenna. Numerical results show that although the antenna loss for a single isolated array element is low, the array antenna loss can be significantly increased by mutual coupling, particularly for beams with a large scan angle.

6.1 Introduction

The key figure of merit for active receiving arrays for satellite communications and radio astronomy observations is the sensitivity (G/T_{sys}). Sensitivity is directly proportional to signal to noise ratio (SNR). Depending on the application, receiving arrays with high sensitivity allow for a long communication range, a low transmitter power usage, or a high image quality for observed radio astronomical sources [44]. Many techniques for improving gain and reducing system noise temperature for receiving arrays have been explored, such as improving antenna designs [16, 20, 45–47] and developing low noise electronics [48, 49].

For phased arrays to be competitive with traditional receivers in high sensitivity applications, reducing antenna loss is critical [50]. The system noise budget for an active receiving array system includes noise from cold sky, warm ground, antennas loss and LNAs [34]. For terrestrial communications, the thermal noise environment leads to a noise floor near ambient temperatures ($\sim$290 K), and improving antenna efficiency leads to only a modest SNR improvement. For satellite communications and radio astronomy observations, however, the sky noise temperature is 4-5 K at L-band and 10 K at Ku band [51]. A state-of-the-art single-antenna radio telescope receiver achieves a system noise temperature at L-band of less than 20 K. When noise budget contributions from sky noise and receiver electronics are small, an increase in added noise due to antenna loss leads to a large degradation in system performance.

For a single antenna, loss is caused by dielectrics and conductors in the structure. Loss is exacerbated by the roughness of metal surfaces and by concentrated currents near the antenna feed point. Using high conductivity metals and low dielectric loss materials and evenly distributing currents can improve radiation efficiency.

These considerations certainly apply to array antennas, but for multiport antenna systems, antenna loss and efficiency are also influenced by mutual coupling. Because loss and efficiency depend on beamformer coefficients and beam scan angle, for an array these figures of merit are no longer an intrinsic property of the antenna. The goal of this paper is to provide a better understanding of mutual coupling and beamformer coefficients on the efficiency of high sensitivity receiving array antennas.

For active receiving arrays, the effect of ohmic and dielectric losses on system performance can be characterized using receiving efficiency [52]. For a single antenna, the ratio of radiated power to input power when the antenna is operating as a transmitter can be used directly to determine the increase in antenna noise temperature due to losses when the antenna is operated as a receiver. For a complex, active receiving array, it is challenging to determine a meaningful equivalent to radiated power and input power, because the antenna system includes nonreciprocal components. Instead, loss effects are parameterized using the ratio of the external antenna noise at the output of the receiver to the sum of the external antenna noise and the noise due to losses in the antenna. No matter how complex the system, this quantity is well defined for active array receivers. By convention, the external noise distribution is assumed have a brightness temperature distribution that is isotropic with respect to angle, and the antenna is assumed to be in thermal equilibrium with the environment. For a reciprocal antenna, the receiving efficiency is equal to the radiation efficiency.

Receiving efficiency for a broadband thickened dipole array antenna is analyzed using a full-wave model. The target application for the antenna system is a phased array feed for a large reflector, and beamformer coefficients depend on the geometry of the reflector. The effect of beamforming and mutual coupling on antenna loss are consolidated for convenience into an effective resistance. Receiving efficiency and effective resistance are compared for an isolated single dipole antenna, an embedded single element in the array, and for a formed beam that combines signals from multiple elements. The influence on loss of different beamforming algorithms is analyzed. For an array feed, the antenna noise contribution due to losses is calculated over the ratio of focal length to diameter (*f/D*). These simulation studies provide insight into the role of mutual coupling in influencing antenna losses for high sensitivity phased array applications.

6.2 Analysis Methods

6.2.1 Receiving Efficiency for Active Antennas

To study loss in active receiving arrays, we use the isotropic noise response and receiving efficiency defined in IEEE standard for definitions of terms for antennas [35]. The isotropic noise response is the output noise power for a given formed beam due to external noise sources and antenna loss for receiving active antennas with noiseless LNAs and receivers in an environment with brightness temperature distribution that is independent of direction and in thermal equilibrium with the antenna, per unit bandwidth and at a specified frequency. Receiving efficiency is defined as the ratio of the isotropic noise response with noiseless antenna to the isotropic noise response. For a passive, reciprocal antenna, receiving efficiency is equal to the radiation efficiency of the antenna. In this section, isotropic noise response and receiving efficiency are used to analyze the antenna noise temperature for a single and active receiving array antennas.

Single Antenna

The definition of isotropic noise response for a single active receiving antenna with a noiseless LNA and receiver in a thermal environment with $T_{\mathrm{iso}} = 290\,\mathrm{K}$ brightness temperature is illustrated in Fig. 6.1a. Receiving efficiency is calculated from the ratio of the antenna external isotropic noise response $P_{\text{iso,ext}}$ with noiseless antennas to the isotropic noise response P_{iso} including antenna loss, so that

$$\begin{aligned}\eta_{\text{rec}} &= \frac{P_{\text{iso,ext}}}{P_{\text{iso}}} && (6.1)\\ &= \frac{P_{\text{iso,ext}}}{P_{\text{iso,ext}} + P_{\text{loss}}}, && (6.2)\end{aligned}$$

where P_{loss} is the noise power at the beam output due to antenna loss.

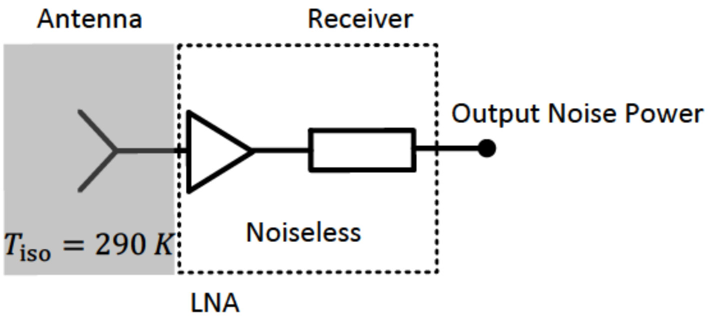

(a) Isolated single receiving antenna.

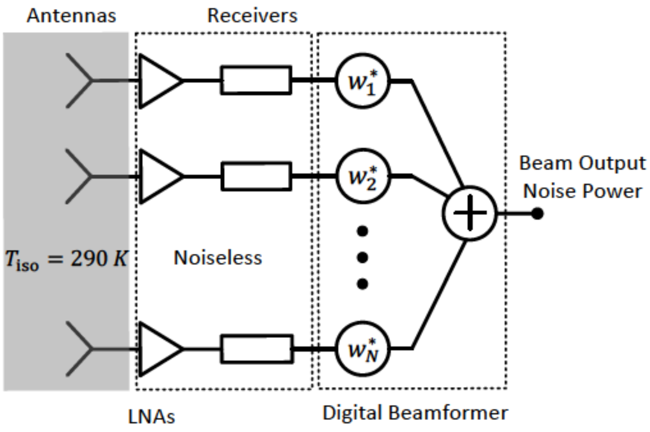

(b) Receiving array antenna.

Figure 6.1: Isotropic noise response for a single and phased array receiving active antennas with noiseless receivers in an environment with 290 K brightness temperature.

Array Antennas

Figure 6.1b illustrates the isotropic noise response for a receiving active phased array antenna including the interaction between antenna element mutual coupling and the digital beamformer with coefficients $\mathbf{w}^*$. In a thermal environment with T_{iso} brightness temperature, the beam output noise power for the active receiving array antenna with noiseless antennas, LNAs and receivers is

$$P_{\text{iso,ext}} = \mathbf{w}^H \mathbf{R}_{\text{iso,ext}} \mathbf{w} \tag{6.3}$$

where $\mathbf{w}$ is a vector of complex beamformer weights, superscript H is the Hermitian conjugate. $\mathbf{R}_{\text{iso}}$ is the isotropic noise response correlation matrix for a lossless antenna,

$$\mathbf{R}_{\text{iso,ext}} = \frac{1}{|I_0|^2} 16 k_{\text{b}} T_{\text{iso}} B \mathbf{Q}\mathbf{A}\mathbf{Q}^H \tag{6.4}$$

where I_0 is the input current into the port of each element, k_{b} is Boltzmann constant, B is antenna bandwidth, $\mathbf{Q}$ is a transfer matrix from open circuit loaded voltages at the array element ports to loaded voltages at the array receiver outputs before beamforming, and $\mathbf{A}$ is a matrix of overlap integral of embedded element pattern $\overline{E}_n(\bar{r})$ with elements given by [34]

$$A_{mn} = \frac{1}{2\eta} \int\limits_{\Omega} \overline{E}_m(\bar{r}) \cdot \overline{E}_n^*(\bar{r}) r^2 d\Omega \tag{6.5}$$

The beam output noise power for active receiving array antenna with lossy antennas and noiseless LNAs and receivers is

$$P_{\text{iso}} = \mathbf{w}^H (\mathbf{R}_{\text{iso,ext}} + \mathbf{R}_{\text{loss}}) \mathbf{w} \tag{6.6}$$

where the antenna loss correlation matrix $\mathbf{R}_{\text{loss}}$ is

$$\mathbf{R}_{\text{loss}} = k_{\text{b}} T_{\text{iso}} B \mathbf{Q} \mathbf{R}_{\text{A,loss}} \mathbf{Q}^H. \tag{6.7}$$

From (6.1), (6.3) and (6.6), the receiving efficiency for the array antenna is

$$\eta_{\text{rec}} = \frac{\mathbf{w}^H \mathbf{R}_{\text{iso,ext}} \mathbf{w}}{\mathbf{w}^H (\mathbf{R}_{\text{iso,ext}} + \mathbf{R}_{\text{loss}}) \mathbf{w}} \tag{6.8}$$

The equivalent temperature of the thermal noise contributed by losses in the antenna elements can be calculated by

$$T_{\text{loss}} = (1 - \eta_{\text{rec}}) T_{\text{ant}} \tag{6.9}$$

where T_{ant} is the physical temperature of the antenna.

6.2.2 Beamformer Weights

Various algorithms can be used to compute array beamformer weight coefficients **w**. Common beamforming algorithms include conjugate field match, maximum sensitivity, maximum gain, and maximum directivity.

Conjugate Field Match

Conjugate field matching (CFM) is used for phased array antennas to steer the beam to a desired direction. The corresponding beamformer weights are given by

$$\mathbf{w}_{\text{CFM}} = \mathbf{E}(\bar{r}) \tag{6.10}$$

where $\mathbf{E}(\bar{r})$ is a vector of polarization-aligned components of the embedded element radiation patterns sampled at the point $\bar{r}$ in the desired beam steering direction. In the case of a phased array feed, $\mathbf{E}(\bar{r})$ becomes $\mathbf{E}_{\text{r}}(\bar{r})$, representing the secondary radiated fields from the array elements in the presence of a reflector antenna.

Maximum Gain and Maximum Directivity

The reflector antenna efficiency can be maximized by the maximum gain beamformer [34]

$$\mathbf{w}_{\mathrm{max,G}} = \mathbf{R}_{\mathrm{iso}}^{-1}\mathbf{E}_{\mathrm{r}}(\bar{r}), \tag{6.11}$$

where $\mathbf{R}_{\mathrm{iso}}$ is calculated by

$$\mathbf{R}_{\mathrm{iso}} = \mathbf{R}_{\mathrm{iso,ext}} + \mathbf{R}_{\mathrm{loss}}. \tag{6.12}$$

The reflector aperture efficiency is optimized by the maximum directivity beamformer

$$\mathbf{w}_{\mathrm{max,D}} = \mathbf{R}_{\mathrm{iso,ext}}^{-1}\mathbf{E}_{\mathrm{r}}(\bar{r}). \tag{6.13}$$

Maximum SNR

Beamformer weights for phased arrays and phased array feeds are commonly used to maximize the sensitivity or SNR for a receiver system [53]. Sensitivity is maximized by the beamformer weight vector

$$\mathbf{w}_{\mathrm{max,S}} = \mathbf{R}_{\mathrm{noise}}^{-1}\mathbf{E}_{\mathrm{r}}(\bar{r}) \tag{6.14}$$

where $\mathbf{R}_{\mathrm{noise}}$ is the receiver output noise correlation matrix including sky noise, spillover, antenna loss noise, and receiver noise.

6.2.3 Effective Resistance for Array Antennas

Degradations in receiving efficiency for active arrays are caused by ohmic or dielectric losses that are distributed throughout the antenna array structure, and the impact of these losses on gain and SNR depends on beamformer coefficients. By analogy with single antennas, we introduce an effective resistance that captures the beam-dependent loss in a single value.

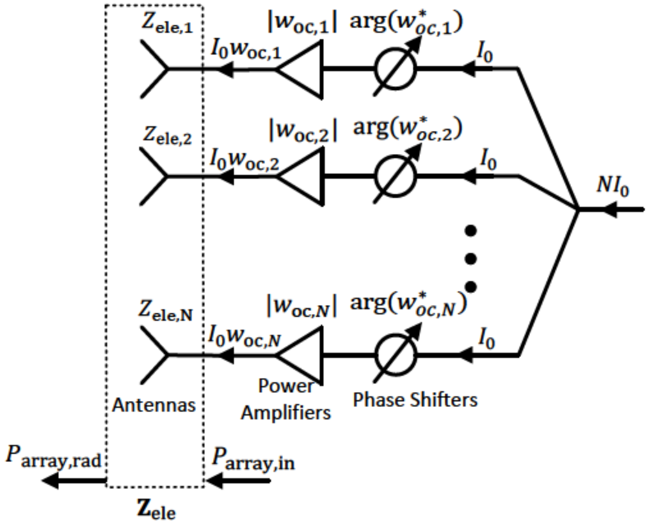

(a) Transmitting array with radiation pattern identical to the receiving pattern of Fig. 6.1b

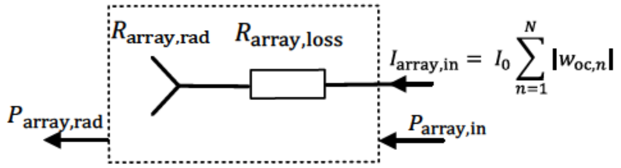

(b) Equivalent transmitting antenna model.

Figure 6.2: Block diagrams for a transmitting array model and the corresponding equivalent model. Under the same array antenna input power $P_{\text{array,in}}$ and radiated power $P_{\text{array,rad}}$, since the summation of the amplitude of input current at the array antenna ports in (a) is equal to the input current of the single antenna in (b), the array model in (a) is equivalent to a single antenna model in (b). The array effective resistance R_{array} can be calculated using the single antenna model by $P_{\text{array,in}}$,$P_{\text{array,rad}}$ and $I_{\text{array,in}}$.

For a single transmitting antenna with input current I_0, the radiation efficiency is the ratio of the radiated power $P_{\text{rad}} = \frac{1}{2} I_0^2 R_{\text{rad}}$ to the antenna input power P_{in}. The input power is the sum of the radiated power and the power $P_{\text{A,loss}} = \frac{1}{2} I_0^2 R_{\text{A,loss}}$ absorbed by antenna losses.

These well known relationships can be generalized using microwave network theory to active array antennas by developing an equivalent transmitting array. The equivalent transmitting array has a radiation pattern that is identical to the receiving pattern of the array shown in Fig. 6.1b. To create the equivalence, we must refer the beamformer weights of the receiving array to a reference plane that is before all nonreciprocal components such as amplifiers and electronics in the receiver chains. Accordingly, we define coefficients $\mathbf{w}_{\mathrm{oc}}$ that when applied to the open circuit equivalent voltages at the unloaded antenna ports produce the same output as the beamformer. The equivalent open circuit voltage referenced weights are given by

$$\mathbf{w}_{\mathrm{oc}} = \mathbf{Q}^{-1}\mathbf{w}. \tag{6.15}$$

For the transmitting array shown in Fig. 6.2a, the input current I_0 on the nth channel is shifted by an angle of $\arg(w^*_{\mathrm{oc,n}})$ and the corresponding amplitude is amplified by a factor of $|w_{\mathrm{oc,n}}|$. Using the electromagnetic reciprocity principle, it can be shown that this transmitting array is equivalent to the receiving array.

For the transmitting array, the relationship between the real part of the array antenna impedance matrix $\mathbf{Z}_{\mathrm{A}}$, the loss resistance matrix $\mathbf{R}_{\mathrm{rad}}$ and the antenna radiation resistance matrix $\mathbf{R}_{\mathrm{loss}}$ is

$$\mathrm{Re}[\mathbf{Z}_{\mathrm{A}}] = \mathbf{R}_{\mathrm{rad}} + \mathbf{R}_{\mathrm{A,loss}}. \tag{6.16}$$

The total input power $P_{\mathrm{array,in}}$ at the array antenna ports is given by

$$P_{\mathrm{array,in}} = \frac{1}{2}\mathbf{w}_{\mathrm{oc}}^H \mathrm{Re}[\mathbf{Z}_{\mathrm{A}}]\mathbf{w}_{\mathrm{oc}}, \tag{6.17}$$

The total radiated power is

$$P_{\mathrm{array,rad}} = \frac{1}{2}\mathbf{w}_{\mathrm{oc}}^H \mathbf{R}_{\mathrm{rad}}\mathbf{w}_{\mathrm{oc}}. \tag{6.18}$$

By conservation of energy, the dissipated power in the array antenna is

$$\begin{aligned} P_{\mathrm{array,loss}} &= P_{\mathrm{array,in}} - P_{\mathrm{array,rad}} && (6.19) \\ &= \frac{1}{2}\mathbf{w}_{\mathrm{oc}}^H \mathbf{R}_{\mathrm{A,loss}}\mathbf{w}_{\mathrm{oc}}. && (6.20) \end{aligned}$$

We now consider a lossless, reciprocal antenna with the same radiation pattern as the phased arrays, and with loss lumped into an equivalent resistance. This simplified model is shown in Fig. 6.2b. The effective radiation resistance is

$$R_{\text{array,rad}} = \frac{2P_{\text{array,rad}}}{I^2_{\text{array,in}}} \tag{6.21}$$

$$= \frac{\mathbf{w}^H_{\text{oc}}\mathbf{R}_{\text{rad}}\mathbf{w}_{\text{oc}}}{\left(\sum\limits_{n=1}^{N}|w_n|\right)^2}, \tag{6.22}$$

The effective loss resistance is

$$R_{\text{array,loss}} = \frac{2P_{\text{array,loss}}}{I^2_{\text{array,in}}} \tag{6.23}$$

$$= \frac{\mathbf{w}^H_{\text{oc}}\mathbf{R}_{\text{A,loss}}\mathbf{w}_{\text{oc}}}{\left(\sum\limits_{n=1}^{N}|w_n|\right)^2}. \tag{6.24}$$

These values are defined for a single formed beam. The effective radiation and loss resistances change with beam scan angle.

Using the definition of array effective resistance for a transmitting array, the receiving efficiency for the corresponding active receiving array in (6.8) is

$$\eta_{\text{rec}} = \frac{\mathbf{w}^H_{\text{oc}}\mathbf{R}_{\text{rad}}\mathbf{w}_{\text{oc}}}{\mathbf{w}^H_{\text{oc}}(\mathbf{R}_{\text{rad}} + \mathbf{R}_{\text{A,loss}})\mathbf{w}_{\text{oc}}} \tag{6.25}$$

$$= \frac{R_{\text{array,rad}}}{R_{\text{array,rad}} + R_{\text{array,loss}}} \tag{6.26}$$

This expression shows that the active array receiving efficiency is analogous to the classical definition of radiation efficiency for transmitting antennas.

6.3 Numerical Analysis

We now study the dependence of active array receiving efficiency, equivalent radiation resistance, and equivalent loss resistance on beam scan angle and beamformer coefficients using a numerical model. We consider as a baseline an isolated element and a single element embedded element in an array, and then turn to the analysis of a beamformed active array. The numerical examples are taken from an L-band array feed system that has been designed, fabricated, and tested on the 100 meter Green Bank Telescope in West Virginia, USA.

6.3.1 Isolated Antenna

Using high conductivity material is the most basic way to reduce antenna loss. The brass dual-pol dipole antenna shown in Fig. 6.3 is plated with copper material, the conductivity for which is 3.6 times higher than that for brass. A full-wave model is used to calculate the antenna loss for one polarization excited. Using (6.1), the calculated receiving efficiency for a single isolated dipole antenna over the frequency bandwidth is shown in Fig. 6.3. The receiving efficiency for the dipole antenna is increased by about 1%, which means from (6.9) the plated copper on the antenna surface when at room temperature decreases the antenna noise temperature by 3 K. For terrestrial communications applications, the improvement is negligible, but for high sensitivity array applications such as astronomical receivers and satellite terminals, this is a significant reduction in system noise.

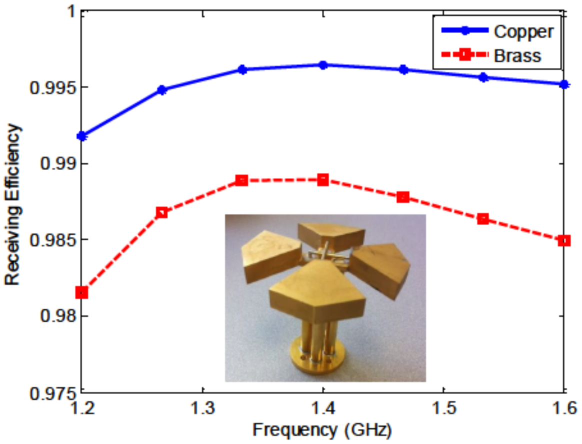

Figure 6.3: Receiving efficiency for an isolated single dipole antenna with different materials over the operation frequency bandwidth.

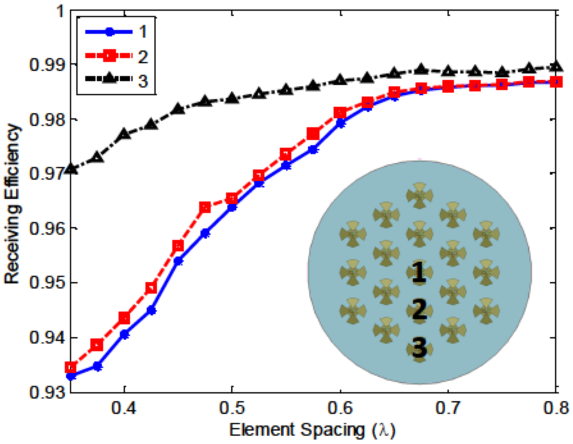

Figure 6.4: Receiving efficiency for singly excited embedded elements in a 19-element focal plane array. The receiving efficiency over different array element spacings is calculated for the excited element when the other elements in the array are open circuited.

6.3.2 Embedded Elements Excited Singly

We now model the same antenna element embedded in an array with a hexagonal layout. The receiving efficiency over different element spacings for center, mid, and edge elements is shown in Fig. 6.4. The beamformer weight vector includes one nonzero value corresponding to the excited element. The receiving efficiency for the center embedded element is similar to the measured results in [27].

When the array element spacing is small, the receiving efficiencies for the embedded elements are lower than that for the isolated element, due to absorption of energy by neighboring elements. The center element has the lowest receiving efficiency. The array edge element has fewer neighboring elements and exhibits the highest receiving efficiency. This numerical example highlights the reduction in radiation and receiving efficiency caused by interaction between elements in an array.

6.3.3 Phased Array With Formed Beams

Receiving Efficiency

As indicated in (6.8), the receiving efficiency for a phased array antenna depends on the correlation matrix related to the array structure and the beamformer weights that control the beam steering angle. For a 19 element array, Fig. 6.5 shows the receiving efficiency over different element spacing for the boresight and 60° steered beams. The receiving efficiency for the boresight direction is larger than that for the 60° steered beam.

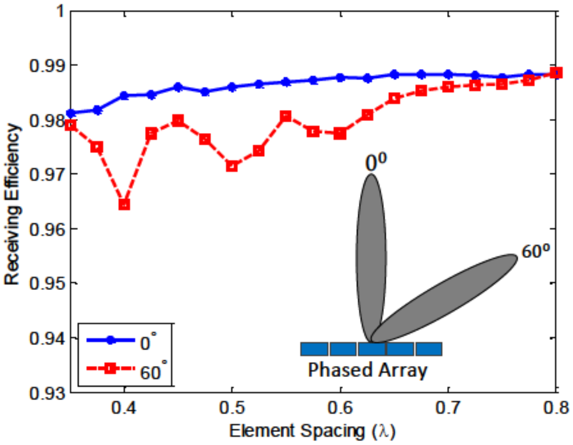

Figure 6.5: Receiving efficiency for a 19-element phased array antenna over element spacing for beams with zenith steering angle 0° and 60°.

Fig. 6.6 shows the array receiving efficiency over the steered angles when the element spacing is 0.4 λ and 0.8 λ, respectively. When the array element spacing is large, mutual coupling is small, and receiving efficiency is constant over the steered angles. When the array element spacing is small, for this array example the receiving efficiency decreases for large angle steered beams.

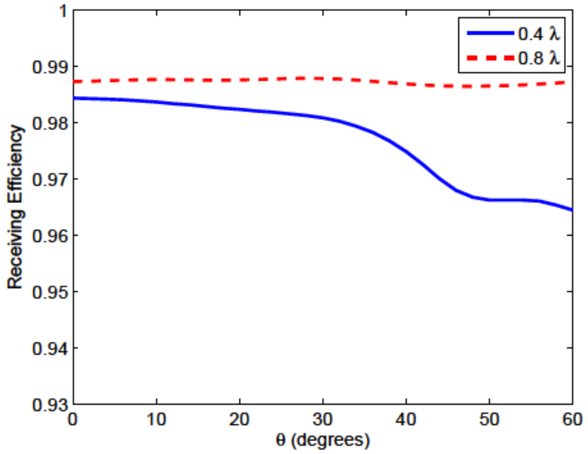

Figure 6.6: Receiving efficiency for a phased array antenna with 0.4λ and 0.8λ element spacing over beam steering angle.

Array Effective Impedance

The array effective radiation and loss resistance over array element spacing in wavelength are shown in Fig. 6.7. The array effective resistance is increased with the decrease of array element spacing. In view of (6.18) and (6.22), the array radiation resistance matrix $\mathbf{R}_{\mathrm{rad}}$ is close to a rank one matrix as the array element spacing becomes small, leading to an increase in the effective radiation resistance.

The decrease in receiving efficiency for the array with 0.4 λ element spacing over steered angles is explained by the array effective resistance in Fig. 6.8. Both the array effective radiation resistance and loss resistance increase at large steered beam angles, but the slope of the effective loss resistance is higher with angle, leading to a net worsening of the receiving efficiency.

6.3.4 Phased Array Feeds

In this section, receiving efficiency for the 19-element phased array antenna operating as a feed in the focal plane of a reflector antenna is studied. The primary feed pattern scatters from the large reflector antenna to produce secondary pattern on the sky. The physical optics approximation is used to compute the secondary radiation patterns. In the model, feed blockage and diffraction from the reflector edges are ignored.

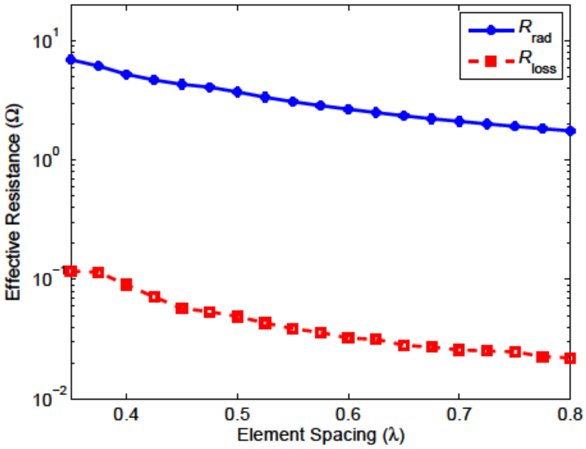

Figure 6.7: Effective array radiation and loss resistance for the boresight beam over array element spacing.

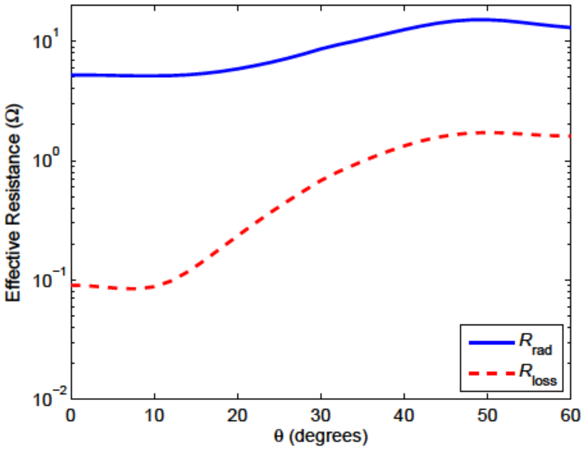

Figure 6.8: Effective array radiation and loss resistance over steering angle when the array element spacing is 0.4 λ.

Steered Beams

Receiving efficiency with the maximum directivity, gain and sensitivity beamformers for the steered formed beams are shown in Fig. 6.9a. The receiving efficiency for the maximum sensitivity beamformer is higher than that for the maximum gain and directivity beamformer, which is due to the high priority of improving antenna noise temperature.

Using the maximum directivity beamformer, receiving efficiency shows a significant decrease when the beam is steered to the edge of the receiving array feed. The array effective radiation and loss resistance are shown in Fig. 6.9b. When the beam is steered to large angles, the fast phase variation for beamformer weights matched to distorted Airy pattern leads to the cancellation of the total radiated far field and results in the decrease of array effective radiation resistance. Meanwhile, rapid weight variation between neighboring elements produces a large oscillation of current on the antennas, which leads to a strong concentrated current on the antenna lossy material and increases the array effective loss resistance.

Element Spacing

Fig. 6.10 shows the receiving efficiency and effective resistance of the 19 element phased array feed with different values for the array element spacing. The aperture field distribution of a phased array feed is approximately a conjugate match to the focused fields distribution on the focal plane of the reflector antenna. To keep the sample rate of the Airy pattern for the reflector with different element spacings, we adjust the ratio of the reflector focal length to diameter (f/D) to match the sampling density of the feed elements to the variation in the fields in the focal plane of the reflector [54]. Receiving efficiency decreases and effective loss resistance increases when the array element spacing is small. As expected, array antenna loss is lower with the maximum sensitivity beamforming algorithm than with other beamformers.

Since the noise temperature for a state-of-the-art feed system for radio telescope is less than 20 K, the dependence of loss and receiving efficiency on scan angle and element spacing are significant and should be accounted for in the design process of phased array feed receiver systems.

6.4 Summary

The influence of mutual coupling on radiation loss and receiving efficiency has been studied for active receiving phased arrays and focal plane phased array feeds. A low loss isolated single array element leads to a high array antenna loss under strong mutual coupling and steered beams with large scanned angles.

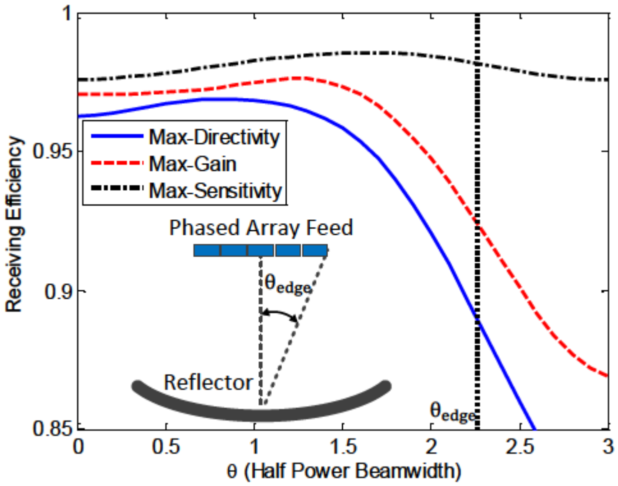

(a) Receiving efficiency.

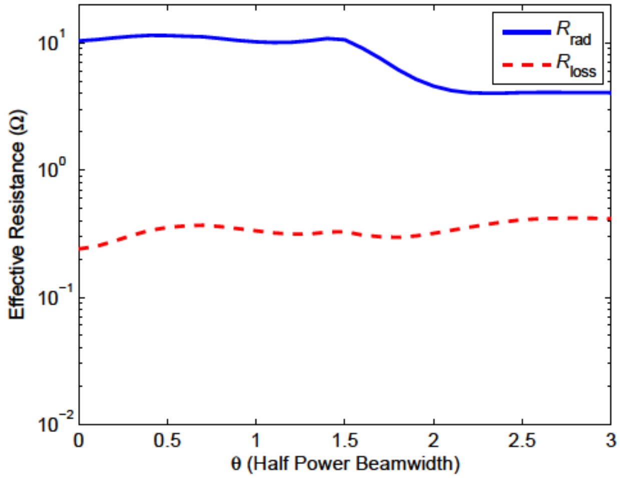

(b) Effective array resistance for the maximum directivity beamformer.

Figure 6.9: Receiving efficiency for a focal plane array with 0.35 λ element spacing when the reflector f/D is 0.35. Maximum directivity, gain and sensitivity beamforming algorithms are used to form the steered beams. The vertical dot line represents the angle of the steered beam on the array edges.

To better understand the physics of array antenna loss, we introduced a new definition of array effective resistance to equivalent the array model to a single antenna model. Strong mutual coupling and large variation in beamformer weights over the array lead to a decrease of the array effective resistance and an increase in the effective loss resistance, due to the strong concentrated current on antennas. Compared to the phased array antennas, antenna loss for phased array feeds

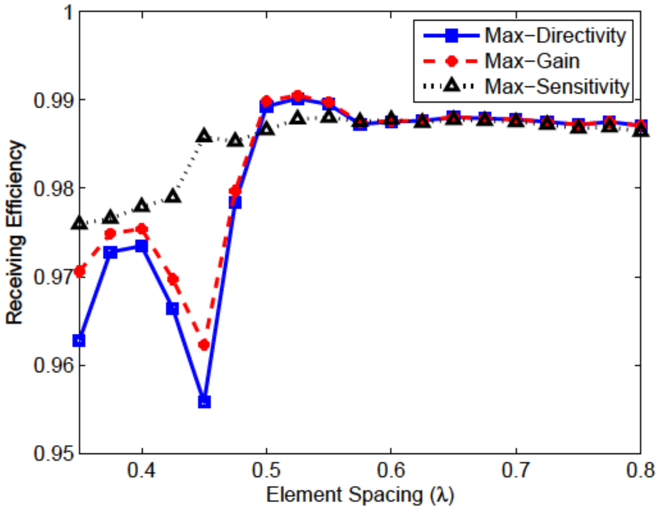

(a) Receiving efficiency.

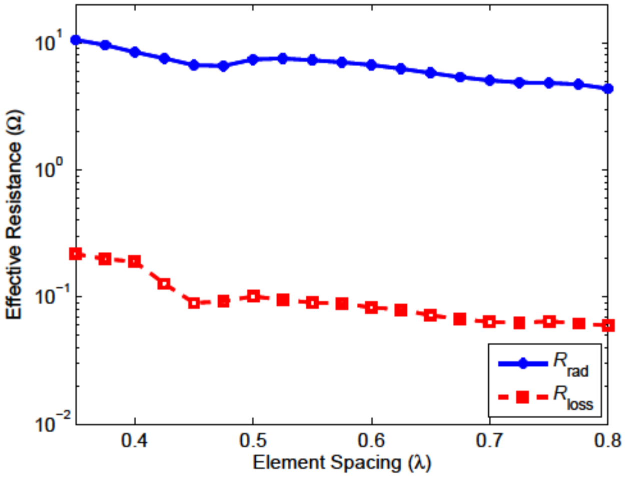

(b) Effective array resistance for the maximum sensitivity beamformer over element spacing for a phased array feed.

Figure 6.10: Receiving efficiency for a phased array feed with element spacing adjusted to maintain a fixed sampling rate of the Airy pattern.

is more sensitive to mutual coupling and steered beams. The array effective resistance can be used to understand array radiation and loss properties and improve the performance of high sensitivity array designs.

CHAPTER 7. SIDE LOBE LEVEL AND APERTURE EFFICIENCY OPTIMIZATION FOR WIDE SCANNED TILED APERIODIC ARRAY ANTENNAS

Array antennas with aperiodic element placement provide a way to mitigate grating lobe level when the array element spacing is larger than one half wavelength. Compared to periodic structure, aperiodicity makes such arrays difficult to design and optimize. In this work, uniform array with discrete rotated tiles uses to reduce the complexity for aperiodic array. Peak side lobe level (PSLL) is minimized by optimizing the element position for one tile and tile discrete rotated angle. An approximate formula related to element pattern is proposed to indicate the relationship between PSLL and array element number and density for aperiodic and tiled arrays. PSLL, sensitivity of PSLL changed with frequency, directivity and design and optimization complexity for uniform arrays, aperiodic arrays and tiled arrays are compared.

7.1 Introduction

Uniform arrays with equal element spacing have been widely used for simple design and fabrication. For many applications such as wide scanned beams, sparse array element distribution, and wide bandwidth operation, however, grating lobes appear when the array element spacing is larger than one half wavelength. Aperiodic arrays offer one possible solution to grating lobe mitigation.

In the early studies of aperiodic arrays, due to limited computer power, arrays were commonly treated as random arrays and peak side lobe levels (PSLLs) were predicted probabilistically [55–60]. As computer power increased and parallel processing become prevalent, optimization methods such as genetic algorithm have been developed to minimize PSLLs by optimizing array element position [61–64], or removing a certain percentage of elements from uniform dense arrays [65–68]. Low PSLLs can be achieved over large beam steered angles from the boresight direction when the array average element spacing is larger than one half wavelength [66].

Table 7.1: Comparison for array performance

	Uniform	Aperiodic	Rotated Tiles
PSLL	High	Low	Moderately Low
PSLL Bandwidth	Narrow	Wide	Moderately Wide
Directivity (Dense Array)	High	Low	Moderate
Complexity	Easy	Difficult	Moderate

Compared to uniform arrays, aperiodicity makes the aperiodic arrays difficult to design and optimize. It is complicated to design a power division network with equal phase delays from input port to output ports connected to array elements. Recently, arrays with aperiodic tiles have been developed to decrease the complexity of aperiodic arrays [69–74]. Identical tile units and fewer aperiodic array elements help to reduce design and optimization complexity for the aperiodic arrays. However, PSLL was reported higher than that for the aperiodic arrays due to the less degrees of freedom of array element positions [72].

To solve the high PSLL issue, in this paper, we designed a tiled array with optimized tile element positions and tile discrete rotated angles. Compared to the analysis of rotated tiled arrays with probabilistical method in [72], this analysis method is closer to the practical array design requirement. PSLLs are optimized for aperiodic arrays and tiled arrays. The relationship between PSLL, array element number and density and element radiation pattern is studied. PSLL, PSLL bandwidth, directivity and design and optimization complexity for uniform arrays, aperiodic arrays and tiled arrays are compared in Table 7.1.

7.2 Analysis Methods

Fig. 7.1a illustrates radiated field E_{ele} from an isolated antenna with an input current I_0. For a phased array antenna, the embedded element pattern can be modeled using a full-wave numerical method, but to speed up the optimization of array element positions and tile rotated angles, the embedded element patterns are approximated by the isolated antenna pattern. The accuracy of this approximation is verified by Fig. 7.2.

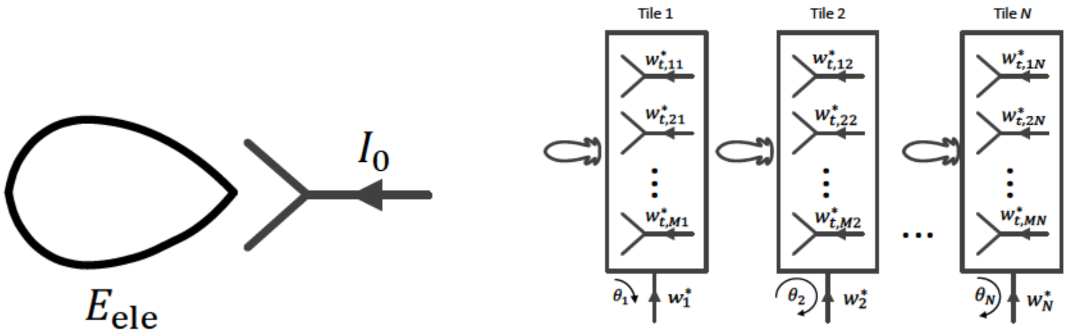

(a) Single antenna.

(b) Phased array antenna with N rotated tiles and M elements for each tile.

Figure 7.1: Block diagrams for an isolated single array element and a phased array antenna with rotated tiles. The embedded element pattern is approximated by the single isolated antenna pattern for each array element. The conjugate field match beamformer is used to maximize the directivity at the beam steering direction.

In Fig. 7.1b, for an array with rotated tiles, the mth element position in the nth tile with rotated angle θ_n is

$$\begin{bmatrix} x'_{mn} \\ y'_{mn} \end{bmatrix} = \begin{bmatrix} \cos\theta_n & -\sin\theta_n \\ \sin\theta_n & \cos\theta_n \end{bmatrix} \begin{bmatrix} x_{mn} \\ y_{mn} \end{bmatrix} \tag{7.1}$$

where (x_{mn}, y_{mn}) is the original tile element position. The tile element radiated fields can be calculated by

$$\overline{E}_{\mathrm{ele},mn}(\bar{r}) = e^{jk_0(\hat{r}_x x'_{mn} + \hat{r}_y y'_{mn})}\overline{E}_{\mathrm{ele}}(\bar{r}), \tag{7.2}$$

where the overbar denotes a three-dimensional field vector and all the fields are phasors relative to e^{jwt}.

Phase shifters connecting to array elements use to control beam steering angles for phased array antennas. For the maximum directivity beamformer, the excitation current vector $\mathbf{w}^*_{\mathrm{t},n}$ in the nth tile with m elements is equal to a set of complex conjugates of element radiated field $\mathbf{E}^*_{\mathrm{ele},n}(\bar{r}_0)$

when the beam is steered to the $\bar{r}_0$ direction, or conjugate field match beamformer, so that

$$\mathbf{w}_{\mathrm{t},n} = \mathbf{E}_{\mathrm{ele},n}(\bar{r}_0), \tag{7.3}$$

where the bold font represents a M-element vector with one value for each element in the nth tile. The total radiated field for the nth tile is

$$\overline{E}_{\mathrm{t},n}(\bar{r}) = \frac{1}{I_0}\sum_{n=1}^{N}\mathbf{w}_{\mathrm{t},n}^{*}\mathbf{E}_{\mathrm{ele},n}(\bar{r}). \tag{7.4}$$

To account for the first order mutual coupling between array elements, an element radiation pattern overlap integral is used to calculate the total radiated power of the array antenna by

$$P_{\mathrm{rad}} = \frac{1}{|I_0|^2}\mathbf{w}^H\mathbf{A}\mathbf{w}, \tag{7.5}$$

where $\mathbf{w}$ is an N-element vector complex conjugate matched with the radiated field at the expected beam steered direction $\bar{r}_0$. $\mathbf{A}$ is an $N\times N$ pattern overlap matrix with elements given by

$$A_{mn} = \frac{1}{2\eta}\int_{\Omega}\overline{E}_{\mathrm{t,m}}(\bar{r})\cdot\overline{E}_{\mathrm{t,n}}^{*}(\bar{r})r^2 d\Omega. \tag{7.6}$$

The total radiated power density of the array antenna at the steered direction $\bar{r}_0$ is

$$S(\bar{r}_0) = \frac{1}{|I_0|^2}\mathbf{w}^H\mathbf{B}(\bar{r}_0)\mathbf{w}, \tag{7.7}$$

where $\mathbf{B}(\bar{r}_0)$ is an $N\times N$ matrix with elements given by

$$B_{mn}(\bar{r}_0) = \frac{1}{2\eta}\overline{E}_{\mathrm{t,m}}(\bar{r}_0)\cdot\overline{E}_{\mathrm{t,n}}(\bar{r}_0). \tag{7.8}$$

Using the overlap matrix $\mathbf{A}$ and the radiation matrix $\mathbf{B}$, the total directivity in the direction $\bar{r}_0$ is

$$D(\bar{r}_0) = \frac{4\pi r^2\mathbf{w}^H\mathbf{B}(\bar{r}_0)\mathbf{w}}{\mathbf{w}^H\mathbf{A}\mathbf{w}}. \tag{7.9}$$

PSLL is calculated by

$$\mathrm{PSLL(dB)} = -10\log_{10}\left(\frac{D(\bar{r}_0)}{D(\bar{r}_\mathrm{g})}\right), \tag{7.10}$$

where $\bar{r}_\mathrm{g}$ represents the PSLL direction.

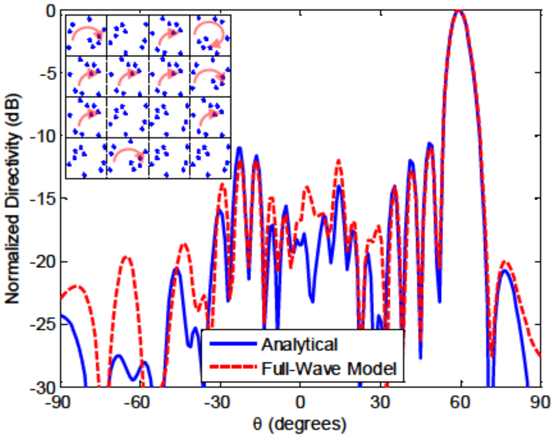

Figure 7.2: Comparison of analytical model and full-wave model radiation pattern for a 12×12-element uniform array with optimized discrete rotated aperiodic tiles. Tiled array configuration is shown in the subplot.

To validate the accuracy of this model, we compare this array model to a full-wave model with a FDTD-based simulator (EMPIRE, IMST GmbH). The total array element number is 144 and the element type in the full-wave model is a traditional square shape microstrip antenna. In Fig. 7.2, the calculated radiation pattern for the 60° steered beam in the H-plane using the array model agrees well with that using the full-wave model, validating the accuracy of the use of array model in the following studies.

7.3 Aperiodic Array

7.3.1 Array Model

When the main lobe of an aperiodic array antenna with $N_{\text{el}} = m \times n$ elements is steered to (θ_0, ϕ_0) direction, the total radiated field is

$$\overline{E}_{\text{array}}(\theta, \phi) = \sum_{m=1}^{M} \sum_{n=1}^{N} e^{jk(\mu_1 x_{mn} + \mu_2 y_{mn})} \overline{E}_{\text{ele}}(\theta, \phi) \tag{7.11}$$

where

$$\mu_1 = \sin\theta\cos\phi - \sin\theta_0\cos\phi_0 \tag{7.12}$$

$$\mu_2 = \sin\theta\sin\phi - \sin\theta_0\sin\phi_0 \tag{7.13}$$

$$x_{mn} = mx_0 + \Delta_{x,mn} \tag{7.14}$$

$$y_{mn} = ny_0 + \Delta_{y,mn}, \tag{7.15}$$

(x_0, y_0) is element position for a uniform array and $(\Delta_{x,mn}, \Delta_{y,mn})$ is the element offset distance from (x_0, y_0).

Array main lobe direction (θ_0, ϕ_0) is controlled by phase shifters, where the E-fields radiated from array elements are in-phase superposition. For a uniform array, $jk(\mu_1 x_{mn} + \mu_2 y_{mn})$ in (7.11) becomes zero in the direction of grating lobe and the radiated fields from each element are in-phase superposition leading to a strong grating lobe level. For an aperiodic array, $jk(\mu_1 x_{mn} + \mu_2 y_{mn})$ in (7.11) becomes nonzero and the total radiated field can be canceled by optimizing the element offset position.

In Fig. 7.3, the array model in section 7.2 without rotated tiles uses to analyze PSLL of an aperiodic array when the θ for the main beam is steered from 0° to 60° by ϕ from 0° to 360°. The maximum PSLL occurs when the beam is steered to the largest angle from the zenith direction. To simplify the design process, PSLL is optimized when θ is 60° and ϕ is 0°, 45° and 90°, respectively.

To make the array model close to practical applications, an analytical $0.5\lambda \times 0.5\lambda$ TE_{10}-mode aperture with ground plane is used as array element model. Array element offset distance

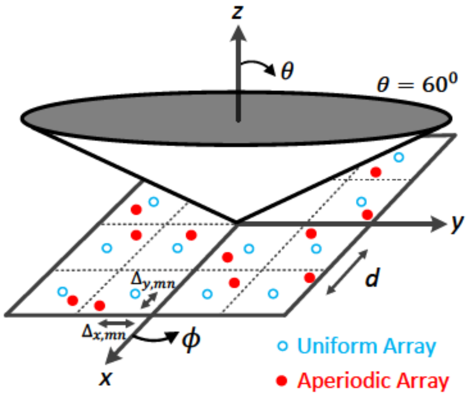

Figure 7.3: Design requirement for an aperiodic array. PSLL is minimized by optimizing the array element offset distance ($\Delta_{x,mn}, \Delta_{y,mn}$) when the main lobe is steered from 0° to 60° in θ by ϕ from 0° to 360°. Average element spacing for aperiodic array is d.

$\Delta_{x,mn}$ and $\Delta_{y,mn}$ are optimized by genetic algorithm to minimize PSLL. To ensure statistical reliability of the optimized results, population number is set as 200 and the best fitness function is the reciprocal of the maximum PSLL in dB. The optimization process is stopped when the average relative change in the best fitness function values over 50 generations is less than 1×10^{-4}.

7.3.2 Optimization Results

As shown in Fig. 7.4, PSLLs for optimized aperiodic arrays are compared over steered beams, element density, element number and array length. PSLL for the optimized 60° steered beam is higher than that for the 0° and 30° beams, which is due to the relative higher element directivity at 60°.

Fig. 7.4a and 7.4b show PSLLs over element number and array length when the element average spacing d and element number is fixed, respectively. The results indicate that PSLLs can be reduced by increasing array element number and density. When the array length or element spacing is fixed, PSLLs decrease by the inverse of array element number, but the decreased speed in Fig. 7.4c is faster than that in Fig. 7.4a.

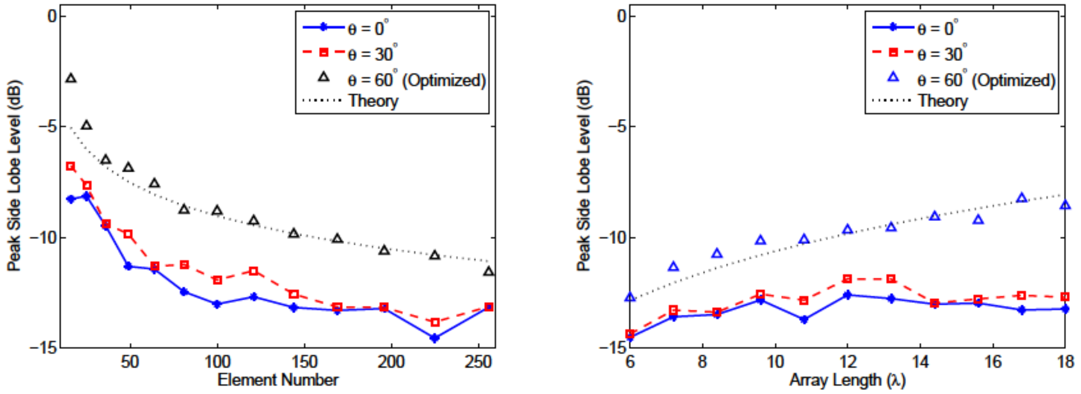

(a) Fixed 1λ average element spacing.

(b) Fixed 144 array element number.

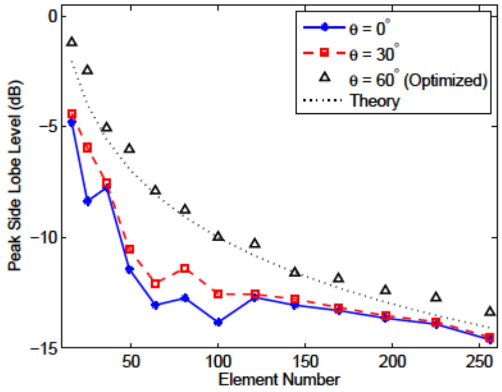

(c) Fixed 8λ array length.

Figure 7.4: Peak side lobe level for an aperiodic array over element density, element number and array length. The optimized peak side lobe level for the 60° beam is compared to that for the 0° and 30° beams. The accuracy for the approximate formula in (7.16) is validated by the optimized results.

To fit the bulk optimized PSLL results, a simple formula is proposed for an optimized aperiodic array by

$$\mathrm{PSLL(dB)} = -10\log_{10}(\mathrm{D_{ele}}(\theta_0,\phi_0)\frac{\mathrm{N_{el}}}{L/\lambda}), \tag{7.16}$$

where $D_{\mathrm{ele}}(\theta_0,\phi_0)$ represents element directivity at the main lobe direction (θ_0,ϕ_0) and L is array length. Compared to the probabilistic prediction of PSLLs for random arrays in [56, 58], this formula is simpler and closer to the practical application.

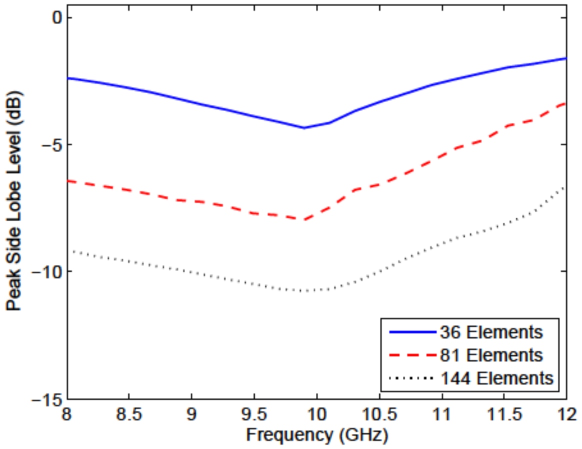

Figure 7.5: Peak side lobe level for an aperiodic array with 8λ array length over frequency, where the aperiodic array is optimized at 10 GHz.

PSLLs for aperiodic arrays over frequency and element number are shown in Fig. 7.5, where the array element positions are optimized at 10 GHz. The slope of PSLL at the high frequency range is larger than that when the frequency is decreased at the low frequency range. For an aperiodic array design, instead of optimizing PSLL over the whole operating bandwidth, the design process can be simplified by optimizing a single frequency at the high end of the operation frequency range.

7.4 Arrays with Rotated Aperiodic Tiles

From the above study, we have found that aperiodic arrays show low PSLLs over wide scanned angles and large frequency bandwidth. The aperiodic structure, however, makes it extremely difficult to design and optimize. Array with rotated aperiodic tiles reduces the design and optimization complexity by the repetitive structures. Using the array model in section 7.2, genetic algorithm optimizes array element positions and tile discrete rotated angles. Optimization setups for the genetic algorithm are the same as those for the aperiodic arrays.

Fig. 7.6 shows an example for an aperiodic array and the corresponding arrays with different size of rotated aperiodic tiles. The array length is 12λ and the total array element number is 144. Original element positions for each tile are identical and discrete rotated angle step is 90°.

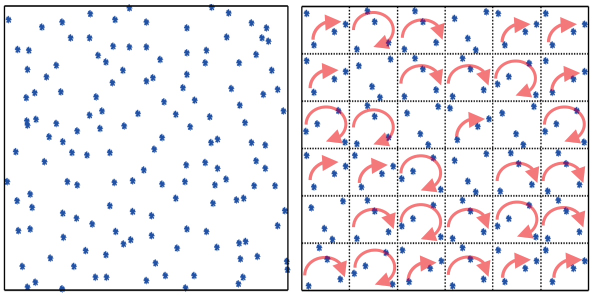

144-Element Aperiodic Array

4-Element Tile

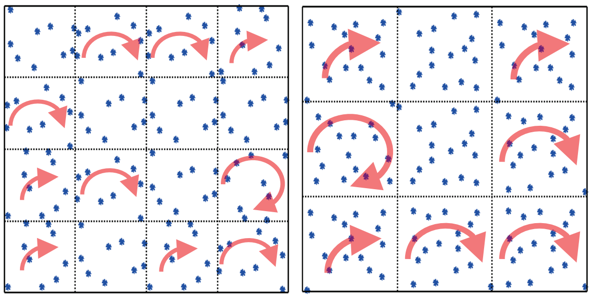

9-Element Tile

16-Element Tile

Figure 7.6: Optimized array configuration for a $12\lambda \times 12\lambda$ aperiodic array with 1λ average element spacing and the corresponding array with rotated aperiodic tiles. The tile size is changed from $2\lambda \times 2\lambda$ to $4\lambda \times 4\lambda$ and the discrete rotated angle step is 90°.

To study the array with different tile sizes, the tile length is changed from 2λ to 4λ. PSLLs are minimized by optimizing the tile element positions and the tile rotated angles.

Fig. 7.7 shows the optimized PSLL for tiled arrays over element density, element number and array length. Under the same array element number and density, PSLL for a tiled array is closed to that for an aperiodic array. By selecting the lowest PSLL over different tile sizes, Table. 7.2 shows the average and maximum differences of PSLLs between the tiled arrays PSLL_t and the aperiodic arrays PSLL_ap. Since the average difference is about 1 dB, PSLLs for the tiled arrays are comparable to the aperiodic arrays. For tiled arrays, the relationship between PSLLs and element number and density can be represented by (7.16).

Table 7.2: Peak Side Lobe Level Difference (dB)

PSLL_t - PSLL_ap	$L = 8\lambda$	$d = 1\lambda$	$N_\text{el} = 144$
Average Difference	1.0	1.3	0.6
Maximum Difference	1.5	2.3	1.4

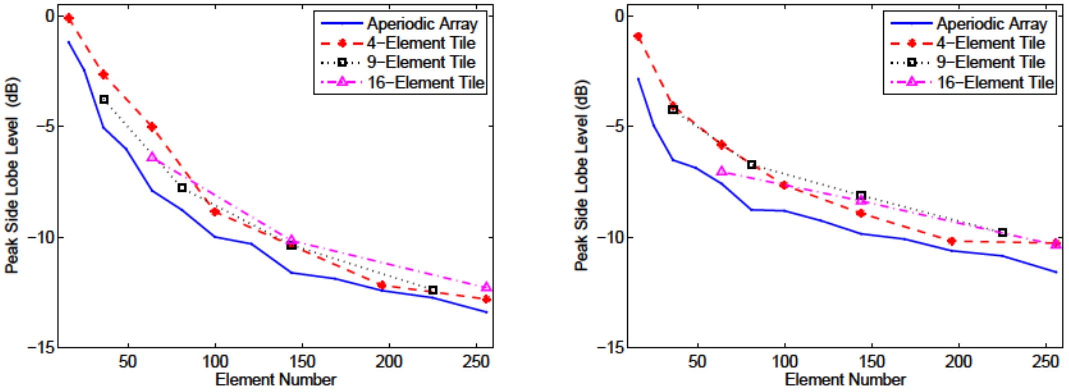

(a) Fixed 8λ array length.

(b) Fixed 1λ average element spacing.

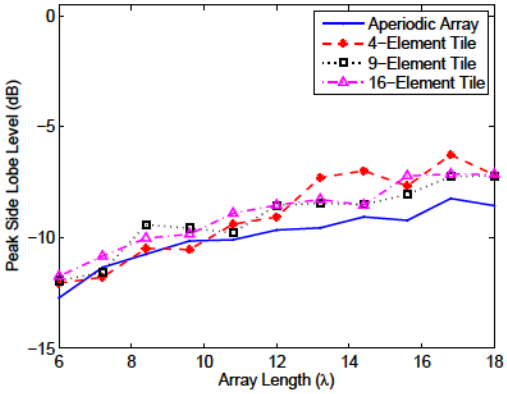

(c) Fixed 144 array element number.

Figure 7.7: Peak side lobe level for an array with rotated aperiodic tiles over element density, element number and array length. Compared to an aperiodic array, the average peak side lobe level for the tiled array is comparable to that for the aperiodic array.

When the array operating frequency is optimized at 10 GHz, PSLLs over frequency and element number are shown in Fig. 7.8. Similar to the aperiodic arrays in Fig. 7.5, PSLL for the array with small element spacing in wavelength is lower than that for the array with large element spacing in wavelength. To simplify the optimization of the tile array over a wide bandwidth, the optimized frequency should be at the high end of the operating bandwidth.

7.5 Comparison of Aperiodic and Tiled Array Performance

In the above section, we have found that PSLLs for the tiled arrays are comparable to that for the aperiodic arrays. To better elucidate the performance different between uniform arrays,

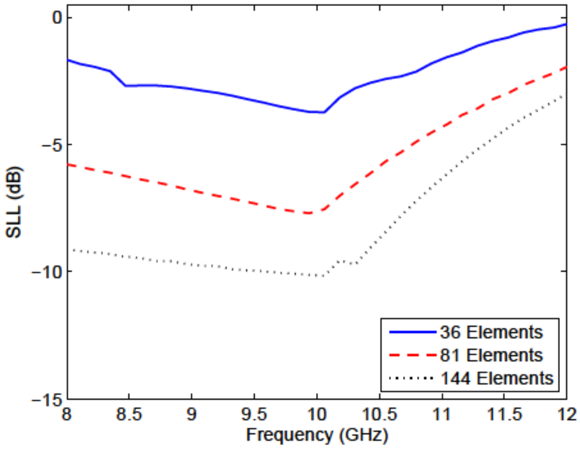

Figure 7.8: Peak side lobe level for an array with rotated aperiodic tiles changing with frequency and element number. The array optimized length is 8λ at 10 GHz.

aperiodic arrays and tiled arrays, we compare the arrays by PSLL, PSLL bandwidth, directivity and design complexity.

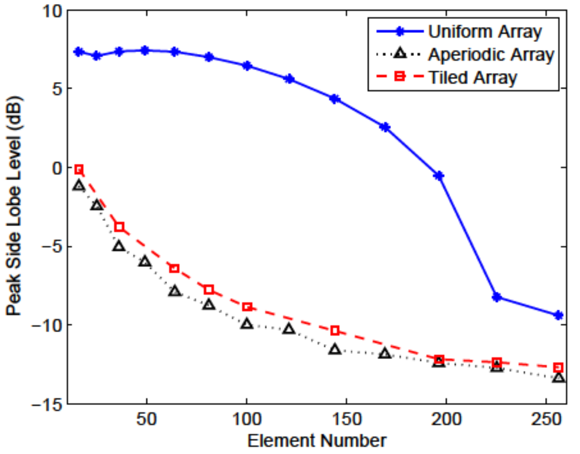

Figure 7.9: Comparison of peak side lobe level for an array with 8λ length. 256 array element number corresponds to 0.5λ average element spacing.

Fig. 7.9 shows a comparison of PSLLs for an array with 8λ length. For the uniform arrays, significant grating lobes occurs when the element density is sparse. PSLLs for the aperiodic and tiled arrays are lower than that for the uniform arrays.

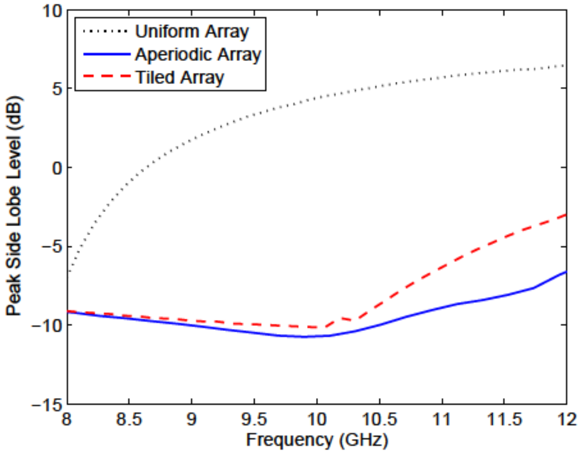

Figure 7.10: Comparison of peak side lobe level changing with frequency for an array with 8λ length at 10 GHz and 144 element number.

Fig. 7.10 shows a comparison of PSLLs over frequency when the array length is 8λ and the array element number is 144. The grating lobe level for the uniform array is largely decreased when the operating frequency is lower than 10 GHz. In the high frequency range, the increase of PSLLs for the tiled arrays are faster than that for the aperiodic arrays.

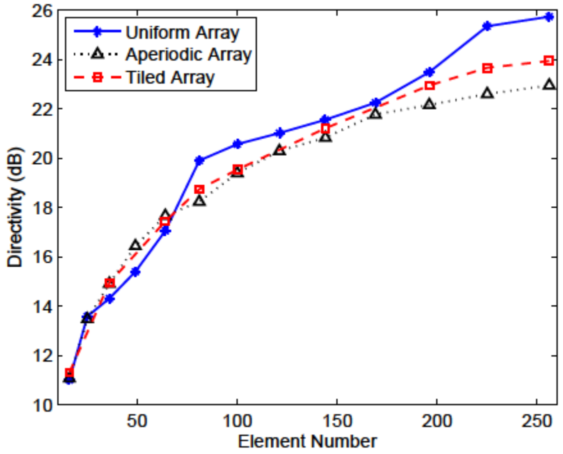

Figure 7.11: Comparison of directivity for an array with 8λ length. The array element number with 256 corresponds to 0.5λ average element spacing.

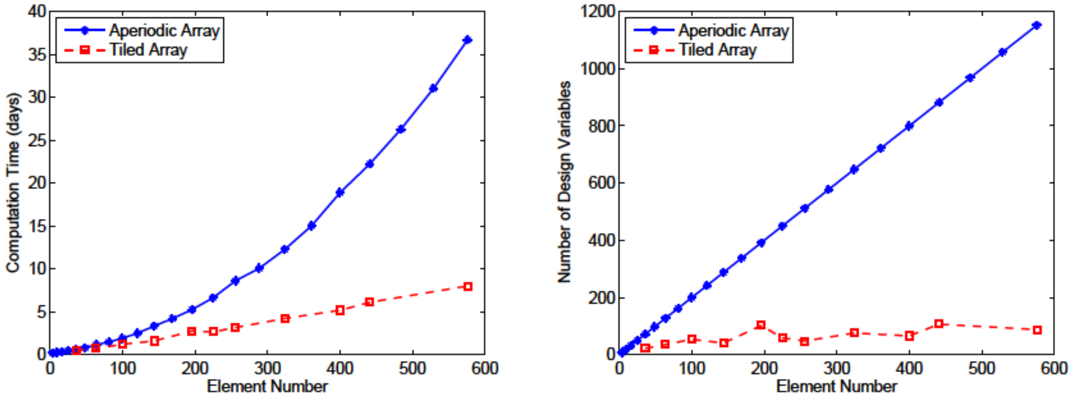

(a) Optimization time.

(b) Number of design variables.

Figure 7.12: Comparison of design complexity for aperiodic array and tile array over different array element number.

Fig. 7.11 shows a comparison of directivity for an array with 8λ length. For the sparse array, the directivity for the uniform array is close to that for the aperiodic and tiled arrays. When the average element spacing is close to 0.5λ, however, the uniform array shows the highest directivity. The reason can be explained by the element-gain paradox that the aperiodic array directivity can be significantly decreased when the array element spacing is smaller than 0.5λ [75,76]. Compared to Fig. 7.9, although aperiodic dense arrays show advantage in low PSLLs, the directivity for uniform arrays are higher than that for aperiodic arrays.

Fig. 7.12 shows a comparison of optimization time and the corresponding design variable number for aperiodic and tiled arrays. Due to the repetitive structure, the design and optimization complexity for the tiled array is significantly decreased when the array element number is large.

To summarize the above study, Table 7.1 shows a comparison of array performance. When the average element spacing is small in wavelength, uniform array shows advantages in terms of directivity and design and optimization complexity. Tiled arrays show low side lobe level, wide frequency PSLL bandwidth and moderately easy for design and optimization.

7.6 Summary

PSLLs for aperiodic arrays and uniform arrays with discrete rotated aperiodic tiles have been studied. Compared to aperiodic arrays, design and fabrication complexity can be largely reduced by tiled arrays. An approximate formula indicates that PSLLs for the aperiodic and tiled arrays can be reduced by enhancing element directivity at the steered beam direction, increasing element number and reducing array size. PSLLs for the tiled arrays are modestly higher than that for the aperiodic arrays. Compromise between peak side lobe level, sensitivity of PSLLs changed with frequency, directivity and design and optimization complexity for uniform arrays, aperiodic arrays and tiled arrays are studied.

CHAPTER 8. SUPERDIRECTIVITY STUDY USING POYNTING STREAMLINE METHOD

A receiving antenna alters an incident field in such a way that the field is concentrated at the terminals of the antenna. The Poynting power flux density vector associated with the field carries to the antenna the power dissipated in the antenna structure and the load. Streamlines of the Poynting vector field can be used to understand electromagnetic energy flow near linear and aperture antennas. Poynting streamlines provide a way to understand and guide the design of superdirective antennas. Directivity-enhancing screens that attract Poynting streamlines and increase the aperture efficiency of a horn antenna to almost 200% are studied. Superdirective antennas generally have limited practical value due to poor radiation efficiency, narrow bandwidth and extreme sensitivity to fabrication errors. We show that these limitations can be mitigated by using metal-only structures that are optimized for broadband operation. The tradeoff between peak achievable aperture efficiency and bandwidth is explored.

8.1 Introduction

Antennas are commonly modeled and understood as transmitters, and reciprocity is used to obtain the receiving properties of the antennas. While it is less common in the field of antenna theory, antennas can also be analyzed directly as receivers. A receiving antenna can be viewed as a field concentrating device. The electric field associated with an incident wave is influenced by the presence of the antenna structure in such a way that fields near the antenna are bent and concentrated so that a high electric field appears at the antenna terminals and power is delivered to the antenna load. The energy flow distribution near the antennas and the effective area shapes can be calculated using streamlines of the Poynting vector field. The existence of streamlines, integral curves, or flow lines for vector fields is a topic of differential geometry [77]. Physically, streamlines which terminate on the antenna load correspond to power absorbed by the antenna, and streamlines that miss the antenna represent power that is not absorbed. The locus of streamlines that terminate on the antenna load provides a way to assign a geometrical shape to the effective area [78].

The Poynting streamline method has been used by several authors to analyze wire antennas [78–80]. We have extended the Poynting streamline method to aperture antennas and guide the design of superdirective antennas. Using the finite element method (FEM) and post-processing to compute streamlines of the Poynting vector field, we use Poynting streamlines to study the effect of the antenna on the power flow in the electromagneic field near dipoles, conventional horns, and superdirective horn antennas. The Poynting streamline approach is used to assign a geometrical shape to the effective area of these antennas, and we find that this shape reflects the physical behavior of the antenna in interesting ways.

For superdirective antennas, Poynting streamlines over a larger area than the aperture are attracted to the antenna and terminated on the load. For an arbitrary aperture field distribution, there is no limit on directivity, and Poynting streamlines over an arbitrarily wide area can be attracted to the antenna. Practical considerations, however, limit both the degree of achievable superdirectivity and the usefulness of superdirective antennas. Drawbacks include narrow bandwidth, low radiation efficiency, and extreme sensitivity to perturbations and fabrication errors [81]. Due to ohmic or dielectric losses exacerbated by intense near fields and currents on the antenna structure, radiation efficiency can be poor for superdirective antennas, meaning that superdirectivity does not necessarily imply that the antenna achieves a higher gain than a uniformly illuminated aperture antenna of the same size.

Superdirectivity is typically implemented for small antennas by extending the near field distribution of the antenna in a variety of ways. Less attention has been given to superdirectivity for electrically large antennas. High directivity horn antennas have been designed using corrugated structures [82], dielectric lenses [83] and metamaterials [84]. We use the Poynting streamline method to enhance the gain of a traditional TE_{10} horn antenna. The horn antenna with gain enhanced by a screen of rods achieves a modeled aperture efficiency from 80% to almost 200%. We also give a design that achieves broadband operation, overcoming a practical limitation of most narrowband superdirective antennas.

Two different metal screen structures for the superdirective horn antenna are compared over frequency, the relationship between the bandwidth and superdirecitivity is studied, and the impact of loss on radiation efficiency is considered over the superdirective operating regime. Through these examples, Poynting streamlines are shown to be a useful tool in understanding the physics of receiving antennas and in creating superdirective antennas that promise better performance than has been realized in the past.

8.2 Numerical Analysis

A full-wave numerical model is used to study Poynting streamlines for receiving antennas. In order to focus on the field bending effect influenced by the directivity and antenna structure, the antenna load is conjugate matched to the antenna input impedance and the antenna structure is assumed to be lossless except where otherwise indicated.

The Poynting vector associated with the total field is computed from the electric and magnetic field for a uniform plane wave normally incident on the antenna [80].The antenna polarization is assumed to be aligned with the incident field. For convenience in software implementation, we extract the Poynting vector on a cut plane that passes through the phase center of the antenna. Streamlines are generated in post-processing for each cut plane by finding paths that are everywhere tangential to the Poynting vector field.

8.2.1 Wire Antennas

As an illustration of the Poynting streamlines technique, we consider a dipole antenna and a 15 element Yagi-Uda antenna. For the dipole antenna, the length and diameter are 0.43 λ and 0.017 λ respectively. A lumped port load is used between two dipole arms with a feed gap of 0.017 λ. For the Yagi-Uda antenna, the antenna axial length and the driven elements length is 3.9 λ and 0.47 λ respectively. The parameters for the reflector and driven element are given in [85]. The loads for both antennas are conjugate matched to the antenna input impedance and the antenna S_{11} relative to a $50\,\Omega$ system impedance is -15.6 dB and -10 dB respectively. A uniform plane wave is incident on the antennas from the broadside direction.

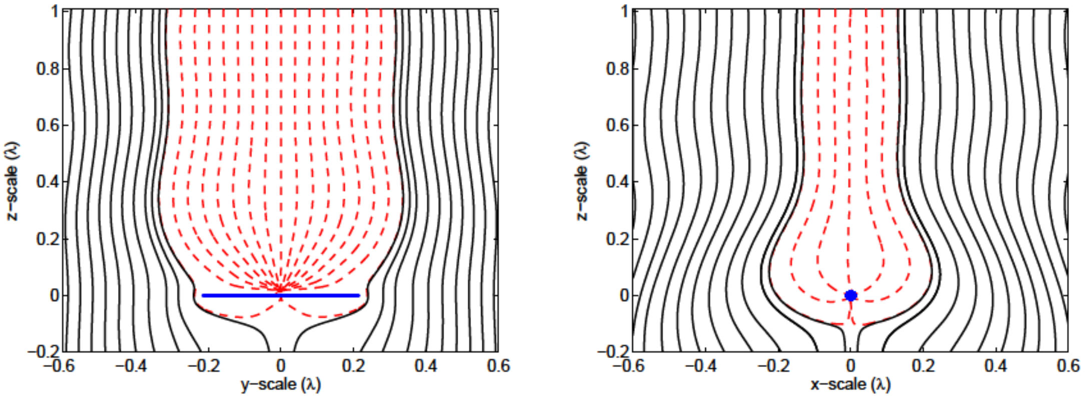

(a) E-plane.

(b) H-plane.

Figure 8.1: Streamline for the Poynting vector of the total fields for a simple dipole antenna with 0.43 λ length. The horizontal straight line represents the actual size of the dipole antenna.

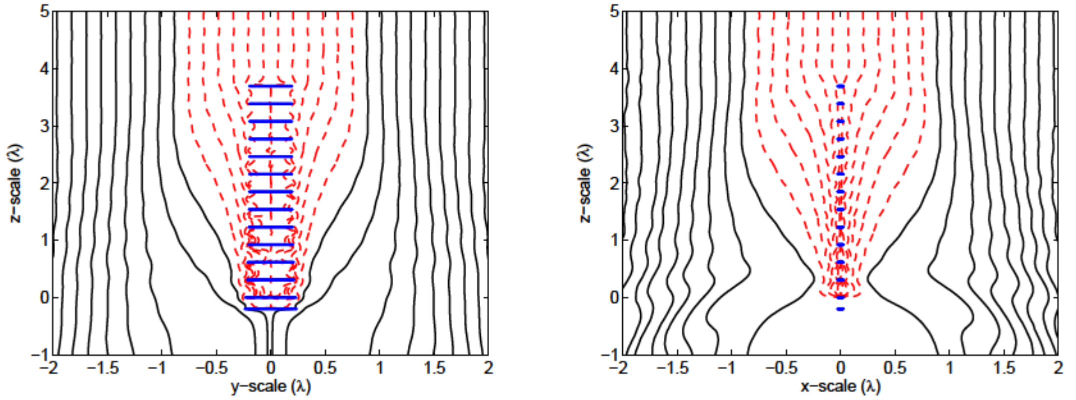

(a) E-plane.

(b) H-plane.

Figure 8.2: Streamlines for the Poynting vector of the toal fields for 15 element Yagi-Uda antenna. The excitation element length is 0.47 λ.

The resulting streamline distributions for the dipole and Yagi-Uda antennas are shown in Figure 8.1 and 8.2. Streamlines terminated by the antenna load are marked with dashed color, and the non-absorbed streamlines are marked with solid line. The physical profile of the antennas are marked with straight solid line. In the E-plane, the Poynting streamlines are concentrated along the top of the dipole arm in the direction of the antenna load. Compared to the E-plane, fewer streamlines in the H-plane are terminated by the antenna load, which reflects the broader radiation pattern in the H-plane. For the Yagi-Uda antenna, streamlines are concentrated along the director elements and then transmitted to the driven element.

Poynting streamlines that are absorbed by the antenna load are associated with the shadow of the antenna as reflected by a decrease in the total field beyond the antenna relative to the arrival direction of the incident field. Near the antenna, due to the scattering from the antenna structure, some of the Poynting streamlines deviate from the straight paths associated with the incident field, but are not absorbed by the antenna load.

The IEEE standard definition of effective area is given by [86]

$$A_{\mathrm{e}} = \frac{P_{\mathrm{T}}}{W_{\mathrm{i}}} \tag{8.1}$$

where P_{T} is the available power at the terminals of a receiving antenna and W_{i} is the power flux density of a plane wave incident on the antenna from that direction with the aligned polarization to the antenna. The effective area definition provides only the scalar magnitude of this antenna parameter, and yields no information about the shape of an antenna's receiving area. For the dipole example, the receiving area can be assigned a geometrical shape using the Poynting streamline method.

For the dipole example, the Poynting streamlines terminated by the dipole antenna load extend from (0, -0.31) to (0, 0.31) in the E-plane. The terminated boundary of Poynting streamlines in each cut plane spans a two-dimensional locus that provides a geometrical shape for the effective area of the antenna. Figure 8.3 shows the load terminated Poynting streamline area shape for the dipole and Yagi-Uda antenna. It can seen that the shape of the locus of terminated streamlines is consistent with the analysis of [79], and the area of the locus is close to the effective area of the antenna calculated from its directivity. A comparison of the Poynting streamline area and the effective area is given in Table 8.1.

The Poynting streamline area shape of the Yagi-Uda antenna is close to circular. Normally, a high gain antenna is designed by maximizing gain, which is equivalent to maximizing the effective area. This suggests that antenna designs that achieve a circular or near circular Poynting streamline area are more effective than designs with elongated streamline areas, as they better utilize the space around the antenna to capture power in the incident wave.

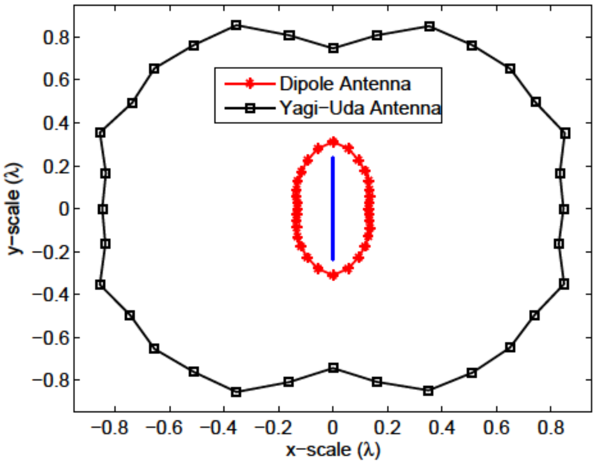

Figure 8.3: Comparison of Poynting streamline area shapes for a dipole and 15-element Yagi Uda antenna.

8.2.2 Traditional TE_{10}mode Horn Antenna

We now extend the Poynting streamline method to an aperture-type horn antenna. In Figure 8.4, Poynting streamlines for a 0.75 × 1.5 λ horn antenna with TE_{10}-mode aperture field distribution are shown. Compared to the H-plane, more streamlines are terminated by the antenna load in the E-plane, which is consistent with the narrower beamwidth in the H-plane.

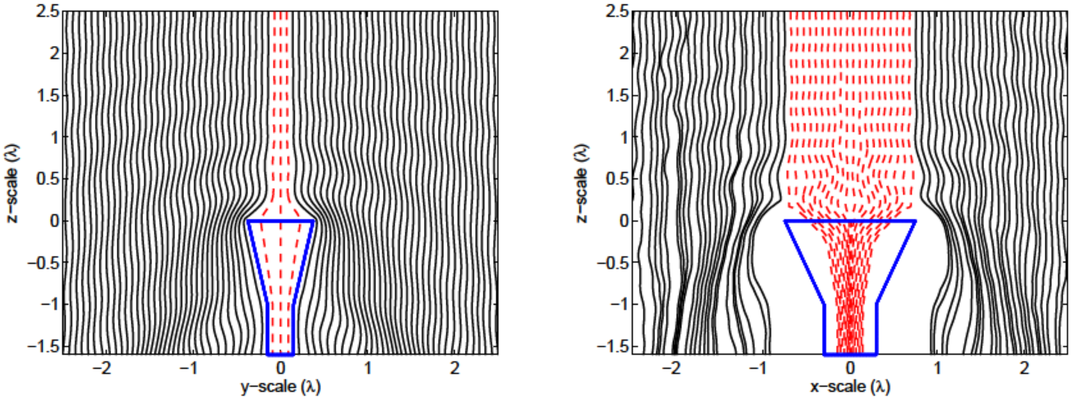

(a) E-plane.

(b) H-plane.

Figure 8.4: Poynting streamlines for a tradition TE_{10}-mode rectangular horn antenna. The dimension of horn antenna is 0.75 × 1.5 λ and the aperture efficiency is 0.8.

Figure 8.5 shows the Poynting streamline area shape and the induced aperture field distribution of the horn antenna corresponding to a normally incident plane wave. The Poynting streamline area shape and the aperture field distribution are close to the TE_{20}-mode field distribution, which is reasonable since the width of horn antenna is larger than the cutoff wavelength of the TE_{20}-mode. For the same horn operated as a transmitter, the aperture field behaves as a TE_{10}-mode distribution, which is different from the field in receive mode. This might seem surprising, as it appears to violate the reciprocity theorem, but reciprocity actually still holds, and the receiving and transmitting properties of the antenna are related in the usual way.

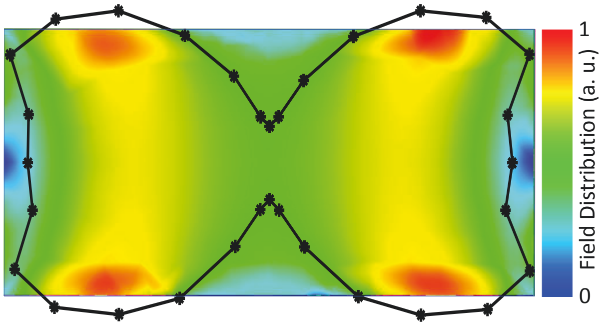

Figure 8.5: Poynting streamline area shape for a TE_{10}-mode horn antenna with 0.8 aperture efficiency and the horn aperture field distribution corresponding to a normally incident plane wave.

In Figure 8.4, the terminated Poynting streamlines by the antenna load in the E-plane and H-plane are located within the antenna physical aperture size. In the 45° and 135° cut planes shown in Figure 8.5, streamlines beyond the antenna physical area area absorbed by the load. This shows that for a non-superdirective aperture antenna, energy propagation outside the antenna physical area can be absorbed by the antenna load.

8.3 Superdirective Horn Antenna Design

We now consider the use of the Poynting streamline approach in guiding the design of superdirective aperture antennas. As observed above, one might conjecture that the Poynting steamline area shape should be circular to fully utilize the space around the antenna for an effective high-gain anteanna. For the horn antenna in Figure 8.5, there is a “notch” in the middle of the

Poynting streamline area along the vertical direction that less efficiently utilizes the physical aperture of the horn antenna, while the area for dipole antenna is enlongated in the vertical direction. Motivated by the Poynting streamline analysis, a screen can be placed in front of the horn antenna to achieve a more convex streamline area.

A design based on the Poynting streamline approach is shown in Figure 8.6. Two rows of conducting rods are placed in the front of the horn antenna considered in the previous section. The rods can be considered as a resonant parasitic dipole array. The induced current on the dipole array element can be controlled by changing the length of the rods. Superdirectivity can be implemented by optimizing the induced current on the rod elements. Similar to a superdirective dipole array, the current distribution on the rods exhibits a rapid phase oscillation. The rods in the second row are used to reduce the backscattered fields from the rods in the first row to the horn antenna and increase the forward radiation. The impedance match between the horn antenna and the antenna load improves with the added screen to an S_{11} of -19 dB at the design center frequency.

For the horn antenna with a 0.17 λ thick screen, the radiating mode is broadside to the screen and the horn aperture, and the directivity is increased by enhancing the dimension of the screen and horn laterally rather than axially like Yagi-Uda antennas. There is a well defined aperture and this particular antenna may be considered to be superdirective by the IEEE definition of the term. Based on this definition, the modeled aperture efficiency of the horn antenna with rods is 1.9, which is significantly higher than that of the bare horn antenna, for which the aperture efficiency is 0.8.

Figure 8.7 shows the Poynting streamlines for the superdirective horn antenna in the E-plane and H-plane. Streamlines between the screen and the horn are not computed because the streamlines become convoluted and cannot be extracted at the simulation resolution. Figure 8.8 shows the effective area shapes for the traditional and superdirective horn antennas. The Poynting streamline area of the superdirective antenna is larger than the physical aperture area, which indicates that fields outside the antenna physical aperture area can be absorbed by the antenna load.

Most earlier investigations of superdirectivity have been confined to antenna arrays with rapid phase oscillations and electrically small antennas with strongly resonant structures [81, 87–89]. For aperture antennas, methods have been developed to enhance aperture efficiency, but most

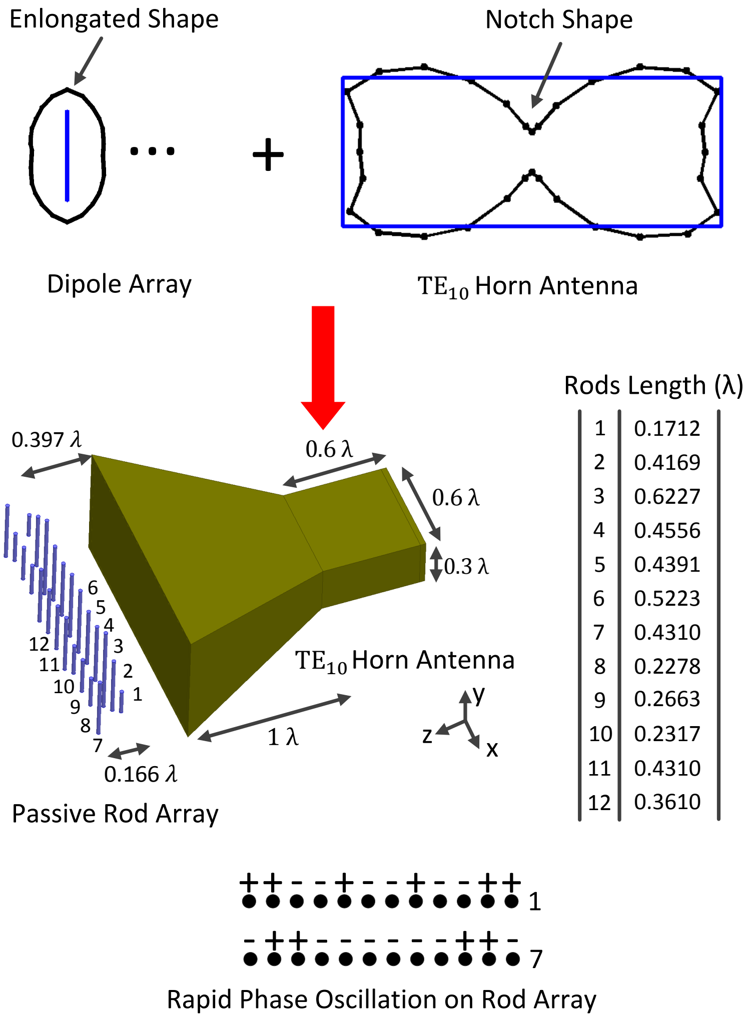

Rods Length (λ)

1	0.1712
2	0.4169
3	0.6227
4	0.4556
5	0.4391
6	0.5223
7	0.4310
8	0.2278
9	0.2663
10	0.2317
11	0.4310
12	0.3610

Figure 8.6: Poynting steamline method is used to guide a superdirectivity antenna design. Two rows of symmetric passive dipole array are located in front of a traditional TE_{10} horn antenna. Enlongated Poynting streamline area for dipole array is used to compensate the notch shape in the Poynting streamline area for the horn antenna. Similar to a superdirective dipole array, the current distribution on the rods exhibits rapid phase oscillation. Aperture efficiencies for the TE_{10} horn antenna and superdirective horn antenna are 0.8 and 1.9, respectively.

designs approach an efficiency of 100% and are not superdirective. The screened horn described here achieves a higher aperture efficiency than any other realistic design of which we are aware.

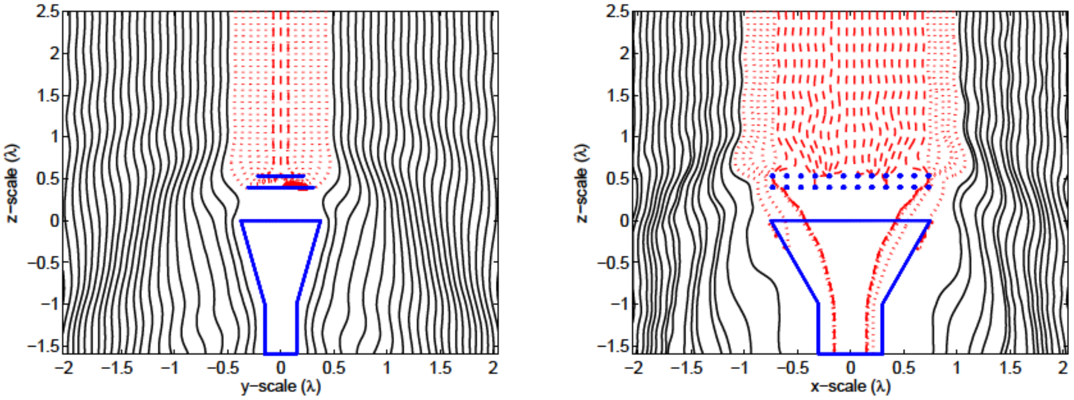

(a) E-plane.

(b) H-plane.

Figure 8.7: Poynting streamlines for a superdirective horn antenna with 1.9 aperture efficiency. The dashed lines represent streamlines terminated at the load of the bare horn antenna with 0.8 aperture efficiency and the dotted lines represent the additional Poynting streamlines terminated by the superdirective antenna load.

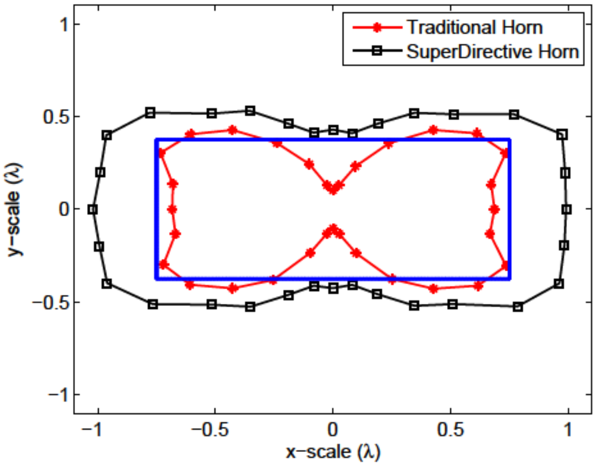

Figure 8.8: Effective area shape calculated from streamlines captured by a traditional horn antenna and a superdirective antenna with the same physical size. The straight lines represents the physical size of the horn antenna aperture.

8.3.1 Overcoming Practical Limitations of Superdirective Antennas

A practical limitation for superdirective antennas is the narrow frequency bandwidth. If the operating frequency is offset from the design frequency, the superdirectivity is eliminated [81]. Superdirectivity is sensitive to the excitation currents on the rods, which depends on the length of the rod elements and the aperture field distribution of the horn antenna. When the frequency is changed, currents distributions on the rods are no longer tuned to attract Poynting streamlines.

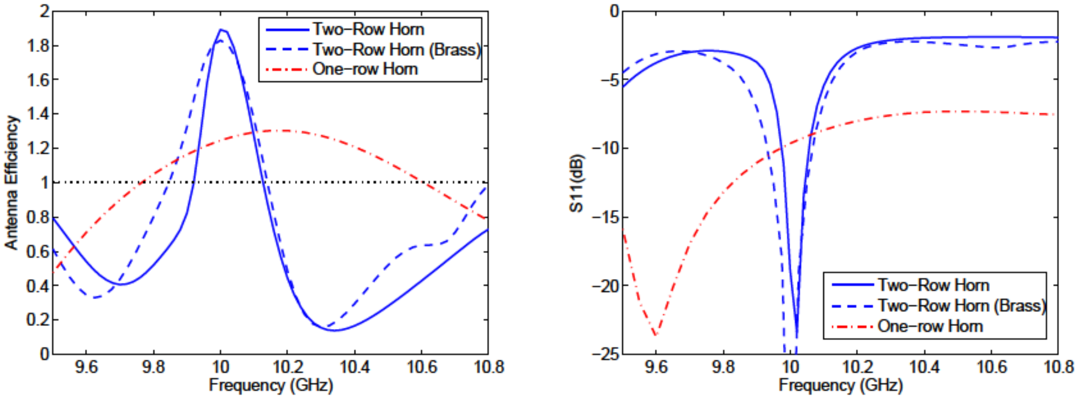

(a) Antenna efficiency.

(b) Antenna *S* parameters.

Figure 8.9: Antenna efficiency and antenna *S* parameters for superdirective horn antennas over frequencies. One-row and two-row rod horns are used for the narrow and wide bandwidth design respectively. The two-row screen with brass material quantifies the reduction in gain due to ohmic loss.

Antenna efficiency and input reflection coefficient are shown over frequency for the superdirective horn antenna in Figure 8.9. Antenna efficiency is the product of the aperture efficiency and radiation efficiency. The superdirectivity radiation bandwidth for the two-row rods horn design is 2.1%. A wider bandwidth superdirective antenna is designed by using only one row of resonant rods. As shown in Figure 8.9, although the maximum aperture efficiency is decreased to 1.3, the superdirectivity radiation bandwidth increases to 8.4% and the impedance bandwidth becomes larger. Superdirectivity requires a high Q value and a strong resonance of the antenna, but by lowering the aperture efficiency target, the Q value decreases and the superdirectivity bandwidth becomes wider.

Besides narrow frequency bandwidth, low radiation efficiency is another practical limitation for the superdirective antennas due to ohmic or dielectric losses exacerbated by intense near fields and currents on the antenna structure. The ohmic loss of the two-row superdirective antenna is studied in Figure 8.9a. When the material of the rods is modeled as brass, the antenna efficiency of the superdirective antenna is decreased by 6% and the bandwidth of superdirective operation is increased by 33%. The increase of superdirectivity bandwidth is due to the lower Q value when the lossy material is used for the antenna. The simple structure of the rod screen, the use of metal only for the directivity enhancing structure, and its location at the aperture rather than near the feed point help to minimize losses that would otherwise diminish the gain of the antenna.

Another practical limitation on superdirectivity is the extreme sensitivity of gain to fabrication errors [81]. For our design, the sensitivity to rod length is actually quite reasonable. The rod lengths can be increased by 1.4% and 11.5% for the two-row and one-row horns respectively before the aperture efficiency reduces to unity. This is well within the tolerance of standard manufacturing techniques.

8.3.2 Poynting Streamlines and Effective Area

We conjecture that the area of the locus of terminated Poynting streamlines is equal to the effective area calculated from the antenna directivity. We compare the Poynting streamline area A_s calculated from the shape area using the Poynting streamline method to the effective area calculated from $A_\text{e} = \lambda^2 D/(4\pi)$, where D represents the antenna directivity in Table 8.1. The maximum difference is 6.6%. Numerical error in the field distribution, integrating the streamlines, and the cut plane approach limit the accuracy of the calculation, but the study provides numerical evidence that the area of captured streamlines is equal to the effective area.

Table 8.1: Accuracy analysis

Antenna Type	A_e (λ^2)	A_s (λ^2)	Difference
Dipole	0.126	0.133	5.2%
Yagi-Uda	2.633	2.579	2.1%
Traditional Horn	0.898	0.961	6.6%
Superdirective Horn	2.128	1.997	6.3%

8.4 Summary

Using the method of Poynting streamlines, we have studied linear, aperture and superdirective receiving antennas. Using the locus of streamlines terminated by the antenna load, effective area shapes are given. Poynting streamline method is used to guide the high-directivity antenna design. A superdirective screened horn antenna with 1.9 aperture efficiency is compared to a traditional TE_{10}-mode horn antenna, which has an aperture efficiency of 0.8. To our knowledge, no superdirective antenna with such large electrical aperture and high aperture efficiency exists. The narrow bandwidth characteristic of superdirective antennas is considered, and a superdirective antenna with 1.3 aperture efficiency is designed with a factor of four larger superdirectivity bandwidth and less manufacture error requirement than the antenna with 1.9 aperture efficiency. Unlike many previous superdirective array antennas, the screened horn does not suffer from low radiation efficiency.

We show numerically that the area of the locus of streamlines terminated by the antenna load is close to the effective area of the antenna, and so we suggest this locus is similar to the effective area shape. The effective area shape might be considered as a supplementary to the IEEE standard definition of the effective area based on the strict mathematical demonstration. Proof that area of the locus of captured streamlines is equal to effective area remains an open question. The closed form solutions for the basic source such as small electric and magnetic dipole are instructive for the future work. There are also likely other types of antenna structures that could be enhanced using visualizations of the Poynting streamlines around the antenna.

CHAPTER 9. CONCLUSION AND FUTURE WORKS

9.1 Conclusion

For phased array feeds applied for radio astronomy observations, the bandwidth for the L-band dipole antenna for the Green Bank Telescope has been investigated by comparing to other wide band antennas. The excellent bandwidth performance is due to the antenna structure fully utilizing the space around the dipole, which is an important rule for the future antenna design. The measured S-parameters for the dipole antennas matched well with the simulated results using a full wave model, which is expected to achieve a high efficiency for the overall system test on the Green Bank Telescope. A 20 MHz down-converter system has been developed and successfully used for the experimental test of the Cornell/BYU L-band phased array feed system on Arecibo Telescope in 2013 and the Umass/BYU mm-wave phased array feed system on the Green Bank Telescope in 2015.

An accurate array noise model including a reflector antenna has been developed to study the performance for a 64-element mm-wave phased array feed on the Green Bank Telescope. The noise model includes a sky with non-uniform brightness noise temperature distribution and an array feed with an electrically large dewar box. The accuracy for this model has been verified by another independent model using different analysis method. With this model, the feed system performance in the presence of a thermal Dewar with an EM transparent window, installation position offset from the reflector focal position, required minimum number of array element for high-efficiency beamformer and expected figures of merits on the Green Bank Telescope has been studied. The mm-wave phased array feed was mounted and measured on the Green Bank Telescope in Nov. 2015 and the effectiveness of beamforming has been experimental demonstrated.

From the analysis of an ultra wide band phased array feed, we have found an inherent decrease of aperture efficiency between phased array feeds and cluster feeds. The physics is explained by the overlap of the array nears center elements and the first nulls of Airy pattern of the focal fields. Optimization of array layout and modification of the element pattern can improve the decrease of aperture efficiency to some extent. For phased array feeds, combining formed radiation pattern bandwidth limit with the Wheeler-Chu impedance bandwidth limit confines the performance bandwidth for a high sensitivity phased array feed.

Antenna loss for active receiving phased arrays and focal plane phased array feeds was studied using the active array receiving efficiency. To better understand the relationship between array antenna loss, mutual coupling, and beamformer weights, losses for a coupled array can be lumped into an array effective resistance similar to the loss resistance of an equivalent single antenna. Using a full-wave model, we have found that strong mutual coupling and large variation of beamformer weights lead to a decrease of array effective resistance and an increase of array effective loss resistance due to concentrated surface currents on the array elements. In addition to aperture arrays, we also considered phased array feeds located at the focal plane of a large reflector. Compared to phased array antennas, antenna loss for phased array feeds is more sensitive to mutual coupling and beam steering angle. This study showed that receiving efficiency and array effective resistance can be used to understand the behavior of array radiation and loss properties of high sensitivity array designs.

For phased arrays used for satellite communications, grating lobes become a major issue for the sparse array antenna design. To reduce the array element density and keep a low peak side lobe level in a large physical aperture, aperiodic arrays and tiled arrays has been investigated. From a bulk of optimization results for arrays with different element number and element density, we have found that for an aperiodic or tiled array, the peak side lobe level can be decreased by enhancing the element pattern gain at the main lobe direction, increasing the array element number and reducing the array electrical size. The relationship between the peak side lobe level, bandwidth, directivity, and design and fabrication complexity has been studied for uniform arrays, aperiodic arrays and tiled arrays. This study can be used to guide the design of a steered phased array with low peak side lobe level.

For superdirectivity study, we directly model a superdirective antenna as a receiving antenna using Poynting streamline method. Superdirectivity is implemented by expanding the effective area shape from the antenna physical aperture. Motivated by this method, a superdirective horn antenna with about 115% aperture efficiency has been experimentally demonstrated. The practical superdirectivity is studied by considering the drawbacks including narrow bandwidth, large antenna loss and sensitivity to the tolerance of element position and excitation. Using the Poynting streamline method, we suggested that the expanded distance of the effective area shape from the border of the antenna physical aperture remains approximately constant over different antenna aperture sizes and shapes. For practical applications, superdirectivity is practical for electrically small and middle size antennas and electrically large antennas with a large aspect ratio.

9.2 Future works

Recently, conformal phased array antennas have been widely applied in aircraft, missiles and satellites, but they have never been used for radio astronomy array feed design. Since all the array feeds have been planar until now, it is necessary to study the performance of spherical conformal array feeds. Compared to the traditional PAF, one possible advantage for a spherical conformal array feed is lower mutual-coupling effects between elements leading to a reduction of the system noise temperature. Another expected advantage is improved performance of the pattern element illumination leading to a at sensitivity map within the field of view.

A PAF is designed to match the reflector Airy pattern. For the boresight beam, the Airy pattern is circularly symmetrical, but it becomes elliptical when the beam is steered. Hence, the Airy patterns for each steered beam are non-uniformly distributed within the field of view, which requires array elements spacing to be non-uniform as well to match the Airy pattern. The element spacing for the current PAFs is uniform, so it is necessary to study non-uniform element spacing PAF. Compared to the conventional uniform element spacing PAFs, the expected advantages are better system sensitivity, an increased field of view, a flatter sensitivity map, and a sharper sensitivity drop at the boundary of the field of view.

REFERENCES

[1] D. F. Sievenpiper, D. C. Dawson, M. M. Jacob, T. Kanar, S. Kim, J. Long, and R. G. Quarfoth, "Experimental validation of performance limits and design guidelines for small antennas," *Antennas and Propagation, IEEE Transactions on*, vol. 60, no. 1, pp. 8–19, 2012. ix, 21, 109

[2] K. F. Warnick, D. Carter, T. Webb, J. Landon, M. Elmer, and B. D. Jeffs, "Design and characterization of an active impedance matched low noise phased array feed," *IEEE Transactions on Antennas and Propagation*, vol. 59, no. 6, pp. 1876–1885, 2011. 17, 90

[3] D. E. Carter, "Active impedance matching and sensitivity optimized phased array feed design for radio astronomy," Ph.D. dissertation, Brigham Young University, 2011. 20

[4] T. D. Webb, "Design and polarimetric calibration of dual-polarized phased array feeds for radio astronomy," 2012. 20

[5] R. Collin and S. Rothschild, "Evaluation of antenna q," *Antennas and Propagation, IEEE Transactions on*, vol. 12, no. 1, pp. 23–27, 1964. 21

[6] R. A. Black, "Digital back end development and interference mitigation methods for radio telescopes with phased-array feeds," 2014. 36

[7] F. J. Lockman, "Green bank telescope: an overview," in *Astronomical Telescopes & Instrumentation*. International Society for Optics and Photonics, 1998, pp. 656–665. 90

[8] P. R. Jewell and R. M. Prestage, "The green bank telescope," in *Astronomical Telescopes and Instrumentation*. International Society for Optics and Photonics, 2004, pp. 312–323. 90

[9] L. LaLonde, "The upgraded Arecibo observatory," *Science*, vol. 186, no. 4160, pp. 213–218, 1974. 90

[10] P. Kildal, L. Baker, T. Hagfors, *et al.*, "Development of a dual-reflector feed for the Arecibo radio telescope: an overview," *Antennas and Propagation Magazine, IEEE*, vol. 33, no. 5, pp. 12–18, 1991. 90

[11] R. Nan, "Five hundred meter aperture spherical radio telescope (FAST)," *Science in China series G*, vol. 49, no. 2, pp. 129–148, 2006. 90

[12] R. Nan, D. Li, C. Jin, Q. Wang, L. Zhu, W. Zhu, H. Zhang, Y. Yue, and L. Qian, "The five-hundred-meter aperture spherical radio telescope (FAST) project," *International Journal of Modern Physics D*, vol. 20, no. 06, pp. 989–1024, 2011. 90

[13] C. Carilli and S. Rawlings, "Science with the Square Kilometer Array: motivation, key science projects, standards and assumptions," *arXiv preprint astro-ph/0409274*, 2004. 90

[14] P. E. Dewdney, P. J. Hall, R. T. Schilizzi, and T. J. L. Lazio, “The square kilometre array,” *Proceedings of the IEEE*, vol. 97, no. 8, pp. 1482–1496, 2009. 90

[15] S. K. Rao, “Parametric design and analysis of multiple-beam reflector antennas for satellite communications,” *Antennas and Propagation Magazine, IEEE*, vol. 45, no. 4, pp. 26–34, 2003. 90

[16] Z. Yang and K. Warnick, “Multiband dual polarization high efficiency array feed for ku/reverse band satellite communications,” 2014. 90, 111

[17] J. D. Bunton *et al.*, “Figure of merit for SKA survey speed,” *SKA, Manchester, UK, Bunton\ _Survey\ _speed. pdf*, 2003. 91

[18] R. Olsson, P. Kildal, and S. Weinreb, “The eleven antenna: a compact low-profile decade bandwidth dual polarized feed for reflector antennas,” *Antennas and Propagation, IEEE Transactions on*, vol. 54, no. 2, pp. 368–375, 2006. 91

[19] J. Teniente, R. Gonzalo, and C. Del Rio, “Low sidelobe corrugated horn antennas for radio telescopes to maximize $\mathrm{G/T_S}$,” *Antennas and Propagation, IEEE Transactions on*, vol. 59, no. 6, pp. 1886–1893, 2011. 91

[20] J. Yang, M. Pantaleev, P. Kildal, B. Klein, Y. Karandikar, L. Helldner, N. Wadefalk, and C. Beaudoin, “Cryogenic 2–13 GHz eleven feed for reflector antennas in future wideband radio telescopes,” *Antennas and Propagation, IEEE Transactions on*, vol. 59, no. 6, pp. 1918–1934, 2011. 91, 111

[21] W. A. Imbriale, S. Weinreb, G. Jones, H. Mani, and A. Akgiray, “The design and performance of a wideband radio telescope for the GAVRT program,” *Antennas and Propagation, IEEE Transactions on*, vol. 59, no. 6, pp. 1954–1962, 2011. 91

[22] D. T. Emerson, U. Klein, and C. Haslam, “A multiple beam technique for overcoming atmospheric limitations to single-dish observations of extended radio sources,” *Astronomy and Astrophysics*, vol. 76, pp. 92–105, 1979. 91

[23] P. Kildal, M. Johansson, T. Hagfors, and R. Giovanelli, “Analysis of a cluster feed for the Arecibo trireflector system using forward ray tracing and aperture integration,” *Antennas and Propagation, IEEE Transactions on*, vol. 41, no. 8, pp. 1019–1025, Aug 1993. 91

[24] L. Staveley-Smith, W. Wilson, T. Bird, M. Disney, R. Ekers, K. Freeman, R. Haynes, M. Sinclair, R. Vaile, R. Webster, *et al.*, “The parkes 21 cm multibeam receiver,” *Publications of the Astronomical Society of Australia*, vol. 13, pp. 243–248, 1996. 91

[25] B. Veidt, “Focal-plane array architectures: Horn clusters vs. phased-array techniques,” 2006. 91

[26] K. F. Warnick, B. D. Jeffs, J. Landon, J. Waldron, D. Jones, J. R. Fisher, and R. Norrod, “Beamforming and imaging with the BYU/NRAO L-band 19-element phased array feed,” in *Antenna Technology and Applied Electromagnetics and the Canadian Radio Science Meeting, 2009. ANTEM/URSI 2009. 13th International Symposium on*. IEEE, 2009, pp. 1–4. 91

[27] M. V. Ivashina, M. N. M. Kehn, P. Kildal, and R. Maaskant, “Decoupling efficiency of a wideband vivaldi focal plane array feeding a reflector antenna,” *Antennas and Propagation, IEEE Transactions on*, vol. 57, no. 2, pp. 373–382, 2009. 91, 122

[28] D. R. DeBoer, R. G. Gough, J. D. Bunton, T. J. Cornwell, R. J. Beresford, S. Johnston, I. J. Feain, A. E. Schinckel, C. A. Jackson, M. J. Kesteven, *et al.*, “Australian ska pathfinder: A high-dynamic range wide-field of view survey telescope,” *Proceedings of the IEEE*, vol. 97, no. 8, pp. 1507–1521, 2009. 91

[29] W. van Cappellen, S. Wijnholds, and L. Bakker, “Experimental evaluation of polarimetric beamformers for an L-band phased array feed,” in *Antennas and Propagation (EUCAP), 2012 6th European Conference on*. IEEE, 2012, pp. 634–637. 91

[30] J. Diao, R. Black, J. Brady, J. Sypherd, K. F. Warnick, and B. D. Jeffs, “Modeling and system development for the flag l-band phased array feed for large-dish astronomical observations,” in *Radio Science Meeting (Joint with AP-S Symposium), 2015 USNC-URSI*. IEEE, 2015, pp. 363–363. 91

[31] G. Cortes-Medellin, A. Vishwas, S. C. Parshley, and D. B. Campbell, “Fully cryogenic phased array prototype camera for the Arecibo radio telescope,” in *SPIE Astronomical Telescopes+ Instrumentation*. International Society for Optics and Photonics, 2014, pp. 91 479Q–91 479Q. 91

[32] M. Ivashina, V. Ardenne, and J. D. B. Arnold, “A way to improve the field of view of the radiotelescope with a dense focal plane array,” in *Microwave and Telecommunication Technology, 2002. CriMiCo 2002. 12th International Conference*. IEEE, 2002, pp. 278–281. 91

[33] M. Ivashina, M. N. M. Kehn, and P.-S. Kildal, “Optimal number of elements and element spacing of wide-band focal plane arrays for a new generation radio telescope,” in *Antennas and Propagation, 2007. EuCAP 2007. The Second European Conference on*. IET, 2007, pp. 1–7. 91

[34] K. F. Warnick and B. D. Jeffs, “Efficiencies and system temperature for a beamforming array,” *Antennas and Wireless Propagation Letters, IEEE*, vol. 7, pp. 565–568, 2008. 91, 111, 115, 117

[35] K. F. Warnick, M. V. Ivashina, R. Maaskant, and B. Woestenburg, “Unified definitions of efficiencies and system noise temperature for receiving antenna arrays,” *Antennas and Propagation, IEEE Transactions on*, vol. 58, no. 6, pp. 2121–2125, 2010. 91, 113

[36] M. V. Ivashina, O. Iupikov, R. Maaskant, W. A. van Cappellen, and T. Oosterloo, “An optimal beamforming strategy for wide-field surveys with phased-array-fed reflector antennas,” *Antennas and Propagation, IEEE Transactions on*, vol. 59, no. 6, pp. 1864–1875, 2011. 91

[37] H. Yordanov, M. T. Ivrlac, P. Russer, and J. A. Nossek, “Arrays of isotropic radiators–a field-theoretic justification,” in *2009 Intern. ITG Workshop on Smart Antennas*, 2009. 93

[38] M. Ivashina and C. v. Klooster, "Focal fields in reflector antennas and associated array feed synthesis for high efficiency multi-beam performances," *TIJDSCHRIFT-NERG*, vol. 68, no. 1, pp. 11–19, 2003. 94

[39] C. A. Balanis, *Antenna theory: analysis and design*. John Wiley & Sons, 2012. 98

[40] N. Erickson, G. Narayanan, J. Bardin, K. Warnick, B. Jeffs, and J. Diao, "A 64 element, 70–95 ghz focal plane phased array," in *Antennas and Propagation & USNC/URSI National Radio Science Meeting, 2015 IEEE International Symposium on*. IEEE, 2015, pp. 1514–1515. 104

[41] N. Yaru, "A note on super-gain antenna arrays," *Proceedings of the IRE*, vol. 39, no. 9, pp. 1081–1085, 1951. 106

[42] Y. Lo, S. Lee, and Q. Lee, "Optimization of directivity and signal-to-noise ratio of an arbitrary antenna array," *Proceedings of the IEEE*, vol. 54, no. 8, pp. 1033–1045, 1966. 106

[43] N. W. Bikhazi and M. A. Jensen, "The relationship between antenna loss and superdirectivity in MIMO systems," *Wireless Communications, IEEE Transactions on*, vol. 6, no. 5, pp. 1796–1802, 2007. 106

[44] G. J. Foschini and M. J. Gans, "On limits of wireless communications in a fading environment when using multiple antennas," *Wireless personal communications*, vol. 6, no. 3, pp. 311–335, 1998. 111

[45] M. V. Ivashina, R. Maaskant, and B. Woestenburg, "Equivalent system representation to model the beam sensitivity of receiving antenna arrays," *IEEE Antennas and Wireless Propagation Letters*, vol. 7, pp. 733–737, 2008. 111

[46] K. F. Warnick, D. Carter, T. Webb, J. Landon, M. Elmer, and B. D. Jeffs, "Design and characterization of an active impedance matched low-noise phased array feed," *IEEE Transactions on Antennas and Propagation*, vol. 59, no. 6, pp. 1876–1885, 2011. 111

[47] Z. Yang, K. C. Browning, and K. F. Warnick, "High-efficiency stacked shorted annular patch antenna feed for ku-band satellite communications," *IEEE Transactions on Antennas and Propagation*, vol. 64, no. 6, pp. 2568–2572, 2016. 111

[48] A. Bevilacqua and A. M. Niknejad, "An ultrawideband cmos low-noise amplifier for 3. 1-10. 6-ghz wireless receivers," *IEEE Journal of Solid-State Circuits*, vol. 39, no. 12, pp. 2259–2268, 2004. 111

[49] M. Varonen, R. Reeves, P. Kangaslahti, L. Samoska, J. W. Kooi, K. Cleary, R. S. Gawande, A. Akgiray, A. Fung, T. Gaier, *et al.*, "An mmic low-noise amplifier design technique," *IEEE Transactions on Microwave Theory and Techniques*, vol. 64, no. 3, pp. 826–835, 2016. 111

[50] R. Maaskant, D. J. Bekers, M. J. Arts, W. A. van Cappellen, and M. V. Ivashina, "Evaluation of the radiation efficiency and the noise temperature of low-loss antennas," *IEEE Antennas and Wireless Propagation Letters*, vol. 8, pp. 1166–1170, 2009. 111

[51] I. T. U. R. itu-r p.372-6. [Online]. Available: https://www.itu.int/dms pubrec/itu-r/rec/p/R REC-P.372-6-199408 S!!PDF-E.pdf. 112

[52] A. Committee *et al.*, “Ieee standard definitions of terms for antennas.” 112

[53] K. F. Warnick, B. Woestenburg, L. Belostotski, and P. Russer, “Minimizing the noise penalty due to mutual coupling for a receiving array,” *IEEE transactions on antennas and propagation*, vol. 57, no. 6, pp. 1634–1644, 2009. 117

[54] J. Diao and K. F. Warnick, “On the bandwidth gap between the array-feed and cluster-feed regimes for broadband multifeed systems,” *IEEE Transactions on Antennas and Propagation*, vol. 64, no. 6, pp. 2207–2216, 2016. 126

[55] Y. Lo, “A mathematical theory of antenna arrays with randomly spaced elements,” *IEEE Transactions on Antennas and Propagation*, vol. 12, no. 3, pp. 257–268, 1964. 129

[56] B. Steinberg, “The peak sidelobe of the phased array having randomly located elements,” *IEEE Transactions on Antennas and Propagation*, vol. 20, no. 2, pp. 129–136, 1972. 129, 136

[57] ——, “Comparison between the peak sidelobe of the random array and algorithmically designed aperiodic arrays,” *IEEE Transactions on Antennas and Propagation*, vol. 21, no. 3, pp. 366–370, 1973. 129

[58] M. Donvito and S. Kassam, “Characterization of the random array peak sidelobe,” *IEEE Transactions on Antennas and Propagation*, vol. 27, no. 3, pp. 379–385, 1979. 129, 136

[59] W. J. Hendricks, “The totally random versus the bin approach for random arrays,” *IEEE Transactions on antennas and propagation*, vol. 39, no. 12, pp. 1757–1762, 1991. 129

[60] R. L. Fante, G. A. Robertshaw, and S. Zamoscianyk, “Observation and explanation of an unusual feature of random arrays with a nearest-neighbor constraint,” *IEEE Transactions on Antennas and Propagation*, vol. 39, no. 7, pp. 1047–1049, 1991. 129

[61] R. L. Haupt, “An introduction to genetic algorithms for electromagnetics,” *IEEE Antennas and Propagation Magazine*, vol. 37, no. 2, pp. 7–15, 1995. 129

[62] W. C. Barott and P. G. Steffes, “Grating lobe reduction in aperiodic linear arrays of physically large antennas,” *IEEE Antennas and Wireless Propagation Letters*, vol. 8, pp. 406–408, 2009. 129

[63] M. D. Gregory, F. A. Namin, and D. H. Werner, “Exploiting rotational symmetry for the design of ultra-wideband planar phased array layouts,” *IEEE Transactions on Antennas and Propagation*, vol. 61, no. 1, pp. 176–184, 2013. 129

[64] M. DUrso, G. Prisco, and R. M. Tumolo, “Maximally sparse, steerable, and nonsuperdirective array antennas via convex optimizations,” *IEEE Transactions on Antennas and Propagation*, vol. 64, no. 9, pp. 3840–3849, 2016. 129

[65] R. L. Haupt, “Thinned arrays using genetic algorithms,” *IEEE Transactions on Antennas and Propagation*, vol. 42, no. 7, pp. 993–999, 1994. 129

[66] M. G. Bray, D. H. Werner, D. W. Boeringer, and D. W. Machuga, "Optimization of thinned aperiodic linear phased arrays using genetic algorithms to reduce grating lobes during scanning," *IEEE Transactions on antennas and propagation*, vol. 50, no. 12, pp. 1732–1742, 2002. 129

[67] O. Quevedo-Teruel and E. Rajo-Iglesias, "Ant colony optimization in thinned array synthesis with minimum sidelobe level," *IEEE Antennas and Wireless Propagation Letters*, vol. 5, no. 1, pp. 349–352, 2006. 129

[68] W. P. Keizer, "Synthesis of thinned planar circular and square arrays using density tapering," *IEEE Transactions on Antennas and Propagation*, vol. 62, no. 4, pp. 1555–1563, 2014. 129

[69] P. Hall and M. Smith, "Sequentially rotated arrays with reduced sidelobe levels," *IEE Proceedings-Microwaves, Antennas and Propagation*, vol. 141, no. 4, pp. 321–325, 1994. 130

[70] D. H. Werner, W. Kuhirun, and P. L. Werner, "Fractile arrays: A new class of tiled arrays with fractal boundaries," *IEEE Transactions on Antennas and Propagation*, vol. 52, no. 8, pp. 2008–2018, 2004. 130

[71] V. Pierro, V. Galdi, G. Castaldi, I. M. Pinto, and L. B. Felsen, "Radiation properties of planar antenna arrays based on certain categories of aperiodic tilings," *IEEE transactions on antennas and propagation*, vol. 53, no. 2, pp. 635–644, 2005. 130

[72] K. C. Kerby and J. T. Bernhard, "Sidelobe level and wideband behavior of arrays of random subarrays," *IEEE transactions on antennas and propagation*, vol. 54, no. 8, pp. 2253–2262, 2006. 130

[73] T. G. Spence and D. H. Werner, "Design of broadband planar arrays based on the optimization of aperiodic tilings," *IEEE Transactions on Antennas and Propagation*, vol. 56, no. 1, pp. 76–86, 2008. 130

[74] R. Mailloux, S. Santarelli, T. Roberts, and D. Luu, "Irregular polyomino-shaped subarrays for space-based active arrays," *International Journal of Antennas and Propagation*, vol. 2009, 2009. 130

[75] P. Hannan, "The element-gain paradox for a phased-array antenna," *IEEE Transactions on Antennas and Propagation*, vol. 12, no. 4, pp. 423–433, 1964. 142

[76] P. Kildal, A. Vosoogh, and S. Maci, "Fundamental directivity limitations of dense array antennas: A numerical study using hannans embedded element efficiency," *IEEE Antennas and Wireless Propagation Letters*, vol. 15, pp. 766–769, 2016. 142

[77] R. W. Sharpe, "Differential geometry, volume 166 of graduate texts in mathematics," 1997. 144

[78] B. Müller, "Energy flow in the near field of a receiving antenna(electromagnetic near field energy flow characteristics of dipole/monopole receiving rod antenna, investigating frequency dependence of antenna effective area shape)," *Archiv fuer Elektronik und Uebertragungstechnik*, vol. 26, pp. 443–449, 1972. 145

[79] G. Greving, "Gain calculation of thin wire antennas using the effective area approach and some inherent problems," *Archiv Elektronik und Uebertragungstechnik*, vol. 32, pp. 49–56, 1978. 145, 148

[80] E. Shamonina, V. Kalinin, K. Ringhofer, and L. Solymar, "Short dipole as a receiver: effective aperture shapes and streamlines of the poynting vector," in *Microwaves, Antennas and Propagation, IEE Proceedings*, vol. 149, no. 3. IET, 2002, pp. 153–159. 145, 146

[81] R. C. Hansen, "Fundamental limitations in antennas," *Proceedings of the IEEE*, vol. 69, no. 2, pp. 170–182, 1981. 145, 151, 153, 155

[82] T. S. Bird and C. Granet, "Optimization of profiles of rectangular horns for high efficiency," *Antennas and Propagation, IEEE Transactions on*, vol. 55, no. 9, pp. 2480–2488, 2007. 145

[83] R. J. Bauerle, R. Schrimpf, E. Gyorko, and J. Henderson, "The use of a dielectric lens to improve the efficiency of a dual-polarized quad-ridge horn from 5 to 15 ghz," *IEEE Transactions on Antennas and Propagation*, vol. 57, no. 6, pp. 1822–1825, 2009. 145

[84] H. F. Ma, X. Chen, H. S. Xu, X. M. Yang, W. X. Jiang, and T. J. Cui, "Experiments on high-performance beam-scanning antennas made of gradient-index metamaterials," *Applied Physics Letters*, vol. 95, no. 9, p. 094107, 2009. 145

[85] E. Jones, W. T. Joines, *et al.*, "Design of Yagi-Uda antennas using genetic algorithms," *Antennas and Propagation, IEEE Transactions on*, vol. 45, no. 9, pp. 1386–1392, 1997. 146

[86] "IEEE standard definitions of terms for antennas," IEEE Std 145-2013. 148

[87] L. J. Chu, "Physical limitations of omni-directional antennas," *Journal of applied physics*, vol. 19, no. 12, pp. 1163–1175, 1948. 151

[88] V. V. Veremey and R. Mittra, "Scattering from structures formed by resonant elements," *IEEE Transactions on antennas and propagation*, vol. 46, no. 4, pp. 494–501, 1998. 151

[89] A. E. Krasnok, D. S. Filonov, C. R. Simovski, Y. S. Kivshar, and P. A. Belov, "Experimental demonstration of superdirective dielectric antenna," *Applied Physics Letters*, vol. 104, no. 13, p. 133502, 2014. 151